THE UNIVERSITY *of* EDINBURGH

Time-dependent Ionisation of Metals in the Intergalactic Medium

Simon C. Reynolds

Institute for Astronomy
School of Physics

University of Edinburgh
Doctor of Philosophy

September 2010

Abstract

This thesis presents the results of a study into modelling the ionisation of heavy elements in the intergalactic medium (IGM) by solving the time-dependent ionisation rate equations. An algorithm has been developed which calculates ionisation fractions of the first 30 elements (hydrogen to zinc) as a function of time, given the gas density and temperature, and the ultra-violet radiation intensity. The results from this algorithm are compared against the standard assumption of ionisation equilibrium used in previous models of IGM metals.

Firstly, the new time-dependent algorithm is used to model the ionisation in uniform volumes of gas, with constant temperature, density and background radiation. Four models are performed, with different values of the ionisation parameter. The models demonstrate the timescales over which different metals in the IGM can be out of ionisation equilibrium, to investigate the conditions under which the time-dependent algorithm should be used in future modelling of metals in the IGM. The models show that for ionisation parameters $U = 0.01$–0.3 many metals observed in quasar absorption spectra could be out of equilibrium for up to 10^7 or a few times 10^8 years when subject to a new hard quasar spectrum. The metals' equilibrium ionisation fractions found in these time-dependent results are compared against the time-independent solutions found by Cloudy (Ferland et al., 1998, PASP, 110, 761) for the same models. Comparing to this well-established programme shows the algorithm is accurate for the most common elements, but disagreement is found for the rarer elements with incomplete atomic data.

An application of the new time-dependent ionisation algorithm to a full cosmological N-body simulation is then presented. The algorithm is used to study the effects of a young quasar on the ionisation structure of metals in the surrounding IGM. An independent simulation of a quasar turning on during the Epoch of Reionisation, performed with a joint particle-mesh and radiative-transfer code (Tittley & Meiksin,

2007, MNRAS, 380, 1369), is used to provide the density, temperature and UV intensity inputs for the time-dependent algorithm. Non-equilibrium effects in the metal ionisation are seen to last for significant lengths of time, as the IGM reacts slowly to the rapid change in UV radiation.

Mock quasar absorption line spectra are then generated by passing lines of sight through the simulation volume. Using the ionisation fraction results from the new algorithm, transmission functions with metal absorption features are produced, and the effect of non-equilibrium ionisation on the CII and CIV column densities and their ratio are presented.

Declaration

I declare that this thesis is not substantially the same as any that I have submitted for a degree or diploma or other qualification at any other University. I further state that no part of my thesis has already been or is being concurrently submitted for any such degree, diploma or other qualification.

This thesis is the outcome of my own work except where specifically indicated in the text. The research described was done in collaboration with my supervisors, Avery Meiksin and Eric Tittley. All of their contributions are individually acknowledged and I carried out all of the other work described.

Simon Reynolds,
Edinburgh,
September 2010.

Acknowledgements

I could not have got through my PhD without the help and support of many people. In particular, I owe a huge thanks:

To Avery, for patiently guiding me all the way through this project;

To Eric, supervisor and friend, for fixing everything time and again and for always being there to help me;

To everyone who shares their work freely, including the creators of CVode and Cloudy for sharing their source code, Dima Verner for his collection of atomic data, Kohji Yoshikawa for supplying me with data, and John Webb and Chris Churchill for allowing me to reproduce their diagrams;

To my Edinburgh flat-mates, office-mates, and all of the other students at the IfA, for the friendship and the good times;

To my family, for their love and support;

To everyone who put me up when I returned to Edinburgh whilst finishing my PhD, for kindness, generosity, and a sofa. Special mention to Stuart and Dave who never failed to make me feel welcome when I showed up on the doorstep.

Finally, all my love and thanks to Rita, for supporting me in every way through this and for the huggin' and kickin' without which this thesis would never have got finished.

Contents

Chapter 1

Introduction

Observations of quasar spectra during the last forty years have shown that the space in between galaxies is not a perfect vacuum. Instead, it is permeated by a tenuous photoionised plasma of hydrogen, helium and a small fraction of heavier elements (or 'metals'). During the last fifteen years we have formed a good understanding of the origin and conditions of this intergalactic medium (IGM) thanks to advances in telescope and spectrograph technology, and in numerical simulations. However, there remain many questions to answer, especially regarding the metals.

In this thesis I present an investigation into accurately modelling the ionisation of these metals. Previous IGM models have typically assumed that the metals are in ionisation equilibrium, but this may not always be valid. It is possible that regions of the IGM may be out of equilibrium for significant lengths of time, especially in the vicinity of bright, short-lived sources such as galaxies hosting a quasar or undergoing a burst of star-formation. To study this, I relax the assumption of ionisation equilibrium, and numerically model the time-dependent ionisation of the metals.

This chapter provides a review of the background to this work. First an overview of the concordance cosmology is given, followed in §1.2 by a review of the science of quasar absorption spectra and the intergalactic medium. §1.3 introduces the metals in the IGM. The final section of this chapter explains the methods used in simulating the IGM and reviews the most recent results from this field.

Chapter 2 details the time-dependent ionisation rate-equations algorithm developed

in this work. Chapter 3 explains the first use of the programme that was produced, modelling the ionisation of metals in a medium with constants physical conditions. Chapter 4 presents the second use of the programme, using inputs from a cosmological simulation to then model the ionisation of metals around a young quasar. Chapter 5 gives the details of the work to produce artificial absorption spectra from the simulation results, and an analysis of the results.

1.1 Background Cosmology

Our current best model of the Universe is the Λ-Cold Dark Matter model (ΛCDM). This states that the energy density of the Universe consists of approximately 73% dark energy, 23% cold dark matter and only 4% baryonic matter (e.g. Komatsu et al., 2009). Dark energy is a vacuum energy which we cannot directly detect, and which is often modelled as a 'cosmological constant' (Λ). Dark matter is the name given to as-yet unidentified mass that was first detected in the rotation curves of galaxies, and which does not interact with light but does obey gravity. The dark matter in the ΛCDM model is referred to as 'cold' because it slows to non-relativistic speeds at early times (which causes structures to form first at small scales, as explained below). Our current best model suggests that dark matter is made up of a class of hypothetical sub-atomic particles which feel gravity (i.e. have mass) and the weak nuclear force, therefore known as 'weakly-interacting massive particles' or WIMPs. There is around six times more dark matter than baryonic matter, which includes most of the mass around us on the Earth, all other visible matter in the Universe such as stars and galaxies, and all of the intervening gas which is not in these collapsed objects, such as the interstellar medium (ISM) and the IGM.

ΛCDM is a Hot Big Bang model, in which the Universe is expanding from an initial hot, dense state. We observe light that was emitted by any distant object at wavelength λ_{emit}, as being redshifted to a longer wavelength λ_{obs}, and define the redshift z as:

$$z = \frac{\lambda_{obs} - \lambda_{emit}}{\lambda_{emit}}. \tag{1.1}$$

The ratio between the observed and emitted wavelengths is then given by $(1+z)$. This effect resembles the everyday Doppler effect where $(1+z) = 1 + v/c$, or the relativistic equivalent where $(1+z) = \gamma(1+v/c)$. The cosmological redshift is often thought of as an effect of the recession velocities of the objects, but is however a distinct effect. The wavelength of the radiation from distant objects expands along with the expanding

space that it travels through, according to the formula:

$$(1+z) = \frac{R_0}{R(t_{emit})}, \tag{1.2}$$

where $R(t)$ is the scale factor at some time t, in units of distance, and R_0 is its present value. Since redshift increases for more distant objects, and the light travel time means that more distant objects appear to us as they were at earlier times, the word 'redshift' is also used refer to both distant regions and earlier epochs of the Universe.

The expansion means that recession velocities v are higher for objects at a greater distance r, and we define the Hubble parameter such that $v = H(t) \times r$, and find:

$$H(t) = \frac{\dot{R}(t)}{R(t)}. \tag{1.3}$$

The dot represents the derivative with respect to cosmological time. Surveys of type Ia supernovae (exploding stars visible at great distances) together with measurements of the matter power spectrum measured in galaxy redshift surveys, and measurements of the power spectrum of anisotropies in the Cosmic Microwave Background radiation (see below), have shown that the expansion of the Universe is now accelerating. This is due to the large dark energy component of the Universe.

At the time of the Big Bang, the temperature was so high that the four fundamental forces we know today (gravity, the strong and weak nuclear forces and the electromagnetic force) could not exist separately. During the first second, these forces separated in turn as the expansion lowered the temperature sufficiently for each type of force-carrying particle to form. After gravity and then the strong nuclear force had separated from the combined electroweak force, the Universe underwent a period known as inflation, during which it expanded exponentially. Around one second after the Big Bang, the Universe reached a temperature low enough for quarks to join together into hadrons, including the protons and neutrons which make up atomic nuclei.

Within the first few minutes, Big Bang nucleosynthesis (BBN) occurred, as the protons and neutrons combined through various stages to form heavier nuclei. This process formed most of the helium in the Universe, but could not form any nuclei heavier than beryllium. By the time the Universe cooled enough to end the processes of BBN, it had formed most of the light nuclei that we see today: hydrogen-1, helium-4, deuterium (hydrogen-2), helium-3, lithium-7 and lithium-6. Also formed during BBN were tritium (hydrogen-3) and beryllium-7 but these decay with short half-lives and have not survived to the present day. The intergalactic medium represents all of the regions of this primordial gas which have survived without collapsing under gravity to

form other structures. One of the big questions in IGM studies is the extent to which it maintains its primordial element abundances established by BBN or the extent to which it has been polluted with other elements formed much later within stars.

The Universe continued to expand and cool, and was dominated by radiation until *matter-radiation equality*, some 7×10^4 years after the Big Bang, when the radiation density (which scales differently with the changing volume of the Universe) dropped below the density of matter. After $2-3 \times 10^5$ years, the hot plasma had cooled enough for recombination, when the protons and helium nuclei were able to capture electrons to form neutral atoms. At this time, photons were for the first time able to move freely without scattering off the free electrons, and we detect these first free-streaming photons today as the Cosmic Microwave Background (CMB) radiation.

The matter content of the Universe, which has dominated through most of cosmic history, is mostly cold dark matter. Eventually the Universe became cool enough for all of the matter to start to collapse gravitationally. This amplified inhomogeneities imprinted on the matter distribution by tiny variations that were expanded by inflation. Overdensities attracted more matter and became more dense, leaving underdensities to become even less dense. On the scale of galaxies, this collapse can be treated as following a simple linear equation at early times, but it eventually became nonlinear as dense regions formed. Our current model of this collapse is hierarchical, in that we believe large structures such as the dark matter halos of galaxies and galaxy clusters formed by the merging of smaller halos which formed earlier (i.e. a *bottom-up* scenario). This is a feature of cold dark matter models, in which the dark matter particles slow to non-relativistic speeds long before the era of matter-radiation equality, so structures smaller than the horizon size can survive and collapse first. In hot dark matter models (for example, if dark matter was made up of massive neutrinos) the particles would still have velocities close to the speed of light at the time of matter-radiation equality, erasing structures smaller than the horizon size. Such models therefore feature larger structures forming first, and structure we see today on the scale of galaxies would have had to form in a *top-down* scenario, by fragmentation of supercluster scale structures. Our concordance cosmology is a cold dark matter model because this fits out observations best (particularly for the matter power spectrum).

While the Universe continued to expand, the collapsing structures of cold dark matter and baryons left the 'Hubble flow' of the expansion. They continued to become more dense as their mass increased and they attracted more matter. Within the dark matter halos, clouds of baryonic gas were able to collapse down to form even more

dense structures, producing the first stars and galaxies. The first stars were formed from pristine primordial gas, and the lack of metals in this gas is expected to have produced very different stars, known as Population-III stars with masses a few hundred times that of the Sun. These stars, along with subsequent generations of Population-II and Population-I stars, produced all heavier elements in the Universe that were not made during BBN (or artificially by man) either in nuclear fusion in their cores, or when they explode as supernovae.

We now believe that all large galaxies form a supermassive black-hole (SMBH) at their centre. Some, and perhaps all, of these galaxies go through an active phase when they emit vast amounts of energy while baryonic matter accretes on to the SMBH. These active galactic nuclei (AGN) are observed as a variety of different types depending on the strength of their emission in different wavebands, and on their orientation towards us. These have resulted in a variety of different historical names for the observed objects (quasars, quasi-stellar objects or QSOs, Seyfert I galaxies, etc.) which are now understood to belong to the same broad class of objects.

Another important phase change occurred during the 'epoch of reionisation' (EoR) when radiation emitted by the first structures turned the IGM back in to a plasma as it is today. This reionisation probably occurred in two stages, the first ionising the hydrogen and singly ionising the helium (possibly by the very first stars to form) and the second fully ionising the helium (probably by quasars).

The result of the hierarchical structure formation described above, is a characteristic distribution of matter often called the 'cosmic web'. When we map the locations of galaxies by measuring their positions on the sky and their redshifts, we find this pattern, with void regions surrounded by dense sheets which meet at denser filaments, which themselves meet at even more dense spherical nodes. This is known as the Large Scale Structure of the Universe (LSS) as we believe these superclusters of galaxies to be the largest scale on which the Universe shows inhomogeneities. One of the big successes of the ΛCDM model is its ability to recreate this cosmic web in N-body simulations of dark matter from a few simple initial conditions. The same pattern of voids, sheets, filaments and nodes is seen in the structure of the IGM, on scales much smaller than the LSS, formed by the same dark matter distribution but traced out by overdensities in the gas rather than the distribution of galaxies.

1.2 Quasar Absorbers and the IGM

1.2.1 Quasar Spectra

Quasars are seen with redshifts up to $z = 6.4$, making them some of the most distant observable astronomical objects. The light we see from them has travelled vast distances across the Universe, and provides us with information about when the Universe was much younger. Their spectra consist of emission features from the AGN that power them, but also absorption features from the intervening matter along our lines-of-sight (LOS). In the forty years since they were first observed, these absorption spectra have become essential tools in cosmology, and give us unprecedented insights into the early and distant Universe.

Figure 1.1 is an example quasar spectrum showing different types of absorption features which are evidence of a range of different types of astronomical objects. These features are superposed onto the quasar's emission spectrum, which is dominated by the Lyman-α (Lyα) emission line caused by electron transitions in neutral hydrogen from the first excited state to the ground state. The rest wavelength of this line is $\lambda_0 = 1216$Å, but it is seen in this figure at $\lambda_{obs} = \lambda_0(1 + z)$ where the redshift of the quasar is $z \approx 3$.

The numerous distinct absorption lines lying shortwards of the strongest emission peak are known as the Lyman-α forest. They are caused by absorption at the same rest wavelength $\lambda_0 = 1216$Å when the electron of a hydrogen atom between us and the quasar is promoted from the ground state to the first excited state. A minority of the lines are instead caused by transitions in heavier elements. Each Lyα line represents absorption by one cloud along the LOS to the quasar. They are seen redshifted by different amounts determined by their distance from us, all less than that of the quasar emission. The term Lyα forest refers to the large number of these absorption lines which are seen in most quasar spectra. Indeed, Lyα forest lines outnumber all other detectable tracers of cosmic structure (Pettini, 2004). They are therefore an indispensable way to study the high redshift Universe.

1.2.2 History

In 1965, Gunn & Peterson suggested that a uniform distribution of neutral hydrogen in the IGM would cause a continuous absorption 'trough' in the spectra of a distant source like a quasar (Gunn and Peterson, 1965). These were seen until it became possible to

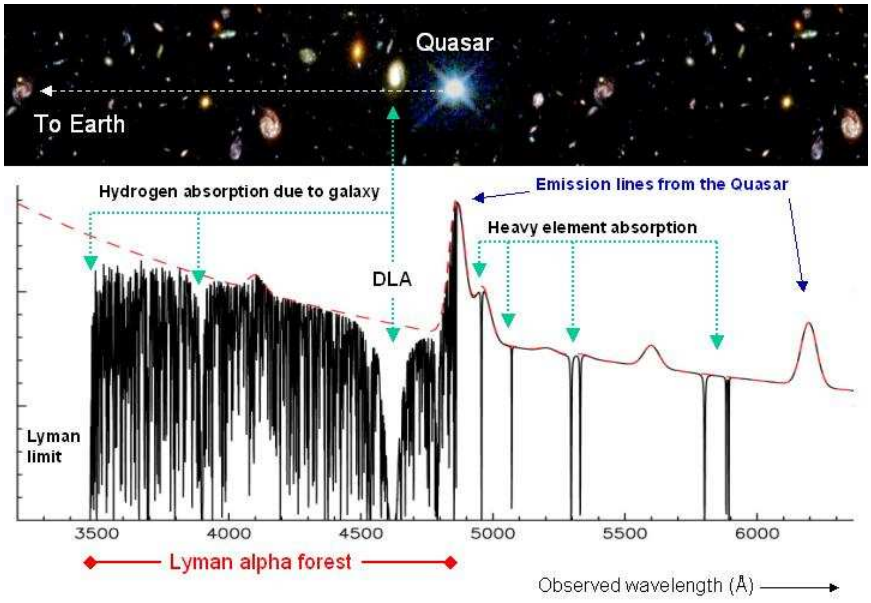

Figure 1.1: Illustration of the spectrum of a quasar at $z \approx 3$. It shows various emission features, and many absorption features including the Lyα forest, a variety of metal lines, and both a damped Lyα line and a sharp cutoff at the Lyman limit caused by the galaxy intercepted by the line-of-sight. Figure by John K. Webb, reproduced with permission.

resolve the troughs into a forest of individual lines (caused by a "*fluctuating* Gunn-Peterson effect"). Lynds (1971) was the first to recognise that these lines were individual hydrogen Lyα lines. Sargent et al. (1980) established the major observational properties of the Lyα forest. They proposed that the lines corresponded to "a population of intergalactic primordial hydrogen clouds".

Great advances in technology for observing absorption features occurred in the mid-1990s. Powerful spectrographs fitted to the new breed of 8–10m ground-based telescopes, and specifically the High Resolution Echelle Spectrograph (HIRES; Vogt et al., 1994) mounted on the Keck I telescope, for the first time allowed observers to fully resolve the profiles of individual absorption lines in the Lyα forest. Around the same time, cosmological simulations of the IGM began to show that the Lyα forest clouds are a natural consequence of hierarchical structure formation.

1.2.3 Absorption Line Characteristics

This section presents some basic theory from spectroscopy to provide an understanding of what information is contained within quasar absorption features. It is useful to consider that for any absorption line, the quantities which might be observed are its minimum intensity, the total intensity removed across the whole line, its shape and the characteristic width.

Absorption basics

These basic features can be derived by considering a beam of quasar light with an initial intensity I_0, travelling in the x direction along our line of sight and passing through an idealised slab of intergalactic gas of thickness L. The rate of change of the intensity $I(x)$ along x is negative and is proportional to both the *number density* $n(x)$ of absorbing atoms and the intensity itself:

$$\frac{dI_\lambda}{dx} = -\sigma_\lambda n(x) I_\lambda(x). \tag{1.4}$$

The *line absorption coefficient* σ_λ represents the cross-section of the absorbing atoms and has units of area. We define the *optical depth* τ_λ as a concise form for the absorption factors:

$$d\tau_\lambda \equiv \sigma_\lambda n(x) dx. \tag{1.5}$$

This gives the optical depth of the whole gas cloud along the line of sight as:

$$\begin{aligned} \tau_\lambda &= \sigma_\lambda \int_0^L n(x) dx \\ &= \sigma_\lambda N(x = L) \end{aligned} \tag{1.6}$$

where the *column density* N is defined as the integral of the number density along the LOS. Both N and τ_λ are functions of x, found at any point along the LOS by integrating to that point. Solving for $I(x)$ by integrating Equation 1.4 shows that the intensity falls exponentially as:

$$I_\lambda(x) = I_{\lambda,0} e^{-\sigma_\lambda N} = I_{\lambda,0} e^{-\tau_\lambda}. \tag{1.7}$$

Line profiles

For any line centred at $\nu_0 = c/\lambda_0$, the frequency-dependent absorption coefficient σ_ν can be split into two factors:

$$\sigma_\nu = \sigma_0 \Phi_\nu. \tag{1.8}$$

The quantum parameters of the atomic transition which causes this line are included in the first factor:

$$\sigma_0 = \left(\frac{\pi e^2}{m_e c}\right)\left[\frac{1}{4\pi\epsilon_0}\right] f_{lu}, \tag{1.9}$$

where e and m_e are the charge and mass of an electron, c is the speed of light and f_{lu} is the upward oscillator strength (Rybicki and Lightman, 1979). The constant in the square brackets, with ϵ_0 the permittivity of free space, is included for SI units and should be left out for cgs units (Meiksin, 2009).

The *broadening function* Φ_ν describes the shape of the line, with a large value near ν_0 and falling off sharply on both sides. It is defined such that the probability that any photon absorbed in the line had a frequency between ν and $\nu + d\nu$ is given by $\Phi_\nu d\nu$, so we see that the broadening function is normalised to give:

$$\int_{-\infty}^{\infty} \Phi_\nu d\nu = 1. \tag{1.10}$$

It is then clear (by substituting Equation 1.10 into the integral of Equation 1.8) that the constant σ_0 is the integral of the frequency-dependent absorption coefficient σ_ν over the line (Spitzer, 1978).

The form of Φ_ν for any line is found by considering the atomic processes involved. The most significant are *natural broadening* and *Doppler broadening* which we will consider now. Other processes such as atomic collisions could also contribute to the broadening. However, in an extremely rarified gas like the IGM their contribution is negligible and they do not change the shape of the lines.

Natural broadening (also known as natural damping) occurs because there is an uncertainty ΔE in the energy of the upper atomic level and this will give an intrinsic width to any absorption line. This is due to the fact that any energy state occupied for a finite time Δt must satisfy the relation $\Delta E \Delta t \sim \hbar$. The uncertainty in the energy of the transition gives the line a Lorentzian profile:

$$\phi_{nat}(\nu) = \frac{1}{\pi}\frac{\delta_k}{{\delta_k}^2 + (\nu - \nu_0)^2}\,, \tag{1.11}$$

where

$$\delta_k = \frac{1}{4\pi}\sum_m A_{km}\,. \tag{1.12}$$

The Einstein coefficients A_{km} give the probability per particle per second of a spontaneous transition to a lower state m.

If the absorbing atoms are in motion, then the resulting line will also have a width due to Doppler broadening. Clearly atoms in the IGM will have some thermal velocity

along the line of sight. Assuming a Maxwell-Boltzmann distribution of velocities, the atoms will have Gaussian distributed velocities along any component. This gives a Gaussian line profile for the Doppler broadening:

$$\phi_{Dopp}(\nu) = \frac{1}{\Delta\nu_D\sqrt{\pi}} \exp\left\{-\frac{(\nu-\nu_0)^2}{(\Delta\nu_D)^2}\right\}. \tag{1.13}$$

The Doppler width $\Delta\nu_D$ is the frequency interval corresponding to the most likely thermal velocity of the absorbing atom along the LOS, given by the Doppler parameter b:

$$\Delta\nu_D = \frac{\nu_0}{c}b, \tag{1.14}$$

$$b = \sqrt{\frac{2k_BT}{m}}. \tag{1.15}$$

It should be noted that the Doppler broadening of the lines is not due exclusively to thermal motions described here ($b = b_{th}$), but is also sensitive to any microturbulence or a difference in velocities across the absorbing cloud as a whole. For example, a Lyα forest cloud that is following the Hubble expansion will have some differential Hubble flow along the length of the cloud which would contribute to the Doppler broadening. Such additional velocity terms can be included in the Doppler profile by adding the velocities in quadrature to the thermal Doppler parameter, e.g.:

$$b = \sqrt{b_{th}^2 + b_{turb}^2}. \tag{1.16}$$

The true line profile is the convolution of the Lorentzian and Gaussian profiles:

$$\Phi_\nu \quad = \quad \phi_{nat} * \phi_{Dopp}\,. \tag{1.17}$$

Using Equations 1.11 and 1.13, and substituting in the form of a Voigt function:

$$H(a,u) \equiv \frac{a}{\pi}\int_{-\infty}^{\infty} \frac{e^{-y^2}}{a^2+(u-y)^2}\,dy\,, \tag{1.18}$$

gives the general form of observed quasar absorption lines, the Voigt profile:

$$\Phi_\nu = \frac{1}{\sqrt{\pi}\Delta\nu_D}H(a,u)\,, \tag{1.19}$$

where $a \equiv \delta_k/\Delta\nu_D$ and $u \equiv (\nu-\nu_0)/\Delta\nu_D$. Close to the line centre ν_0 this profile has a Gaussian shape as more photons are absorbed because of Doppler broadening than natural broadening. This probability falls off exponentially away from the line centre however, leaving Lorentzian wings which only fall off as the inverse square of $\Delta\nu$. Therefore, absorptions away from the line centre tend to be occur because of natural damping.

The shape of an absorption line can therefore tell us the processes involved in the absorption, and gives us information about the conditions in the absorbing IGM gas. It can also tell us the relationship between the strength of the line and the column density of the absorbing cloud. However, things are rarely this simple, and we typically cannot resolve the shape of individual lines. Spectrographs record the convolution of the Voigt line profile with the instrument's own broadening function which is typically wider than the line itself. This means that we lose most of the information that could have been obtained from the line profile. The resolving power of a telescope is normally expressed as $R = \lambda/\Delta\lambda = c/\Delta v$, where $\Delta\lambda$ and Δv are the Full Widths at Half Maximum (FWHM) of the instrument broadening function (in wavelength or velocity units). To resolve the shape of a line, this width must be smaller than the line's FWHM. For example, typical intergalactic Lyα absorption lines have $b \simeq 20$–$30\mathrm{km\,s^{-1}}$, which if we assume a Gaussian distribution of velocities, corresponds to FWHM $= 1.665b \simeq 35$–$50\mathrm{km\,s^{-1}}$ (Pettini, 2006). To resolve these lines, a spectrograph requires $R \gtrsim c/b =$ 8600–6000. Only the very best spectra taken with long observations on 8–10m class telescopes can resolve the shape of these lines, and this has only been possible since the mid-1990s.

The equivalent width

The key for low resolution spectra is to define the *equivalent width* W which is invariant to convolution and so is conserved even when the shape of the line profile is lost. It is a measure of the strength of a line, and should not be confused with the velocity width. The equivalent width of some line is defined as the width in wavelength units of a line of the same total energy but with zero intensity throughout (i.e. the width of a rectangular strip of the spectrum with the same area as the line in question):

$$W = \int_{-\infty}^{\infty} \frac{I_{\lambda,0} - I_\lambda}{I_{\lambda,0}} d\lambda \,. \tag{1.20}$$

This formula can be understood by considering the area of the absorption line as the difference between the integrals of I and I_0 with respect to λ, and dividing this area by the (constant) background intensity I_0 to get the width of a line with zero intensity.

Substituting in I_λ from Equation 1.7 shows that the equivalent width is also a function of the optical depth:

$$W = \int_{-\infty}^{\infty} (1 - e^{-\tau_\lambda}) d\lambda \,. \tag{1.21}$$

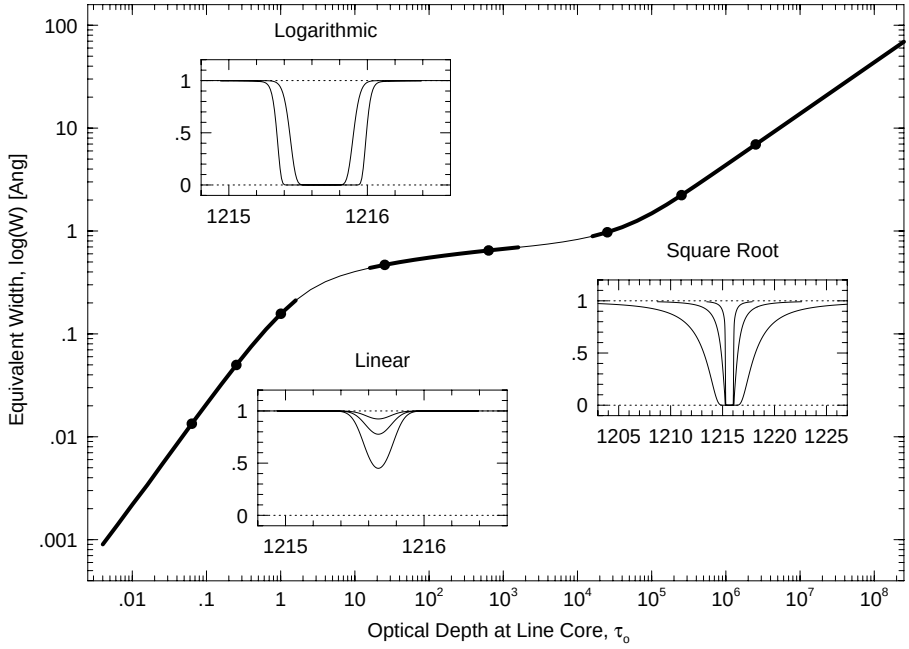

Figure 1.2: The Curve of Growth, plotting W against $\tau(\lambda_0)$. The three smaller panels show example absorption lines in the different regimes. Each of these examples is marked with a point on the Curve of Growth. Note the increased scale of the third panel which shows the wide Lorentzian wings in the square root regime. Figure reproduced with permission from Churchill (2011).

Under the right conditions we can therefore recover the optical depth and thus the column density from the equivalent width, which is conserved even for unresolved spectral lines. However, the dependence of the optical depth on the broadening function means that the relationship between W and N is not trivial.

Integrating Equation 1.21 and plotting the equivalent width W against the optical depth at the line centre $\tau(\lambda_0)$ in Figure 1.2 shows the three different regimes in which an absorption line can be. This *Curve of Growth* shows how the equivalent width grows for Lyα lines of increasing optical depth. The position of any absorption line as a point on this curve dictates the relationship between W which we can measure, and N which we want to recover:

Linear regime For optically thin gas clouds with $\tau(\lambda_0) \ll 1$, thermal and peculiar motions dominate and give a Gaussian shape to the line profile. For clouds with

increasingly large N and τ, the lines stay Gaussian and the equivalent width increases linearly: $W \propto N$.

Logarithmic regime For sufficiently dense clouds with $\tau(\lambda_0) \gtrsim 10$, the absorption line becomes saturated and the cloud is optically thick, absorbing all photons in the line core. If we increase the density and optical depth further, very little additional light is removed and the equivalent width changes only a small amount. Note that in this regime, the equivalent width is sensitive to the Doppler width $\Delta\nu_D$ and so is not a good measure of N: $W \propto \Delta\nu_D \sqrt{\ln(N/\Delta\nu_D)}$.

Square root regime The most dense gas clouds with $\tau(\lambda_0) \gtrsim 10^4$ have wide Lorentzian wings as the optical depth has started to become significant far from the line centre. Increasing the optical depth further will cause the line's equivalent width to grow again as more light is absorbed in the damping wings because of natural broadening: $W \propto \sqrt{N}$.

In order to recover the column density from any line, it is necessary to identify where it sits on the Curve of Growth. This is straightforward for well resolved lines, but for an unresolved line with an equivalent width W, the column density is degenerate with the Doppler width $\Delta\nu_D$. It is sometimes still possible to identify the regime of an unresolved line and thus find the column density N if other lines with a transition to the same energy level can be observed.

1.2.4 Observations and theory

Analysis of Lyα absorption lines gives the column density of neutral hydrogen, N_{HI}, of the individual clouds. Note that this represents only a small fraction ($\sim 10^{-3}$ to $\sim 10^{-6}$) of the gas present in the IGM (Pettini, 2004). The majority is ionised hydrogen, HII, which has no bound electron and so produces no absorption lines. However, for the optically thin gas of the Lyα forest it is possible to analytically calculate what fractions of the total gas will be ionised and neutral. This allows us to correct for the unseen HII to find the total masses of the observed Lyα forest clouds.

The number of absorption systems observed per unit redshift dn/dz is not constant, but evolves with redshift. The trend is for a higher number density of absorbers at higher redshifts, which is consistent with the Universe being smaller at earlier times.

However, there are other effects which influence the evolution of the number of absorbers, and the observational results also show a number of different trends. The Hubble Space Telescope has been used to make observations of the Lyα forest at low redshifts (e.g. Stocke et al., 2004, and references therein). Measurements of the low redshift dn/dz from these observations, are consistent with a simple model of constant comoving number density and a constant proper cross-section for the absorbers. At higher redshifts, the observations show a smooth transition to a faster evolution above $z \sim 1.5$. Simulations show that this is probably due to the higher UVB at earlier epochs. The evolution at $z > 1.5$ also shows a dependence on column density, with the number density of DLAs and Lyman-limit systems evolving more slowly. This shows that the evolution of the IGM's structure must also play a role.

The modern view of the Lyα forest is not gas confined within discrete clouds as was previously believed, but rather a continuous medium of diffuse, ionised gas with a fluctuating density (Theuns, 2005). This is what we call the intergalactic medium, and it represents all of the baryonic matter that is not contained within dense collapsed systems like galaxies, stars and black holes. At the present epoch about 30% of baryons in the Universe are found in the IGM, with another 20–40% in the collisionally ionised 'warm-hot intergalactic medium' (WHIM) which is seen in simulations and is now starting to be detected in UV and X-ray observations (Stocke et al., 2004). The Lyα forest lines are produced in the regions that are slightly more dense, with the column density of the lines giving a measure of the overdensity of those regions. Of course, the term 'cloud' is not unique and it is still applied to these overdense regions.

1.2.5 Types of quasar absorbers

This section gives a summary of the sorts of systems detected in quasar spectra. Almost all of the observed absorption lines are due to hydrogen Lyα absorption, so the different types of lines represent clouds of hydrogen gas in the IGM with different densities.

Lyα forest clouds The majority of the lines that make up the Lyα forest represent overdensities in the IGM with $10^{12}\mathrm{cm}^{-2} \lesssim N(\mathrm{HI}) \lesssim 10^{17}\mathrm{cm}^{-2}$. These low density clouds produce absorption lines whose Voigt profiles are basically Gaussian.

Lyman-limit systems Gas clouds with $N(\mathrm{HI}) \gtrsim 10^{17}\mathrm{cm}^{-2}$ produce a stronger line in the Lyα forest (at $\lambda_{rest} = 1216$Å) but also introduce a new absorption feature. At these column densities, the clouds have enough neutral hydrogen atoms to absorb most

photons with $E_\gamma \geq 13.6$eV. Lyman-limit systems are therefore optically thick to this ionising radiation, which causes a cutoff in the quasar spectrum at the Lyman limit, $\lambda_{rest} = 912$Å. All denser hydrogen clouds will also show this cutoff.

sub-Damped Lyα systems From systems with $N(\mathrm{HI}) \gtrsim 10^{19}\mathrm{cm}^{-2}$, selfshielding means that a high percentage of their hydrogen remains neutral. The Lyα line will begin to show the Lorentzian damping wings as radiation is absorbed at wavelengths away from the line centre. Sub-Damped Lyα systems are a new classification introduced during the last ten years by Péroux et al. (e.g. 2002), for systems detected at $z \gtrsim 3.5$ which fall below the traditional column density threshold for DLAs but contain a significant fraction of the *neutral* gas at high redshift. Also known as super-Lyman limit systems (Wolfe et al., 2005), these objects are distinct from damped Lyα systems because they are still partially ionised.

Damped Lyα systems DLAs have very little ionised hydrogen, and their neutral hydrogen column densities $N(\mathrm{HI})$ are higher than $2 \times 10^{20}\mathrm{cm}^{-2}$. This puts them on the 'square root' part of the Curve of Growth and so they produce absorption lines that are dominated by very wide damping wings. Between redshifts of 1.6 and 5.0, DLAs contain most of neutral gas in the Universe (see the review by Wolfe et al., 2005). It is widely accepted that DLAs could be the progenitors of today's galaxies, seen before the gas had collapsed to stars, as first proposed by Wolfe et al. (1986). There is a great deal of evidence to support this connection, however it is still not certain as the evidence is mostly indirect and there is also much evidence to the contrary (all summarised by Meiksin, 2009).

1.3 Metals in the IGM

Absorption lines from other elements are also seen in quasar absorption spectra, but these 'metal lines' are outnumbered by the Lyα forest lines by more than 50:1 (Pettini, 2006). We can see only the strongest lines of common species, such as OI, CII, CIV, MgII, SiII and FeII. Observations have focused on doublets since these pairs of lines are much easier to identify than single lines. The two most commonly observed doublets, of MgII (with wavelengths $\lambda\lambda$2796, 2803Å) and CIV ($\lambda\lambda$1548, 1551Å), also have the advantages of being some of the strongest observable QSO absorption lines and having wavelengths longer than Lyα ($\lambda = 1216$Å). This latter fact means that the

MgII and CIV absorption lines, along with some other metal lines, lie redward of the Lyα emission peak in a region of the quasar spectra where there are no hydrogen lines. This makes their identification much easier.

The first individual intervening absorbers identified in quasar spectra were metal lines (e.g. Bahcall et al., 1968), not long after Gunn and Peterson's original paper in 1965 on intergalactic absorption. Over the next few years, hydrogen lines were also observed, with Lynds (1971) making detections of associated Lyα and metal lines, and suggesting that the majority of unidentified absorption lines in quasar spectra would be due to Lyα. The number of observations of the Lyα forest increased during the next decade, and the absorption was attributed to either intervening cosmological material or material ejected from the QSOs themselves. Sargent et al. (1980) set out to prove which model was correct, and conducted the first systematic survey of absorption lines. Their data suggested that the hydrogen and metal absorbers made up two separate populations, the first of which Sargent et al. identified as being intergalactic in origin, while the "metal clouds" were attributed to gaseous galactic halos. York et al. (1984) tried to find metal lines associated with the Lyα absorbers of Sargent et al. (1980), whilst considering an extra-galactic origin for metal lines. Although they did not unite the hydrogen and metal populations, they managed to show from the widths of observed CIV lines that the gas temperatures were too low for the gas to be collisionally ionised, suggesting the photoionisation that we now know to be true. Meyer and York (1987) managed to make the first detections of weak CIV lines associated with the population of Lyα systems. Other detections followed, including at low redshifts by the Hubble Space Telescope (e.g. Spinrad et al., 1993). The advent of the HIRES spectrograph (Vogt et al., 1994) on the Keck I telescope made great advances for the field of IGM observations, and allowed the detections of the CIV doublet associated with Lyα clouds in dense systems, with $N(\mathrm{HI}) \gtrsim 10^{14.5}\mathrm{cm}^{-2}$ (Cowie et al., 1995; Tytler et al., 1995; Songaila and Cowie, 1996).

When a metal line is present in a spectrum it always corresponds to a hydrogen Lyα line seen with the same well-defined redshift, caused by absorption in the same gas cloud. Since all but the lightest elements can only be formed by stellar nucleosynthesis, we would naively expect to only see metals nearby to galaxies, in overdense regions of the IGM. However, comparing the column densities of corresponding pairs of hydrogen and metal lines suggests that metals may also exist in underdense regions of the IGM,

far from where we believe there to be any galaxies. The origin of the observed metals is one of the most fundamental questions for IGM observations. We might expect the distribution of metals to be very different depending on whether the stars which produced the metals we see formed at early times (for example if the enrichment was due to the first Population III[1] stars) or whether the responsible stars formed at later times in the strongest overdensities (i.e. in galaxies) (Ellison et al., 2000). These are the two main classes of model, either early or late enrichment, but uncertainty remains even within each type of model. Both models distribute metals by winds which are presumably powered by supernovae and are associated with periods of star-formation (Pettini, 2004). These winds are also linked to the feedback in galaxy formation which is required to suppress excess star formation, although the nature of the connection is still not certain and is an active field of research. Generally, if the metals we observe were seeded into the IGM at early times, they would have formed in smaller pockets of star formation, and may therefore have been more widely distributed through the IGM. Metals produced in galaxies could have been distributed by superwinds strong enough to escape from the potential well of the galaxy, although the wind mechanisms are still not well constrained. If we observe no metal lines in gas below some column density threshold, showing a transition from enriched regions to low density primordial regions, this would provide evidence to constrain our enrichment models. This would most likely favour a galactic origin for the metals, however, some Population III enrichment models also suggest such a metallicity floor. Nonetheless, distinguishing between enrichment models has been one of the main inspirations for attempts to observe metals in low density regions of the IGM and future observations should provide the evidence to solve this question.

It is worth noting that finding metals only nearby to galaxies could instead suggest an inefficient mixing mechanism. The process that mixes stellar ejecta into the Interstellar Medium is still poorly understood, and the process for mixing metals into the IGM is even less well understood (Meiksin, 2009). Kelvin-Helmholtz and Rayleigh-Taylor instabilities may mix enriched gas from winds with primordial gas. However, if the mixing is not complete then regions of higher metallicity and regions of pristine

[1]The first stars in the Universe will have formed from metal-free primordial gas, potentially having very different properties to present-day stars including much higher mass and shorter lifetimes. These metal-free stars are known as Population III to distinguish them from the existing classifications of metal-rich stars (Population I) and metal-poor stars (Population II). The classification is by metallicity not chronology, so Population III stars existed first.

gas will remain. Evidence for this sort of inadequate mixing was found by Schaye et al. (2007).

A number of techniques have been used to search for weak metal lines in low column density systems. A key aspect is attempting to maximise the signal-to-noise ratio (SNR) of the observed spectra. One method for improving the SNR of a spectrum is known as "shift and stack" and involves producing a composite spectrum by stacking sections of the spectrum, having shifted them to the rest frame by lining up each of their Lyα lines. This aligns their other absorption features and reduces the noise. The expected location of metal lines relative to the Lyα line is then searched for a signal. Using this technique, Lu (1991) was able to make a tentative detection of CIV associated with Lyα absorbers (four years before the HIRES spectrograph provided spectra with a sufficiently high SNR to confirm a detection).

Another method for detecting weak CIV features in spectra, which was introduced by Cowie and Songaila (1998), involves measuring the optical depth of each pixel in the Lyα forest, and the optical depth of each pixel at the corresponding CIV wavelength. The distribution of the CIV optical depths as a function of the corresponding HI optical depths is then converted into an estimate of the metallicity as a function of density (Schaye et al., 2003). Originally this technique was used to find the median metallicity, for example by Aguirre et al. (2002). That group also extended the method to measure the full probability distribution of the carbon abundance (Schaye et al., 2003).

Both of these analytical techniques "effectively enhance the sensitivity of the data beyond the normal equivalent-width limits of the spectra" (Ellison et al., 2000). The alternative is to strive to measure higher SNR spectra, by taking longer integrations with the spectrograph. Ellison et al. (2000) used HIRES to record the spectrum of an already well-studied quasar, but roughly doubled the integration time. This technique was successful in detecting many CIV systems. They then presented a comparison of the stacking and pixel techniques, to push their results to detect even weaker lines. Their analysis was sensitive down to column densities as low as $N_{CIV} \simeq 4 \times 10^{11}\mathrm{cm}^{-2}$, and they found CIV absorbers down to this level, in clouds with N_{HI} down to $10^{14}\mathrm{cm}^{-2}$. As expected, the number of metal lines increases for lower column densities. Previous studies, for example by Petitjean and Bergeron (1994) and Songaila (1997), found this trend but with a levelling off of the number of metal lines at low column densities. However, this fall-off was always at the limit of the sensitivity of each survey. Ellison et al. detected systems at lower N_{CIV} to show that the decrease in the number of detections seen in previous results was due to incompleteness. They also saw this same

levelling off at the lowest column densities themselves, but were able to show that this was due to incompleteness. Thus they showed that the power-law column density distribution holds down to at least $N_{CIV} = 10^{11.7}\mathrm{cm}^{-2}$ (a factor of ten lower than previous measurements) and detecting no evidence for a turn-over towards primordial gas at low densities.

This trend has continued, and to date no proof has been found for a floor in the IGM metallicity. Simcoe et al. (2004) focused on measuring only the column density of OVI and CIV lines, so had lower sensitivity than the statistical methods but gained information on the local metallicity field and on any systematic biases. They were also careful to account for nondetections as well as their detections. They found that 60–70% of lines in the Lyα forest are enriched to [O,C/H] $\gtrsim 3.5$, and again saw no evidence of a metallicity floor. The distribution of metallicities can be fit as a lognormal distribution with a mean of 6×10^{-3} solar, and the minimum observed metallicity was around 3×10^{-4} solar. Based on their results they argue against early enrichment by Population III stars. Note that such results are model dependent, and these were calculated using a model of the UV background from Haardt and Madau (1996). This was based on an input power-law spectrum with a mean intensity $J_\nu = J_L(\nu/\nu_L)^{-\alpha}$ and a spectral index of $\alpha = 1.8$, normalised to $J_L = 10^{-21.5}$ erg cm^{-2}s^{-1}Hz^{-1}str^{-1} at the Lyman limit $\nu_L = 3.28 \times 10^{15}$Hz, and propagated through the IGM.

In addition to the important results from Simcoe et al. (2004) just discussed, other general conclusions from recent metal line studies will now be summarised. Firstly, the metallicity of the IGM is typically very low ($\lesssim 1\%$ at $z \sim 3$) compared to solar levels (e.g. Cowie et al., 1995; Schaye et al., 2003). The metallicity increases with the gas density, although there is a large range of observed values of these metal abundances for any given hydrogen density (Schaye et al., 2003; Simcoe et al., 2004).

We can also constrain the redshift evolution of metallicities. Songaila (2001) found that there is not much evolution of N(CIV), the column density of CIV, between $z \approx 5$ and $z \approx 2$, and there is also not much evolution of the carbon abundance from $z \approx 4$ to $z \approx 2$ (Schaye et al., 2003). More recent results push to higher redshifts. In 2006, Simcoe (using the GNIRS spectrograph on the Gemini South telescope) and Ryan-Weber et al. (using the ISAAC spectrograph on UT1 of the VLT) detected two strong CIV features at $z \sim 6$, towards SDSS J1030+0524. Becker et al. (2009) confirmed these detections with HIRES on Keck 1, but in a search of four other sightlines using the NIRSPEC spectrograph, found no CIV systems (compared to a prediction of roughly

13 systems if there was no evolution out to $z \sim 6$). If the column density distribution of CIV absorbers is assumed to be have the same trend as at $z \sim 3$, e.g. the power-law given by Songaila (2001), then this non-detection suggests a drop in the normalisation by a factor of 4.4 . The results also suggest a rapid increase in the amount of CIV between $z \sim 5.3$ and $z \sim 4.5$ which in turn suggests a change in the UVB, ionising more carbon to CIV, or perhaps an increase in the overall IGM metallicity. The different results between different sightlines suggest large-scale variations at $z \sim 6$ in either the level of enrichment or the ionisation state of the gas.

We can also measure the relative abundances of important elements, e.g. the ratio of silicon to carbon in the IGM is seen to be higher than in solar abundances (Aguirre et al., 2004).

Damped Lyα Absorbers have higher metallicities, which evolve from around 3×10^{-2} solar at $z \sim 4$ to 1.5×10^{-1} solar at $z \sim 1$. The few highest observed metallicities are above 3×10^{-1} solar (Wolfe et al., 2005). No DLA is found with a metallicity lower than 2.5×10^{-3} solar. Sub-Damped Lyα Absorbers have even higher metallicities, from 10^{-1} solar to super-solar metallicities, e.g. 5 times solar for zinc (Kulkarni et al., 2007).

The narrow size of metal lines compared to their corresponding hydrogen lines, as well as giving direct estimates of the IGM temperature, also allows them to reveal substructure within the absorbers causing Lyα features (Songaila and Cowie, 1996). Understanding these density features is also important for interpreting the ionisation of metals. Since ion fractions depend on the ionisation parameter (the ratio of number densities of ionising photons to atoms), different substructures could have different ion fractions but giving the same total column density.

Comparing associated metal lines in neighbouring LOS can give measurements of the physical extent of clouds. For example, Ellison et al. (2004) find coherent CIV and SiIV absorbers separated by $\sim$ 100kpc in the multiple LOS towards a gravitationally lensed quasar. They find much smaller coherence scales for lower ionisation systems, e.g. $1.5 - 4.4$kpc for MgII and FeII. Rauch et al. (2001) find coherence scales of around 300pc for CIV systems at $1.5 \lesssim z \lesssim 3$.

The "proximity effect" (Murdoch et al., 1986; Tytler, 1987; Lu et al., 1991) is a well established result in Lyα forest observations, with a relative lack of Lyα absorption features close to the background quasar. This is caused by the quasar's own radiation field locally dominating the UVB and ionising a higher fraction of the hydrogen, leaving less neutral hydrogen to generate an absorption feature. This effect is one of our primary tools for measuring the intensity of the UVB at high redshifts (e.g. Bajtlik

et al., 1988). The equivalent effect is expected in neighbouring lines of sight, with the radiation field of a foreground QSO expected to reduce the number of absorption features seen at the same redshift in the spectrum of a background QSO. This is known as the "transverse proximity effect" (TPE). To date, searches for the TPE in the Lyα forest along neighbouring LOS (e.g. Fernandez-Soto et al., 1995; Crotts and Fang, 1998; Croft, 2004; Schirber et al., 2004) have found no evidence for a reduction in the number of Lyα features. Indeed, most of these surveys detected an increase in the number of features, likely due to the large-scale environments of the quasars, a short or variable lifetime for their radiation, or anisotropic radiation. Gonçalves et al. (2008) search instead for the TPE in metal lines, taking new higher quality spectra of an already well-studied QSO triplet (Q1623+268). For the first time, they claim a detection of the TPE, based on evidence from the metal lines for local enhancements in the radiation field, rather than on counting lines.

Quasars that appear close on the sky to a foreground galaxy, allow us to probe galactic environments. For example, galaxies at $2 \lesssim z \lesssim 3$ show very strong CIV absorption for LOS that pass within 40kpc of the galaxy, and CIV absorption is still seen out to radii of 80kpc (Adelberger et al., 2005). This association between metals and galaxies may well result from the heavy elements being produced in the galaxy's stars, and ejected into the nearby space. However, this is not the only possible interpretation. If instead, the whole IGM was polluted by metals, then the detection of high densities of metals near to galaxies may just reflect the high density of hydrogen in the overdense surroundings of galaxies.

These results show what has been possible, but clearly they all still pose open questions with the possibility of much greater constraints being created by future work. Other questions that remain about the distribution of metals in the IGM include: the extent to which metal density varies with distance from galaxies (Pieri et al., 2006); whether metals are confined primarily to the filaments or the voids of the IGM (Rauch, 1998); what the volume filling factor is for metal enriched regions (30% of the volume of the IGM could be polluted by metals if a mechanism exists for widespread enrichment, but observations of OVI suggest it could be as low as 5%) (Pieri et al., 2006). With so much uncertainty about the distribution of the metals and its underlying processes, it is little wonder that current simulations cannot accurately reproduce observations of metal lines. Improvements in our understanding of the metals in the Lyα forest and improvements in our ability to simulate them will go

hand-in-hand.

Important early models of metal-line absorption systems were made by Bergeron and Stasińska (1986); Verner and Yakovlev (1990); Donahue and Shull (1991); Madau (1991) and Bergeron et al. (1994). Bergeron and Stasińska used the code `PHOTO` (Stasińska, 1984) to create models for interpreting observations taken from the literature. The code computes the transfer of radiation from a constant UV background, through a plane-parallel slab of constant density. The models assume thermal and ionisation equilibrium. Grids of models were produced with different densities, metallicities, and spectral slopes. Comparing observations with the results of the models allowed constraints to be placed on the physical characteristics of the absorbers. For example, the models that fit different observed column density ratios of metal species, put strong constraints on the ionisation parameter U for the observed systems, and all roughly in the range of a few 10^{-4} to a few 10^{-2}. A softer spectrum was found to give higher values of U. Having found U, they then calculated the size of the absorbers by assuming a particular intensity for the ionising radiation, $J_L = 10^{-21}$erg cm^{-2} s^{-1} Hz^{-1} st^{-1}. The thickness of the clouds was found to be 0.2 – 65kpc (which matches the scales found in observations of multiple gravitationally lensed quasars and quasar pairs, suggesting that the value used for J_L is of the correct order of magnitude). The models constrain the metal abundances to be at least 0.01 solar for systems showing CIV and no CII, and a few tenths solar for systems with strong CIV and CII. For a spectral index of $\alpha = 1.5$, N(HI)$<10^{17}$cm^{-2} and $U = 10^{-3}$, they find temperatures from ∼20,000K for a metallicity of 0.01 solar, to ∼8,000K for solar abundances.

Verner and Yakovlev (1990) produced the code `LINESPEC` which calculates the ionisation equilibrium of twelve elements in an optically thin plane-parallel slab of gas, and produces synthetic spectra showing the absorption by these elements of light from a background quasar. The code is much simpler than others since it does not solve for the temperature, instead taking the temperature as an input parameter. This allows the code to be much faster. The aim of the work was to study the impact of the spectral intensity and temperature on absorption spectra. For a high enough spectral intensity, Lyα lines were found to dominate the metal lines, and even be the only lines visible in the UV spectral range. Verner and Yakovlev also noted that strong resonant lines may appear in absorption spectra even when the atoms of that element are mostly in another nearby ion state. Changes in spectra might therefore not exactly follow changes in the distribution of ion states for different temperatures and ionisation parameters.

Donahue and Shull (1991) modelled the ionisation of seven elements plus H_2 in the IGM with their code `THERMAL`. They model only low density systems and ignore radiative transfer since Bergeron and Stasińska (1986) showed that the optical depth does not affect photoionisation models for low column density systems. The code works by iterating between solving the thermal equilibrium, the ionisation equilibrium and the density. Models are produced for a range of temperatures, metallicities and for two different model QSO spectra. They produce column density ratios of clouds with different values of U and a range of metallicities. They compare their results with a few recent observations, placing new constraints on the derived metallicities, temperatures, etc. They also find a stable molecular phase in Lyα clouds with $10^{-7} \lesssim U \lesssim 10^{-5}$ and $n(H_2)/n(HI) \approx 10^{-2}$.

Madau (1991) made a grid of models using `Cloudy` as in earlier work, but also included the effect of earlier IGM absorption on the ionising spectrum. The aim of the work was to assess the possibility that the ionising background was dominated by flux from hot stars in young galaxies rather than from quasars. The models are run for different values of N(HI), metallicities and spectral shapes. One of the conclusions was that such a starburst spectrum is capable of reproducing the observed ionisation of carbon absorption systems.

Bergeron et al. (1994) analyse 18 absorbers from Hubble Space Telescope spectra. One absorber shows a wide range of ionisation states from MgII to OVI, which cannot be reproduced by a photoionisation model with a single region of constant density and a quasar-like spectrum. They therefore model this absorber using a modified version of the code `Nebula`, as a spherical cloud around a central source (the absorbing galaxy, which has been observed for the absorber in question) with the addition of an external diffuse radiation field. The cloud is given two regions, one with density that varies with distance, embedded within a larger region of constant density. They produce a model with an outer region ∼70kpc wide, with $n_H \sim 3 \times 10^{-4}\mathrm{cm}^{-3}$, which gives the OVI absorption, and an inner region ∼7kpc wide, with n_H around 20 times higher, giving the MgII absorption. The model gives a high overall metal abundance of ∼0.5 solar and CIV absorption is produced in both regions.

Recent examples of modelling metal systems include the work of Simcoe et al. (2006) and Agafonova et al. (2007, and references therein), with both groups using `Cloudy`. Simcoe et al. studied absorption systems along the line of sight towards a single quasar, using accurate spectra from Keck HIRES along with observations of galaxies close to the LOS taken from a galaxy survey by Steidel et al. (2004, using Keck LRIS-B).

Many metal lines are identified and grouped into small substructures within six main absorption systems. Grids of models were performed for different densities and total metallicities, using a UV background spectrum along with a starburst galaxy spectrum for those systems nearest to known galaxies. A best-fit density was chosen for each system by a χ^2 test to select the model which best matched the observed line ratios of ions from the same element (e.g. CII/CIV and SiIII/SiIV). The ion fractions from that model were then combined with this best-fit density and the observed column densities to calculate a mean path-length of the LOS through the absorbing system. For systems with line ratios of individual elements that could independently constrain the ionisation parameter, the ratio of Si to C was varied in the models and the resulting ratio of SiIV/CIV was used to constrain the abundance ratio of these elements. Three of the observed absorption systems are found to be very small (with LOS path-lengths $\lesssim$ 1kpc), dense (with $\rho/\bar{\rho} \sim$1000), and metal-rich (with metallicities at least around 0.1 to 0.3 solar), two of which are located within 100–200h_{71}^{-1} physical kpc of high-redshift galaxies. These are attributed to a population of small, dense sheets or bubbles near to galaxies caused by shocks ploughing through overdense filaments of gas. Outside of the volume containing these systems, the metallicity drops to the background IGM level, and at $\gtrsim$ 300 physical kpc, the intergalactic gas density is seen to drop off.

Agafonova et al. (2007) model IGM metal systems as part of a study to constrain the shape of the UVB, using observed metal lines from the LOS to 3 quasars. They parameterise the shape of the UVB with seven parameters, and use an iterative process with `Cloudy` photoionisation models to determine the ionising spectrum for each of the absorbing systems. The dependence of the ion fractions on density were found from models of a given system, and a Monte Carlo Inversion procedure was used to find the best values of the relative abundances and absolute metallicity of the system. If these values did not match the inputs used for the models, the process was repeated using the new values as model inputs, and this continued until the abundances converged. However, if a consistent solution could not be found, the spectral shape was modified, and the entire process was iterated until a preferred spectrum was found that gave a converging solution for the system's abundances. The results show fluctuations of the UVB in the studied redshift range, $1.8 < z < 2.94$, which Agafonova et al. attribute to different factors depending on redshift. This variability around $2.4 < z < 2.94$ is caused by absorption in the clumpy IGM, which at $z \lesssim 1.8$ the UVB fluctuations are due to a diversity in intrinsic quasar spectra. They conclude that their recovered spectra do not indicate a significant contribution to the UVB from starburst galaxies.

All of these models have assumed that the IGM is in a state of ionisation equilibrium. This means that any non-equilibrium effects have been neglected (e.g. any changes in conditions on timescales shorter than the time to reach equilibrium). It is possible however that some observations probe regions which might be out of equilibrium. One obvious example is observations of absorption close to a quasar, seen in the spectrum of a second background quasar that is nearby on the sky. The lifetimes of quasars are not yet well understood: an AGN may shine as a quasar for 10^8 years but if the luminosity was variable during this time, we can imagine a bright phase on a timescale 10 or 100 times shorter. Observations of neighbouring LOS could therefore probe regions of the IGM which have experienced varying conditions. Any species which takes longer to reach ionisation equilibrium will appear with its ionisation due to an earlier luminosity than the ionisation of other elements. Assuming that the observed IGM is in equilibrium would therefore misinterpret such observations.

To accurately model the ionisation of the IGM, especially around shortlived sources such as AGN or perhaps massive stars in starburst galaxies, therefore may require modelling the time-dependent effects by relaxing the assumption of ionisation equilibrium. Interpreting future observations using such models could then provide evidence about time-varying sources of ionising radiation.

1.4 Simulations of the IGM

The study of the intergalactic medium is based on observations, theoretical work and numerical simulations. Since we cannot examine the IGM directly, simulations are particularly important in this field of research, and comparing simulations to observations is essential for our understanding. These comparisons help us to appreciate how different parameters and effects govern the properties of the Lyα forest clouds that we see. Without simulations we would not have the same ability to study the influence on the IGM of parameters like the matter-power spectrum, reionisation history, ionising background and the nature of dark matter. Much of the discussion in this chapter comes from the excellent recent review of numerical simulations of quasar absorbers written by Tom Theuns (2005).

Simulations of the IGM, as with those in other areas of cosmology, grow ever larger and more detailed as technology develops. A variety of different conceptual approaches for simulations have been developed, corresponding to different mathematical treatments of the problem. Whilst small codes that are run on a desktop computer can still

produce interesting results, research groups now often run much larger simulations in parallel across a number of processors. Simulations may take weeks to run on large supercomputers, and produce terabytes of data. Analysis of the output can be a very large task, but can offer us unique insights into the workings of the IGM.

The test for simulations is comparing their predictions to observations of the Lyα forest. Continual refinement of the simulations allows us to better reproduce what we observe, and at the same time reveals how the physical processes being modelled affect the properties of the IGM. Simulations are also key in determining the extent to which observations can constrain the parameters.

1.4.1 Simulation Methods

Fundamentally, a numerical simulation of the IGM follows the properties such as position and energy of the matter in a volume for a period of time. The initial conditions are typically generated by simulating a volume of primordial density perturbations following some Gaussian random field, and then evolving it according to the chosen cosmology. The resulting matter distribution is used as the starting point for the simulation proper. This distribution is modified according to difference schemes formed from the differential equations governing the conservation of mass, momentum and energy in a self-gravitating fluid (Landau and Lifshitz, 1959). The difference schemes are evaluated over a large number of points in the volume, and steps in time.

The two main types of difference schemes used in simulations of the IGM are Eulerian and Lagrangian. The former solves the equations at a fixed grid of points (also called cells, for the small volumes each point represents). The latter has 'cells' that move with the fluid, therefore known as particles. These are not typically on the scale of the true physical particles of the system being modelled, for example stars in a galaxy or the individual atoms of the IGM, but rather are 'super-particles' each representing the properties of a group of particles. Often Eulerian codes give better resolution of under-dense regions, whilst Lagrangian codes generally resolve high-density regions better (Theuns, 2005).

Large simulations run today using Eulerian methods are not normally solved on a uniform grid throughout the whole volume. Whilst it is computationally the most simple idea, a uniform grid can be inefficient since the same spatial resolution is used in empty regions as in galaxy-forming areas where the largest changes occur. Instead, additional resolution can be given at interesting sites by using an increased number

of smaller cells. In a local simulation of objects such as galaxies that are at specified locations, the additional cells can be established wherever desired before the code is run. For larger Eulerian simulations of the IGM, a method known as Adaptive Mesh Refinement (AMR) is often used. This varies the density of grid points throughout the volume whilst the simulation is running, according to some specified criterion such as keeping the mean mass per cell constant.

Lagrangian codes do not all treat the simulation simply as a system of particles. The inclusion of a grid in Particle-Mesh (PM) codes can greatly increase the computation speeds (Hockney and Eastwood, 1988). To solve the gravitational potential of the particles, the mass density field is approximated by values at the mesh points, calculated from the masses of the nearest particles. Fast Fourier Transform methods can then be used to calculate the gravitational potential on the grid, which is then interpolated to the particle positions to find the forces they experience. This method does not give the same resolution of the potential and force fields as found by solving at every particle, but can vastly increase the speed of computation. PM codes are only valid for systems with long range forces acting over greater distances than the mesh size, but this suits IGM simulations well.

The resolution currently available in hydrodynamical simulations on cosmological scales is not nearly small enough to resolve areas where star formation occurs. Therefore, this type of process cannot be simulated by the codes themselves. Instead, star formation is included by means of some recipe that tries to recreate the global effect. The recipe specifies that 'cold dense gas' will be converted into stars at some given rate and efficiency, manually tailored to give a realistic looking approximation to the underlying effect. Star formation is just one example of 'sub-grid' physics that has to be applied to simulations in this way. Other processes that originate on the scale of stars including metal production, feedback from star formation, cosmic rays, winds driven by supernovae and magnetic fields. Presently they all can only be included as sub-grid physics.

Other essential features of simulations that have to be calculated individually include the treatment of shocks, cooling effects and the ionising background radiation. The background radiation can be imposed with some assumed spectrum and evolution behaviour such as that given by Haardt and Madau (1996). Only with recent increases in computer speed has it become practical to instead include radiative transfer (RT) codes in simulations to solve for the propagation of radiation through the simulation volume (see next section).

The causes of processes included as sub-grid physics are mostly known, but their large scale effects are often not well understood. This limits the accuracy of simulations; for example, current simulations fail to recreate the higher column density lines seen in absorption spectra because feedback effects, radiative cooling and self-shielding all become more important at higher densities (Theuns, 2005). To increase our understanding of the processes at work, we must improve the realism of our simulations.

1.4.2 Current IGM Simulations

Much of the current simulation work is focused on using better models of the baryonic physics. The aim is to try to improve the agreement with observations, and in particular, one goal is to better reproduce the detailed density- and redshift-dependent metal distribution which are sensitive to these sub-grid processes.

For example, the recent simulation by Oppenheimer and Davé (2008) aimed at reproducing the effect of feedback from star formation on the distribution of mass, metals and energy. They use `GADGET-2` (Springel, 2005) with a momentum-driven galactic wind model (as would be powered by stellar UV radiation pressure rather than supernovae) which gave the best results in their earlier comparison of models (Oppenheimer and Davé, 2006). The wind model is based on Murray et al. (2005) and implemented using a method by Springel and Hernquist (2003a) which gives SPH particles a velocity kick. The simulation separately tracks C, O, Si and Fe from type Ia and type II supernovae and from AGB stars. They find that the wind material typically accretes back on to the galaxy it was ejected from, so that metals in the IGM may not stay there forever. High redshift galaxies are able to enrich a larger comoving volume with metals returning to galaxies at lower redshifts, whereas sizeable galaxies at lower redshifts are typically not able to eject their metals out of their halo. They find that the wind energy can exceed the expected total energy output of supernovae in the high mass galaxies modelled in their simulations. This supports the idea of an alternative or additional source of wind energy (such as photons from young stars).

Another example is Nagamine et al. (2004a,b) who study the abundance, metallicity and star formation rate of DLAs in cosmological SPH simulations (originally run by Springel and Hernquist (2003b) using `GADGET`), which use star formation and supernova feedback models, including metal tracking, and a wind model (as powered by supernovae). Their findings include a median DLA metallicity an order of magnitude higher than typically observed. This could show an inadequate treatment of the feedback in

the simulations, or it might show that observations are missing the majority of high metallicity DLAs. As some simulations become more focused on processes such as feedback that affect a wide range of scales (e.g. from IGM pollution to galaxy formation), so those individual simulations become of use for studying a wide range of effects. The simulations by Springel and Hernquist (2003b) have also been used to study the evolution of the cosmic star formation rate, Lyman-break galaxies, disk formation, 21cm emission from the IGM, and extremely red high-redshift galaxies (Nagamine et al., 2005, and references therein).

Another focus of recent work is improving the dynamic range that is simulated, to try and unite the size of cosmological simulations with the fine resolution of galactic scale simulations. At smaller scales, Yoshida et al. (2006) have simulated the formation of the first stars in the Universe within a volume $(0.3\text{Mpc})^3$, by zooming in on progressively smaller regions down ten orders of magnitude. The formation of the first stars may be intrinsically linked with the history of the IGM, as they have the potential to have been the sources both of the photons the triggered Reionisation and of the metals that pollute the IGM. Reed et al. (2005) also did a zoomed simulation of the first stars forming, in a larger cosmological volume of $(479h^{-1}\text{Mpc})^3$.

Another recent project modelling a similar volume, is the *Galaxies-Intergalactic Medium Interaction Calculation* (`GIMIC`) simulations by the Virgo Consortium (Crain et al., 2009). They re-simulate five spherical regions of radius $\sim 20h^{-1}$Mpc taken from the $(500h^{-1}\text{Mpc})^3$ Millennium Simulation volume (Springel et al., 2005), with the addition of full hydrodynamics including gas cooling, heating from photoionisation by an imposed ionising background, star formation, supernova feedback and galactic winds, but no AGN feedback. Although only zooming once, these simulations still offer a very large dynamic range because of their high resolution. The large scale of the original simulation allows accurate integration of the simulations to $z = 0$. The individual simulations are chosen to contain a variety of densities and thus sample the full range of large-scale environments. Combining their results allows statistical properties to be estimated for the wider simulation volume. One paper has been released to date, which focuses on the star formation properties in the simulations. Future results should shed new light on the evolution of the IGM and its relationship with the galaxies it surrounds.

Another area of continued research is the inclusion of radiative-transfer (RT) models into IGM simulations, using some approximation to the full RT equations. Most work has been done using ray-tracing methods (e.g. Bolton et al., 2004; Mellema et al., 2006)

or methods that take moments of the radiation field (e.g. Gnedin and Abel, 2001), often as post-processing on an N-body simulation. Typically the computational intensity has limited the simulation size for these calculations, although Iliev et al. (2006) achieved a large simulation with a volume $(100h^{-1}\mathrm{Mpc})^3$ by developing a fast RT code. A more common approach has been to study a particular simplified model. For example, Tittley and Meiksin (2007) and Paschos et al. (2007) study the ionisation and temperature of the IGM during the reionisation of HeII to HeIII. Tittley and Meiksin solve the RT for a single source and only along 256 lines of sight. Paschos et al. solve only for the ionisation of HeII and only model the radiation field at three frequencies. Modelling these specific cases allow the inclusion of computationally intensive RT routines, without making the simulations too computationally expensive.

1.5 Previous Astrophysical Time-dependent Ionisation Models

A number of papers have been published since the 1970s which have modelled the time-dependent ionisation of metal-enriched gas in a non-equilibrium state in various astrophysical settings. None have yet addressed the photoionised IGM studied in the present work, but some of the more recent papers have investigated ionisation at higher temperatures in the collisionally ionised warm-hot intergalactic medium (WHIM). As will now be described, previous non-equilibrium metal-ionisation work in astronomy has focussed on modelling cooling gas in a wide variety of systems, most of which are collisionally ionised.

Early time-dependent ionisation and cooling models, for example by Bottcher et al. (1970) or Jura and Dalgarno (1972), did not include any metals. An early astrophysics paper which modelled the ionisation of oxygen and silicon without the standard assumption of a steady-state equilibrium was by Kafatos and Tucker (1972) studying solar flares. The following year Kafatos (1973) applied the same techniques to model the ionisation and cooling of interstellar gas cooling after a supernova. This work to calculate the cooling functions of a hot, diffuse interstellar plasma was repeated and extended by Shapiro and Moore (1976) and others including Edgar and Chevalier (1986), Schmutzler and Tscharnuter (1993), Sutherland and Dopita (1993) and Smith et al. (1996). The cooling functions calculated by Sutherland and Dopita (1993) became the standard reference used by many authors, and are still in use today (for example, by

Tescari et al., 2010).

Perna and Lazzati (2002) included dust destruction into a photoionisation code for modelling the environment of a gamma-ray burst (GRB). Heckman et al. (2002) interpret observations of OVI absorption line systems from the Galactic disk, the Galactic halo, the Large and Small Magellanic Clouds, starburst galaxies, and the WHIM. They follow Edgar and Chevalier (1986) in using the cooling functions of Sutherland and Dopita (1993) to calculate the densities of other abundant ions in collisionally ionised intergalactic clouds. Cen and Fang (2006) include non-equilibrium ionisation of the oxygen fractions OV–OIX into their numerical simulations of the WHIM. Yoshikawa and Sasaki (2006) do the same (as well as presenting some simple models discussed in Chapter 2), and although they include seven different metals in their code, they again present results only for the highly ionised states of oxygen. Gnat and Sternberg (2007) model the ionisation and cooling of collisionally ionised clouds relevant to both hot gas in the Galactic halo and in the WHIM. They later extended this work to include effects in the regions behind fast, radiative shock-waves (Gnat and Sternberg, 2009). Henney et al. (2005, 2007) add steady-state gas dynamics into the plasma physics code `Cloudy`, and model different types of ionisation fronts in HII regions and planetary nebulae, including time-dependent ionisation of the metals.

Chapter 2

Time-Dependent Ionisation Rate-Equations Algorithm (`Timedep`)

The intergalactic medium is highly ionised, but the ions in such a plasma constantly undergo recombinations and ionisations. We typically only see absorption lines from certain states of a given element. The rates of ionisation and recombination for each of the states govern which ionisation states are most abundant. These rates can be calculated for a given set of environmental conditions (temperature, flux of ionising radiation, etc.) by approximations to the atomic quantum mechanics. When simulating the IGM, it is standard to assume that all elements are in ionisation equilibrium, with the fraction of atoms in each ionisation state in equilibrium at any time. These ion fractions are calculated by balancing the rates of all the ionisation and recombination processes which move atoms into a given state against the rates of processes moving atoms out of this state, and solving for the equilibrium abundances. However, this assumption of ionisation equilibrium might not always be justified.

If the timescales for a given species to reach ionisation equilibrium are long, then it may be unrealistic to assume equilibrium for that species in simulations of the IGM. The IGM that we observe (and simulate) has only existed in its current form for a finite

length of time. Indeed, the physical conditions of the IGM which dictate the ionisation structure may vary locally over relatively short timescales, for example when driven by the turning on of a quasar.

To investigate this topic, my first aim was to develop an algorithm to model the time-dependent ionisation of metals in the IGM. The next goal was to use this algorithm to test whether there are conditions in the IGM that require time-dependent modelling to be studied accurately. The other main aim was to provide an example of using this new algorithm in a simulation to give fresh scientific insight into the ionisation of metals in the IGM.

The question of modelling time-dependent ionisation of metals is topical in light of continuing improvements in computing speeds. In the past it may have been prohibitively time-consuming to calculate the ionisation and recombination rates and to solve for the ion fractions at each step of a simulation. Previous IGM simulations have always made the simplifying assumption of ionisation equilibrium, so these rates and the ion fractions did not need to be followed with time. As computing power increases it is always possible to include more physics into our simulation models. It is now conceivable to include the full ionisation calculations, and so it is necessary to test the need to do so. For a general discussion of modelling time-dependent processes in plasmas, see Seager (2001).

In this chapter I discuss writing a programme to solve time-dependent rate equations for ionisation and recombination processes. By integrating these differential equations over time, the change in ionisation fractions can be studied. Section 2.1 presents the algorithm developed from the rate equations, and Section 2.2 discusses the two different integration schemes that have been used in the programme written to solve the algorithm. Section 2.3 explains the input parameters required by the programme, and Section 2.4 explains the different atomic reactions included in the algorithm and lists the sources of the data used. Section 2.5 details other features included in the programme.

2.1 `Timedep` Algorithm

An algorithm was developed to solve for the ionisation fractions f_{ij} of a given element as a function of time. The rate of change $\dot{f}_{ij}$ of each ion fraction at each timestep is calculated as the sum of the rates of ionisation and recombination to that state, minus the sum of the recombination and ionisation away from that state. The fractions are

each updated to some new time by integrating these ordinary differential equations with one of the schemes discussed below in Section 2.2. An adaptive timestep length was calculated on each iteration to give accurate resolution for the evolution of the ionisation states over time.

I wrote a programme in C to run the algorithm, referred to as the `Timedep` code. It reads in tables of publicly available atomic data (specifically, parameters for fits to the rates of various ionisation and recombination processes), calculates the rates, and then performs the time integration of the rate equations for either a given number of steps, a given length of time or until some equilibrium condition is met. It was written to be as general as possible, and can take any combination of the first thirty elements (hydrogen to zinc) with densities specified by the user. Values of the ion fractions are recorded throughout for analysis.

Some numerical approximations and the notation used below were taken from Verner and Yakovlev (1990, V&Y hereafter). Equation 2.1 is the main rate equation used by the `Timedep` code, and was derived from the general equation of ionisation balancing given in V&Y's equation (4).

$$\begin{aligned}\dot{f}_{ij} = {} & f_{ij+1}\left[n_e(r_{ij}+d_{ij}) + n_{11}r_{ij}^{H} + n_{21}r_{ij}^{He}\right] + \\ & f_{ij-1}\left[n_e(c_{ij-1}+a_{ij-1}) + n_{12}c_{ij-1}^{H} + n_{22}c_{ij-1}^{He} + p_{ij-1}\right] + \sum_{l=1}^{j-2} f_{il}q_{ilj} - \\ & f_{ij}\left[n_e(c_{ij}+a_{ij}+r_{ij-1}+d_{ij-1}) + n_{12}c_{ij}^{H} + n_{22}c_{ij}^{He} + n_{11}r_{ij-1}^{H} + n_{21}r_{ij-1}^{He} + p_{ij} + \sum_{k=j+2}^{J_i} q_{ijk}\right]\end{aligned} \tag{2.1}$$

The ion fraction f_{ij} is the fraction of atoms of the element i that are in the ionisation state j. It can be calculated as the ratio $f_{ij} = n_{ij}/n_i$ where n_{ij} is the number density of atoms in a given state and n_i is the total number density of the element. The possible ionisation states go from the neutral atom ($j = 1$) to the fully stripped ion ($j = J_i$). For example, helium has $j = 1$, 2 or 3 corresponding to He^0, He^+ and He^{2+}, hereafter HeI, HeII and HeIII[1]. n_e is the number density of electrons. All remaining terms are the rate coefficients for the ten atomic processes included in the code: c_{ij} is the collisional ionisation rate; p_{ij} is the photoionisation rate (without Auger-electron

[1]Throughout the rest of this thesis I will follow the convention in modern IGM studies of referring to physical ions using Roman numeral notation. However, this notation technically refers to spectral lines. The distinction is important for emission line studies where one spectral line can be emitted by two different ions, either by recombination or collisional excitation, but there is no such ambiguity for absorption studies. See for example, Gary Ferland's note on the `Cloudy` website at http://www.nublado.org/etc/cii_vs_cp.htm

ejection); q_{ijk} is the ionisation rate (from a state j to a final state $k \geq j+2$) due to Auger-electron ejection after a photoionisation; a_{ij} is the autoionisation rate; r_{ij} is the radiative recombination rate; d_{ij} is the dielectronic recombination rate; c_{ij}^{H} and c_{ij}^{He} are the charge transfer ionisation rates with HII and HeII; and r_{ij}^{H} and r_{ij}^{He} are the charge transfer recombination rates with HI and HeI. Details of these processes and the sources of the data used to calculate the rates, are given below in Section 2.4.

The only elements not following Equation 2.1 are hydrogen and helium. These are treated separately since they feature in the charge transfer processes included in the code. The rate equations for the two states of hydrogen, taken from V&Y's equation (6), are:

$$\begin{aligned} \dot{f}_{11} &= f_{12}\left[n_e r_{11} + \sum_{i\neq 1}\sum_{j=1}^{J_i-1} n_{ij} c_{ij}^{H}\right] - f_{11}\left[p_{11} + n_e c_{11} + \sum_{i\neq 1}\sum_{j=2}^{J_i} n_{ij} r_{ij-1}^{H}\right] \\ \dot{f}_{12} &= -\dot{f}_{11} \end{aligned} \tag{2.2}$$

Each of the charge transfer terms involves a sum over every state of all of the other elements. For example, the recombination rate for hydrogen includes contributions from the rate of charge transfer ionisation of every element from helium to zinc.

The helium rate equations are:

$$\begin{aligned} \dot{f}_{21} &= f_{22}\left[n_e(r_{21}+d_{21}) + \sum_{i\neq 2}\sum_{j=1}^{J_i-1} n_{ij} c_{ij}^{He}\right] - f_{21}\left[p_{21} + n_e(c_{21}+a_{21}) + \sum_{i\neq 2}\sum_{j=2}^{J_i} n_{ij} r_{ij-1}^{He} + q_{213}\right] \\ \dot{f}_{22} &= -\dot{f}_{21} - \dot{f}_{23} \\ \dot{f}_{23} &= f_{22}\left[p_{22} + n_e(c_{22}+a_{22}) + n_{12} c_{22}^{H}\right] + f_{21} q_{213} - f_{23}\left[n_e(r_{22}+d_{22}) + n_{11} r_{22}^{H}\right] \end{aligned} \tag{2.3}$$

As an aid to visualising the problem being solved, it is useful to also see the system of Equations 2.1 for each state of one chemical element, written together as a matrix equation. As an example, the system of ordinary differential equations to be solved for carbon is:

$$\begin{bmatrix} \dot{f}_{61} \\ \dot{f}_{62} \\ \dot{f}_{63} \\ \dot{f}_{64} \\ \dot{f}_{65} \\ \dot{f}_{66} \\ 1 \end{bmatrix} = \begin{bmatrix} -(I_{61}+q_{613}) & R_{61} & 0 & 0 & 0 & 0 & 0 \\ I_{61} & -(I_{62}+R_{61}+q_{624}) & R_{62} & 0 & 0 & 0 & 0 \\ q_{613} & I_{62} & -(I_{63}+R_{62}+q_{635}) & R_{63} & 0 & 0 & 0 \\ 0 & q_{624} & I_{63} & -(I_{64}+R_{63}) & R_{64} & 0 & 0 \\ 0 & 0 & q_{635} & I_{64} & -(I_{65}+R_{64}) & R_{65} & 0 \\ 0 & 0 & 0 & 0 & I_{65} & -(I_{66}+R_{65}) & R_{66} \\ 1 & 1 & 1 & 1 & 1 & 1 & 1 \end{bmatrix} \begin{bmatrix} f_{61} \\ f_{62} \\ f_{63} \\ f_{64} \\ f_{65} \\ f_{66} \\ f_{67} \end{bmatrix}. \tag{2.4}$$

Equation 2.4: An example of the system of ordinary differential equations for solving the time-dependent ionisation of one element (in this case, carbon).

Here, the ionisation and recombination rates have been grouped for legibility, using the shorthand, $I_j = n_e(c_{ij} + a_{ij}) + n_{12}c_{ij}^H + n_{22}c_{ij}^{He} + p_{ij}$ and $R_j = n_e(r_{ij} + d_{ij}) + n_{11}r_{ij}^H + n_{21}r_{ij}^{He}$. The matrix is close to being tridiagonal, only differing in two ways. Firstly, Auger-electron ejection transfers atoms between non-neighbouring states. Note that strictly the whole lower-left half of the matrix should have q_{ilj} rates instead of zeros, but only the non-zero rates for carbon have been shown to illustrate that most Auger rates are zero. Secondly, the equation for the rate-of-change of one ion fraction (here, the last line of the matrix) is replaced with the normalisation equation, such that the fractions sum to unity. Without this, the full set of Equations 2.1 are not linearly independent. This normalisation equation is equivalent to those in Equations 2.2 and 2.3. Assuming ionisation equilibrium makes the rates-of-change on the left-hand side equal to zero. Consider that without the normalisation equation, this would have made Equation 2.4 into a homogenous set of linear equations. All of the above rate equations can also be formulated with number densities n_{ij} instead of ion fractions f_{ij}, by multiplying through each term by the total number density n_i of the element being modelled. The matrix equation 2.4 would then become $\dot{\mathbf{n}}_i = \mathbf{R}_i \cdot \mathbf{n}_i$ where $\dot{\mathbf{n}}_i$ and $\mathbf{n}_i$ are the vectors of $\dot{n}_{ij}$ and n_{ij} values respectively, and $\mathbf{R}_i$ is exactly the same matrix of rate coefficients as above.

The number density of electrons is calculated at the start of each timestep. As in V&Y's equation (5), the contribution from ionised metals is neglected and n_e is approximated from the number densities of the ionised hydrogen and helium states:

$$n_e = n_{12} + n_{22} + 2n_{23} \tag{2.5}$$

This approximation that the metals give a negligible contribution to the free electron density is valid because of their small abundances. Typical metal abundances in the IGM can be less than around 1% solar at $z \sim 3$ (e.g. Cowie et al., 1995; Schaye et al., 2003) which for even the most abundant metal, oxygen, means less than around five atoms per million of hydrogen. To give a sizeable contribution (e.g. 5%) to the free electron density, oxygen which might typically be ionised to OVI (for example, with a temperature of 10^4K, density of $n_H = 10^{-4}\mathrm{cm}^{-3}$, and a UV background with a spectral index $\alpha = 1.5$ and mean intensity at the Lyman edge of $3 \times 10^{-22}\,\mathrm{erg\,cm^{-2}s^{-1}str^{-1}Hz^{-1}}$), would need an abundance of over 20 times solar which is highly unlikely. Conversely, with a typical 1% solar abundance of around five atoms per million of hydrogen, the maximum contribution to the electron density by fully stripping all of the electrons from each atom would be 0.004%. Even this tiny contribution could only be approached with

extremely high temperatures or a very hard spectrum. Clearly for most common conditions in the IGM, the contribution of the metals to the electron density is negligible. It is worth noting however, that other regimes do exist where this assumption is not true. For example, in regions of neutral hydrogen can exist with a soft spectrum that is still able to ionise the first states of elements such as C, Mg, Si and Fe since they have photoionisation thresholds at lower energies than H. In such a regime, the only free electrons would come from the metals, but this sort of regime is not being modelled with the `Timedep` code. Another realistic regime in which metals may also make their largest contribution to the free electron density (but again, which is not being modelled here), is in dense knots of high-metallicity gas. Poor mixing of metals into the IGM will produce an inhomogenous distribution. Clouds with poorly mixed metals have been observed with metallicities greater than around solar (Schaye et al., 2007), and here the metals will give a higher contribution to the electron density that on average throughout the IGM.

Another key assumption is that the time-dependent ionisation and recombination do not contribute significantly to the heating or cooling of the gas. Because of this assumption, the `Timedep` models that are presented all have fixed thermal histories, with either a constant temperature, or an evolving temperature calculated by a simulation code, with heating or cooling contributions from ionisation processes only included for hydrogen and helium. A more self-consistent method would be to have `Timedep` continuously update the temperature with contributions from the metals while the code models the ionisation. This is necessary when modelling many astrophysical regimes as metals can be very important coolants, removing energy from gas clouds more efficiently than atomic hydrogen can. However, the metallicity in the IGM is sufficiently low that it is appropriate to assume that the atomic processes calculated by `Timedep` for the metals give a negligible contribution to cooling or heating. Once again, dense knots of high metallicity gas would have a much higher contribution to their cooling from metals, but these are not being modelled with `Timedep`.

2.2 Integration Schemes

2.2.1 Euler's method

The original integration scheme included in the `Timedep` code for updating the ionisation fractions is *Euler's method*. At each timestep (n), the fractions of all elements

including hydrogen and helium are updated as:

$$f_{ij}^{(n)} = f_{ij}^{(n-1)} + \left(\Delta t^{(n-1)} \times \dot{f}_{ij}^{(n-1)}\right). \tag{2.6}$$

A characteristic timescale for f_{ij} to change is given by $f_{ij}^{(n-1)}/\dot{f}_{ij}^{(n-1)}$. For any ion ij, choosing an integration step equal to some small fraction of this timescale ensures that the steps are small enough to accurately resolve changes in f_{ij}. In principle, the timescale Δt for updating all of the ions could be chosen as some fraction (say, 10%) of the minimum timescale from all of the ions. On every step, this would update the fastest-changing ion-fraction by that fraction (10%) and all other ions would be guaranteed to change by less than that. However, ions with very low occupancy have timescales that are not of interest, so it was decided to choose Δt using the minimum timescale from any ion state with $f_{ij} > 10^{-4}$. A convergence test was conducted to select a fraction of this minimum timescale to use as Δt. A number of runs were performed using different factors, and 10% was selected as the largest factor which still accurately converged on the true solution. Thus, the timesteps used with Euler's method were:

$$\Delta t^{(n-1)} = 0.1 \times min\left(f_{ij}^{(n-1)}/\dot{f}_{ij}^{(n-1)}\right), \tag{2.7}$$

where the minimum timescale taken from all states ij with $f_{ij} > 10^{-4}$. Euler's method is a primitive technique, and some authors (e.g. Press et al., 1992) explicitly advice against its use. It was originally selected as a first attempt for the algorithm, with the expectation that it would be updated later to a higher-order method (such as the fourth-order Runge-Kutta method). However, using Euler's method for the work described in Chapter 3 provided no problems. As described in the next section, the integration method was updated when Euler's method proved inadequate for solving a later problem (detailed in Chapter 4). The work that had previously been done with Euler's method in Chapter 3 was then repeated with the new method described below.

2.2.2 CVODE

During the second application of the `Timedep` code, it became clear that there were problems with solving the rate equations with Euler's method. It was observed that ion fractions would sometimes be updated to unphysical values (i.e. less than 0.0 or greater than 1.0), or that the fractions for one element no longer summed to 1.0. This was a result of the attempt to not resolve the timescales of (uninteresting) empty states. A number of 'fixes' were tried. For example, when a fraction went negative, this

was detected by the programme and the fraction set to zero. However, boosting one negative fraction up to zero would boost the sum of the fractions higher than 1.0 by the same amount. Various schemes for maintaining the normalisation were considered and tested, including reducing the fraction in either the neighbouring ion state or the most occupied one.

Eventually it was realised that the problems experienced whilst attempting to solve the equations using Euler's method were typical of a *stiff* system of equations, characterised by the vastly different timescales for the variables being calculated. Stiff equations are often solved by implicit methods, which make use of knowledge or approximations about future timesteps. The requirement of information at advanced timesteps when using implicit methods typically makes the set of equations nonlinear and difficult to solve. Practically, these methods therefore rely on some approximation to provide a solution. Typically, Newton's method is used to linearise the matrix by iteration (Press et al., 1992).

Once the difficulties in solving the equations were identified as typical of stiff sets of equations, the decision was made to use a freely available *solver* package. `CVODE` (Hindmarsh and Serban, 2009; Cohen and Hindmarsh, 1996) was selected as a suitable package which could solve both stiff and non-stiff systems of ODEs such as those in the `Timedep` code. The modular design of `CVODE` is such that it can be included as a subroutine into another programme.

As detailed by Hindmarsh and Serban (2009), the integration schemes included in `CVODE` are variable-order, variable-step multistep methods. For stiff systems, Backward Differentiation Formulas are used:

$$\sum_{x=0}^{q} \alpha_x^{(n)} f^{(n-x)} + \Delta t \beta^{(n)} \dot{f}^{(n)} = 0, \tag{2.8}$$

with coefficients $\alpha_x^{(n)}$ and $\beta^{(n)}$ decided by the method and the recent history of step sizes; $\alpha_0 = -1$; and the order q between 1 and 5. For example, the first order method finds $f^{(n)}$ as:

$$f^{(n)} = \alpha_1^{(n)} f^{(n-1)} + \Delta t \beta^{(n)} \dot{f}^{(n)}, \tag{2.9}$$

using the value of f at the previous timestep, $(n-1)$, and an evaluation of the right-hand side of Equation 2.1 for $\dot{f}^{(n)}$ which is at the advanced timestep (making this method *implicit*). Note that this requirement of evaluating rates at a future timestep is trivial when post-processing a simulation (as in Chapter 4) since all of the rate coefficients can be evaluated for any time from the stored simulation data. The implicit evaluations

in CVODE use Newton's iteration method to solve the non-linear matrix equation. A number of iteration schemes are provided within CVODE. For the Timedep code, where the elements of the coefficients matrix are all known from the atomic rates, a Modified Newton iteration is used, keeping the iteration matrix fixed throughout the iterations. Three direct solvers are included in CVODE, suitable for a dense matrix (with mostly non-zero elements), a diagonal matrix, or a band matrix (with non-zero elements only near the diagonal). The dense matrix solver was used in Timedep since the coefficients matrix in Equation 2.4 has significant off-diagonal elements (specifically, the coefficients of the normalisation equation). It may be possible to find a linear solver module to plug into CVODE that is better suited to the form of this matrix, but the speed of using the dense solver has not been a problem.

CVODE requires two tolerance values to be set for all of the variables in the problem. The 'relative tolerance' controls the relative errors on each variable. The 'absolute tolerance' sets a minimum threshold below which the precise value of the variable is not significant (and pure relative error control would be too computationally expensive). Variables whose values are lower than the absolute tolerance are therefore assumed to be effectively zero, and are not subject to the relative tolerance for the errors on their values. For each problem being solved with CVODE (i.e. each chemical element), Timedep uses a single scalar value for the relative tolerance and a single scalar value for the absolute tolerance to apply to each variable (each ion fraction of the element). A range of values were used for the tolerances in test CVODE runs of single simulation cells, to select which values best reproduced the ion fractions for H and He found by PMRT. The selected values were 10^{-3} for the relative tolerance and 10^{-6} for the absolute tolerance.

CVODE adaptively selects its own timesteps for solving the differential equations to the required tolerances, between selected output times. These output times were chosen to give the required resolution for studying time-dependent effects in the results, and also to have intervals small enough that the rates can be approximated as being constant between two outputs (see Chapter 4). To start with, the Timedep code used 100 regularly spaced steps in t between the times of the first and last PMRT dumps.

2.3 Input Parameters

The Timedep code solves for the time-evolution of ionisation fractions at one point in the IGM, given the local physical conditions. Specifically, in order to calculate the

ionisation and recombination rates, it takes local values of the following as its input:

- the number density of each element, $n_i = m_i n_H$ (cm^{-3}), specified by an abundance (or metallicity) m_i by number relative to hydrogen, and the number density of hydrogen n_H;
- the gas temperature T (K);
- the number density of photons $n_{ph}(\nu)$ (cm^{-3}), equal to the energy density of the radiation (erg cm^{-3}) at that frequency divided by the energy per photon $h\nu$ (erg). The energy density is equal to the mean intensity $4\pi J_\nu$ (the energy passing through a region per unit area per unit time, measured in erg cm^{-2} s^{-1}) divided by the speed of the photons c (cm s^{-1}). $n_{ph}(\nu)$ is therefore specified as some parameterisation of the mean intensity, divided by $h\nu c$:

  $$n_{ph}(\nu) = \frac{4\pi J_L}{h\nu c}\left(\frac{\nu}{\nu_L}\right)^{-\alpha} = \frac{1}{h\nu c}\,\frac{L_\nu}{4\pi R^2}\,e^{-\tau_\nu} \tag{2.10}$$

  The input parameters are either the power-law spectral index α and the mean intensity per unit frequency at the Lyman edge J_L, or the source luminosity L_ν, the distance R from the source and the hydrogen and helium column densities N_{HI}, N_{HeI} and N_{HeII} for the path (of length R) from the source. The optical depth τ_ν is then calculated from the column densities using a fit from Osterbrock (1989), explained in Section 4.1.

The first application of the `Timedep` algorithm (see Chapter 3) calculates the ionisation for a single set of physical conditions with no spatial information, essentially modelling a homogenous (and infinite) volume of gas. The physical conditions are kept constant, and the ionisation is modelled as the gas evolves towards ionisation equilibrium (from some given initial ionisation structure, e.g. fully neutral). The second application of the algorithm (see Chapter 4) takes as its input the histories of the evolving density, temperature and spectral intensity in each cell of a cosmological simulation. It then calculates the ionisation throughout the simulation by generating the rates from these conditions at each time.

Note that for both of these applications, the temperature and radiation field have not been updated with contributions from the recombination processes of metals. In the first case, the physical conditions of the models are deliberately kept constant to allow straight-forward comparison to results calculated with a different code. For the simulation application, the contributions from the metals to the physical state of the

gas are neglected in favour of the original simulation's temperature model which solved accurately for the H and He. The original spectrum is also maintained for consistency with the H and He model.

2.4 Atomic data

Ten atomic processes were included in the code, and an explanation of each is given below, along with references for the sources of data used to calculate the rates. Most of these data (and some Fortran routines for implementing them) were obtained from the website *Atomic Data for Astrophysics* by Verner (2000). This is a publicly accessible collection of recent data for ionisation- and recombination-rates. Most of these data were also used in the photoionisation code `Cloudy` used in Chapter 3. The website can be found at http://www.pa.uky.edu/∼verner/atom.html

It is important to note that uncertainty in the atomic parameters for some metal transitions is a significant source of error when modelling metals in the IGM (see the detailed discussion by Savin, 2001, and references therein). Surprisingly, even for familiar elements such as magnesium, there remain significant holes in our knowledge of the reaction rate-coefficients.

Photoionisation – p_{ij}

The photoionisation rate per ion of element i in state j, removing an electron from shell nl (where n and l are the principal and orbital quantum numbers of the shell) is:

$$\Gamma_{ij}^{nl} = c \int_{E_{ij}}^{\infty} n_{ph}(E)\, \sigma_{nl}^{ij}(E)\, dE. \tag{2.11}$$

The number density of photons n_{ph} is calculated from the input parameters as specified above (with an extra factor of $1/h$ to give the number density per unit energy). $\sigma_{nl}^{ij}(E)$ is the partial photoionisation cross-section calculated using a Fortran routine by Dima Verner which uses analytic fits from Verner et al. (1996) for the outer shells of H through Si, and S, Ar, Ca, and Fe, and fits from Verner and Yakovlev (1995) otherwise. The ionisation threshold energies E_{ij} are taken from the same routine.

The integrations are performed with Gaussian quadrature, using the Gauss-Legendre and Gauss-Laguerre routines from Numerical Recipes (Press et al., 1992). In the limit of a large number of integration points these methods are exact for integrating polynomials, so offer good accuracy for any smooth function that can be well

approximated by a polynomial. The integration regions (from the ionisation threshold of the ion, E_{ij}, to infinity) are subdivided at the hydrogen and helium thresholds. Absorption by these elements can create sharp discontinuities in the ionising spectrum at these thresholds, so the quadrature is performed over the regions in between, where the spectrum is smooth so the methods work well. The number of these integration regions is dictated by the threshold energy of the ion ij relative to those of H and He. Tittley and Meiksin (2007) performed convergence tests of these quadrature methods on the same spectra used in this thesis. They found the number of evaluations of the integrand which are necessary to give a converged solution in each region. Surprisingly few of these integration points are needed, making these quadrature methods very fast and ideally suited to this problem.

The total rate (per ion per second) of photoionisations of the ion ij is found by summing over the rates of losing an electron from each shell nl:

$$p_{ij} = \sum_{nl} \Gamma_{ij}^{nl} \, W_{ij1}^{nl} \,, \tag{2.12}$$

where W_{ij1}^{nl} is the probability of only one electron being ejected, with no Auger electrons emitted (see below).

Auger-electron ionisation – q_{ijk}

The Auger effect can be found in any ionisation process that removes an inner shell electron, and it causes multiple electrons to be emitted (Semat and Albright, 1973; Smith and Stokes, 1972). One is the electron removed from an inner shell by the original ionisation process, e.g. a photoelectron ejected by the absorption of a photon. The other electrons have less energy and are called *Auger electrons*, ejected by a radiation-less transition.

Consider the case of a photoionisation which removes an electron from the $n = 1$ level. Instead of an electron passing down from the $n = 2$ state to fill the vacancy in $n = 1$, and emitting a photon with energy equal to the energy difference between levels, this energy instead is used to eject a second electron that has an ionisation energy less than that energy difference, e.g. another electron from the $n = 2$ level. This process can be imagined as one $n = 2$ electron emitting a photon as it moves to $n = 1$, and this photon ejecting a different $n = 2$ electron from the same atom. The Auger effect is known as a radiationless transition since no photon leaves the atom. For a long time after the discovery of the effect, it was believed that it was caused by this two-step

process involving the internal conversion of a photon, but it is now understood to be a single-step alternative process for removing energy.

The Auger effect is capable of emitting many electrons in one event, as a cascade effect. If a photoionisation causes a vacancy in an inner shell, and thus the ejection of an Auger electron as described, this leaves a vacancy in the next state, which has a given probability of causing another Auger electron to be ejected from the following state, and so on.

The rate of ionisation of ions from an initial state j into a state $k \geq j+2$ is given by:

$$q_{ijk} = \sum_{nl} \Gamma_{ij}^{nl} \, W_{ij(k-j)}^{nl} \, . \tag{2.13}$$

$W_{ij(k-j)}^{nl}$ is the probability of emitting $(k-j)$ electrons (including the photoelectron) during a photoionisation event which removes an electron from the nl shell of an ion ij. The values for W_{ijm}^{nl} used by `Timedep` to calculate p_{ij} and q_{ijk} were published by Kaastra and Mewe (1993). They modelled ionisation and recombination events including the Auger effect, to calculate the distribution of probabilities for losing any number of electrons. Their results show that the effect can have a significant influence on photoionisation models. For example, if a CIII atom loses an electron from the $n=1$ level by photoionisation, the probability of it also emitting an Auger electron is greater than 0.9999 . This means that for a photoionisation from the ground state, CIII is nearly always ionised to CV and not CIV. Photoionisation of FeI from its $n=1$ level can result in cascades losing up to ten electrons, with the most likely result being the ejection of seven Auger electrons along with the photoelectron.

Collisional ionisation – c_{ij}

Ions of element i can be ionised from a state j to $j+1$ by collision with a free electron, at a rate of $n_e c_{ij}$ per second. The coefficient c_{ij} is calculated using the fit (as a function of temperature) by Voronov (1997).

Autoionisation – a_{ij}

Autoionisation is the spontaneous emission of an electron during the decay of an excited state. The excited state is degenerate with the state of an electron in the continuum, i.e. the excited electron has the same energy as a free continuum electron. The ionisation appears spontaneous because this excited state can survive for a long time. Eventually the excited electron is lost to the continuum in a radiationless transition. Such an

excited state can be created by collision with a free electron, giving an excitation-autoionisation rate $n_e a_{ij}$, with fits for a_{ij} calculated by Arnaud and Rothenflug (1985).

Radiative recombination – r_{ij}

This is the capture of a free electron and the emission of a photon. The rates are calculated using fits by Verner and Ferland (1996) for H-like, He-like, Li-like and Na-like ions[2]. For all other ions, `Timedep` uses power law fits by Aldrovandi and Pequignot (1973), Shull and van Steenberg (1982) and Arnaud and Rothenflug (1985).

Dielectronic recombination – d_{ij}

There is an alternative recombination process which happens in two steps and involves another of the ion's electrons. In the first step, a free electron is captured into a highly excited state, but rather than the ion emitting a photon, the excess energy from this recombination goes to promoting a second electron into an excited state. The second stage is the decay of this double excited state. This involves the second electron falling back to its original state and radiating a photon (although the excited state could instead decay by autoionisation and the re-emission of a free electron). The main dielectronic recombination rates in `Timedep` are taken from Nussbaumer and Storey (1983, 1986, 1987). In addition to these, some other ions are given dielectronic recombination rates, in an attempt to match the atomic data used by `Cloudy`. By default, `Cloudy` gives third and forth row elements which have no known dielectronic rates, new rates equal to the mean of Nussbaumer and Storey's coefficients for C, N and O (Ferland, 1996, Vol. 1). This approximation is originally due to Ali et al. (1991) and has been reproduced in `Timedep`.

Charge transfer ionisation – c_{ij}^{H} , c_{ij}^{He}

Ions of some element i can be ionised in a collision with a positive hydrogen or helium ion. The ion ij is stripped of an electron by a singly-ionised hydrogen or helium ion which itself recombines with the electron: $H^+ + e^- \rightarrow H$ or $He^+ + e^- \rightarrow He$. Only charge transfer processes with H and He are considered, using rates from Kingdon and Ferland (1996) for H charge transfer, and from Arnaud and Rothenflug (1985) for He

[2]Isoelectronic sequences classify ions that have the same number of electrons, and are named for the neutral element in the sequence. For example, HeI, LiII, BeIII, BIV and CV are a few examples of "He-like" ions, each having two electrons.

charge transfer. The rate of ionisations per second for each process is proportional to the number density of the relevant H^+ or He^+ ion.

Charge transfer recombination – r_{ij}^{H} , r_{ij}^{He}

The other two charge transfer processes considered are the opposite of the charge transfer ionisations above. Here, any ion can recombine by capturing an electron in a collision with a neutral hydrogen or helium atom, which gets ionised: $H \rightarrow H^+ + e^-$ or $He \rightarrow He^+ + e^-$. The rates are taken from the same studies as for the charge transfer ionisation: Kingdon and Ferland (1996) for H charge transfer and Arnaud and Rothenflug (1985) for He charge transfer. The number of charge transfer recombinations per second are proportional to the number density of the neutral hydrogen or helium atoms.

2.5 Other Features

2.5.1 Initial fractions & equilibrium fractions

A number of options are available in the `Timedep` code for the initial ionisation fractions of the elements used. Hydrogen and helium can be started neutral ($f_{11} = f_{21} = 1$; $f_{12} = f_{22} = f_{23} = 0$), or when post-processing a simulation, the ion fractions can be read in from the first output dump. The metals used can also be started from neutral, or from ionisation equilibrium. The latter option involves solving the time-*in*dependent version of the system of ionisation equations for each metal (e.g. for carbon, solving Equation 2.4 with each $\dot{f}_{ij} \equiv 0$). This matrix equation is solved using the Gauss-Jordan elimination routine from Numerical Recipes (Press et al., 1992).

The equilibrium ion fractions can also be calculated using this method at every output time of `Timedep`. A second output file is then written containing these equilibrium fractions in the same format as the main output file of time-dependent fractions. This allows analysis of results relative to those found with the assumption of ionisation equilibrium.

2.5.2 Output options

The main results of the `Timedep` code are the ionisation fractions stored for each state of each element, for every cell, at the specified output intervals. These are all stored in a binary file (up to a few gigabytes in size), along with the number densities of each

element. Routines have been written in C, IDL and Matlab for reading in, analysing and displaying these data.

As described above, a second output file of identical format and size can be written containing the equilibrium ion fractions found by solving the time-independent equations. This is optional, and can be turned off with a conditional compilation flag, but is a default output.

Basic information about the `Timedep` run, such as confirmations of the settings used, notifications of progress made during the run and any non-fatal warnings, are all printed to the standard output stream (*stdout*) to be saved as a log file. Certain compilation flags cause extra information to be written to the standard output to aid debugging.

A third output file is a 'mask' which records any errors generated by `Timedep` for each cell. This is an ASCII file, containing one integer value for each cell, which stores any error flags returned by that cell.

Various other debugging options in the code cause extra output ASCII files to be written. These record values such as the spectrum used to calculate the photoionisation rates, the physical conditions (temperature, density, etc.) read in from the `PMRT` simulation data, or the HII fraction calculated at each time.

2.6 Time-dependent Tests

A number of comparisons have been performed between `Timedep` and other codes. The models presented in the next chapter (with constant temperature, density and UV spectrum) study the equilibrium times of various elements in different environments, but also provide a comparison of the distribution of the final equilibrium ion-fractions against results from `Cloudy`. Post-processing simulations that were performed with the `PMRT` code (as discussed in Chapter 4) allows a comparison of the non-equilibrium hydrogen and helium fractions. An independent test of `Timedep`'s non-equilibrium ionisation of metals requires a comparison against an earlier paper discussed in Section 1.5. Unfortunately, these published non-equilibrium models are mostly unsuitable for reproducing with `Timedep`. Many of the papers (from Kafatos, 1973 to Gnat and Sternberg, 2007) model the radiative cooling of gas as well as its time-dependent ionisation. `Timedep` cannot reproduce such models without the exact thermal history of the gas. Cen and Fang (2006) present only spectral results from their warm-hot intergalactic medium (WHIM) models (along with some other models which only test the equilibrium limit).

Gnat and Sternberg (2009) perform detailed modelling of shocks (such as those that heat the WHIM) and do present some time-dependent metal ionisation results, but the models include details such as photoionisation by shock self-radiation which cannot be reproduced by `Timedep`.

However, Yoshikawa and Sasaki (2006, hereafter Y&S) present time-dependent ionisation results for four models with fixed temperature histories, suitable for reproducing with `Timedep`. They investigate the non-equilibrium ionisation of metals in the WHIM, through both these simple models and full hydrodynamical simulations. Y&S also study the consequences of the non-equilibrium ionisation for the detectability and observables of the WHIM. Their simple models follow the ionisation of oxygen in given thermal histories of the cosmic baryons. These thermal histories represent baryonic matter diluting according to the cosmological expansion, then being shock heated as it collapses into denser structures, and then becoming quasi-virialised in these halos or filaments. The models are dictated by very few parameters, but Y&S show that they provide a reasonable representation of the histories of baryons in hydrodynamical simulations. Each of the four models includes the same UV and X-ray background spectrum calculated with the CUBA code of Haardt and Madau (2001). The CUBA code is no longer available online at the specified URL, but the spectrum used by Y&S was supplied to me by Kohji Yoshikawa.

The thermal history which runs from $z = 10$ to 0 in the models, has the baryons at 5000K until they are shocked at $z_s = 1$ to a postshock temperature T_s. Before the shock, the comoving density is constant so the physical density decreases, changing with redshift as $n_H = 2.2 \times 10^{-7}(1+z)^3\mathrm{cm}^{-3}$. At the shock, the density increases to $n_H = 2.2 \times 10^{-7}(1+\delta_s)\mathrm{cm}^{-3}$ with some postshock overdensity δ_s, and then remains constant. The postshock parameters for the four models A, B, C and D are given in Table 2.1.

Figure 2.1 shows the ion fractions of the three most highly ionised states of oxygen, as a function of time, in the four models A–D. The x-axis is the cosmological time normalised by the time to $z = 0$ (with redshift also marked along the top axis). The thick and thin lines show Y&S's non-equilibrium and equilibrium solutions, respectively. The red solid lines are f_{OVII}, the blue dotted lines are f_{OVIII} and the magenta dashed lines are f_{OIX}. The two left panels (A and C) have the same postshock density but the upper panel (A) has a higher postshock temperature. The lower right panel (D) has the same temperature history as panel A but with a higher postshock density. The two right panels (B and D) have the same postshock density but panel B has an even

Table 2.1: Postshock temperature and overdensity parameters for the four different Yoshikawa and Sasaki (2006) models. The postshock hydrogen number-density is also shown for reference. For comparison, the preshock temperature was 5.0×10^3K and density fell from and initial 2.93×10^{-4}cm^{-3} to 1.76×10^{-6}cm^{-3} before the shock.

Model	T_s (K)	$1 + \delta_s$	n_H (cm^{-3})
A	1.0×10^6	10	2.2×10^{-6}
B	4.0×10^6	$10^{1.5}$	6.96×10^{-6}
C	1.6×10^5	10	2.2×10^{-6}
D	1.0×10^6	$10^{1.5}$	6.96×10^{-6}

higher postshock temperature. Before the shock, all of the models share exactly the same conditions so the results are identical. Most of the oxygen is OVII, and all of the oxygen states are in ionisation equilibrium (as the thick and thin curves match precisely). The shock event at $z_s = 1$ is clearly seen to quickly change the ionisation fractions. The fractions also evolve both before and after the shock because of the changing density before the shock and the evolving background spectrum throughout. The non-equilibrium results in all of the models show a rise in the OVIII fractions immediately after the shock, followed by a decrease while the OIX fraction increases. The OIX fractions then start to fall again with the OVII and OVIII fractions beginning to rise while the spectrum continues to evolve through to $z = 0$.

Figure 2.2 shows the results calculated with `Timedep` for the same four Y&S models. Overall the same behaviour is seen, but the preshock OVII and OVIII ion fractions are different. Instead of reaching a peak of 0.73 around $z = 4$ and falling to 0.57 by $z = 1$ as in the Y&S results, f_{OVII} peaks at 0.65 and falls to 0.45 before the shock. f_{OVIII} is correspondingly higher in the `Timedep` results, peaking at 0.43 instead of 0.32. The other fractions match well between the two codes, with f_{OIX} reaching 0.09 by $z = 1$ in both, and 0.02 of the oxygen atoms being in the states OVI or lower. As in Y&S's results, `Timedep`'s non-equilibrium results match the equilibrium results at the start of the runs. After the shock, there is very good agreement between the results of the two codes.

Overall, `Timedep` reproduces the time-dependent results of the Y&S models well. The difference in the balance between the OVII and OVIII fractions before the shock does not mean there is a flaw in the code. Rather, it suggests a difference in the rates which makes the oxygen over-ionise between these states. The fact that `Timedep`'s

preshock non-equilibrium results match the equilibrium results suggests that it is accurately computing the ion fractions for its given set of atomic rates, which again suggests that the difference between the two codes is just a difference in these rates. Reducing the spectral intensity by a factor of 1.6 roughly reproduces the preshock results of Y&S, but also changes the postshock results. Instead, reducing only the OVII photoionisation rate (p_{OVII}) by the same factor, reproduces the preshock results and only makes a small change to the postshock results, although again moving them away from the results of Y&S. I conclude that the difference between `Timedep` and Y&S's results are due to small differences in more than one rate rather than simply one of them, but that the good match between the results overall, confirms that the `Timedep` code accurately models non-equilibrium ionisation of metals.

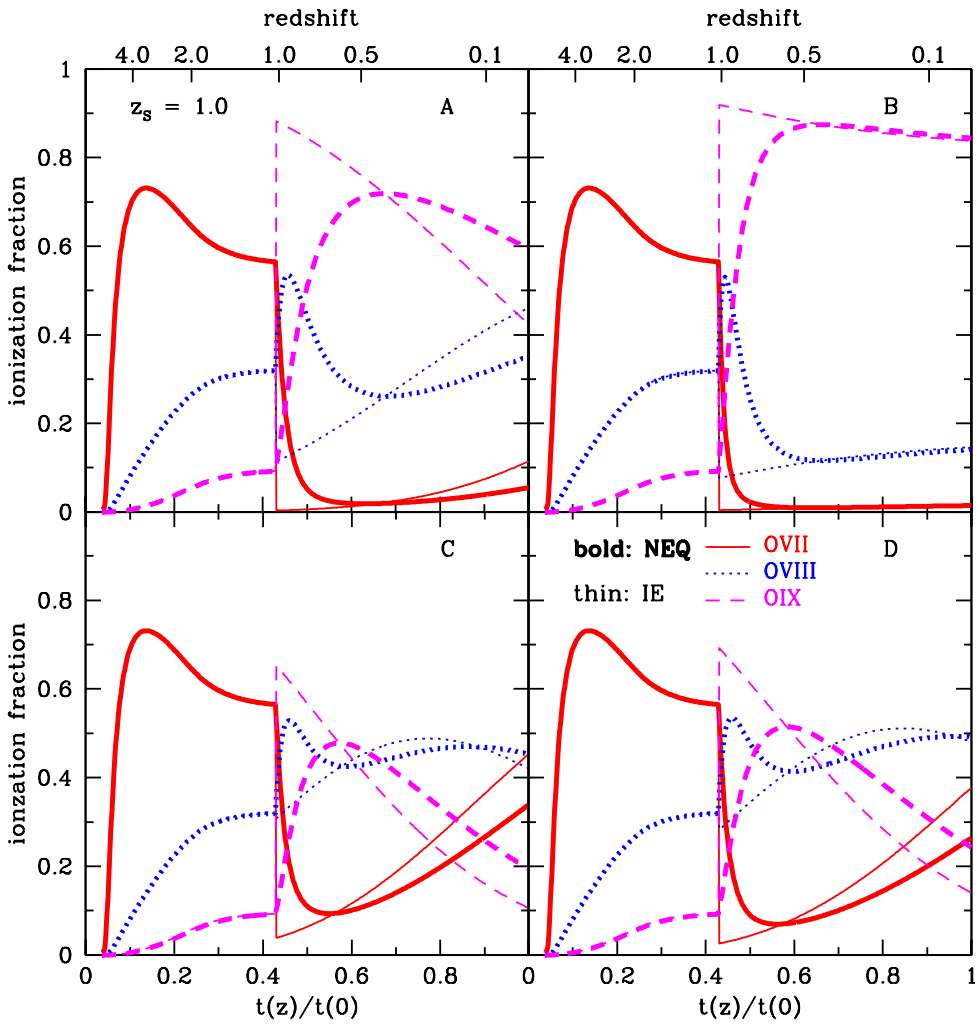

Figure 2.1: The time-evolution of the OVII, OVIII and OIX ion fractions in the four models as calculated by Yoshikawa and Sasaki (2006). The bold lines show the non-equilibrium results (whilst the thin lines show the ion fractions assuming ionisation equilibrium). This figure is 'Figure 7' reproduced from the paper of Y&S.

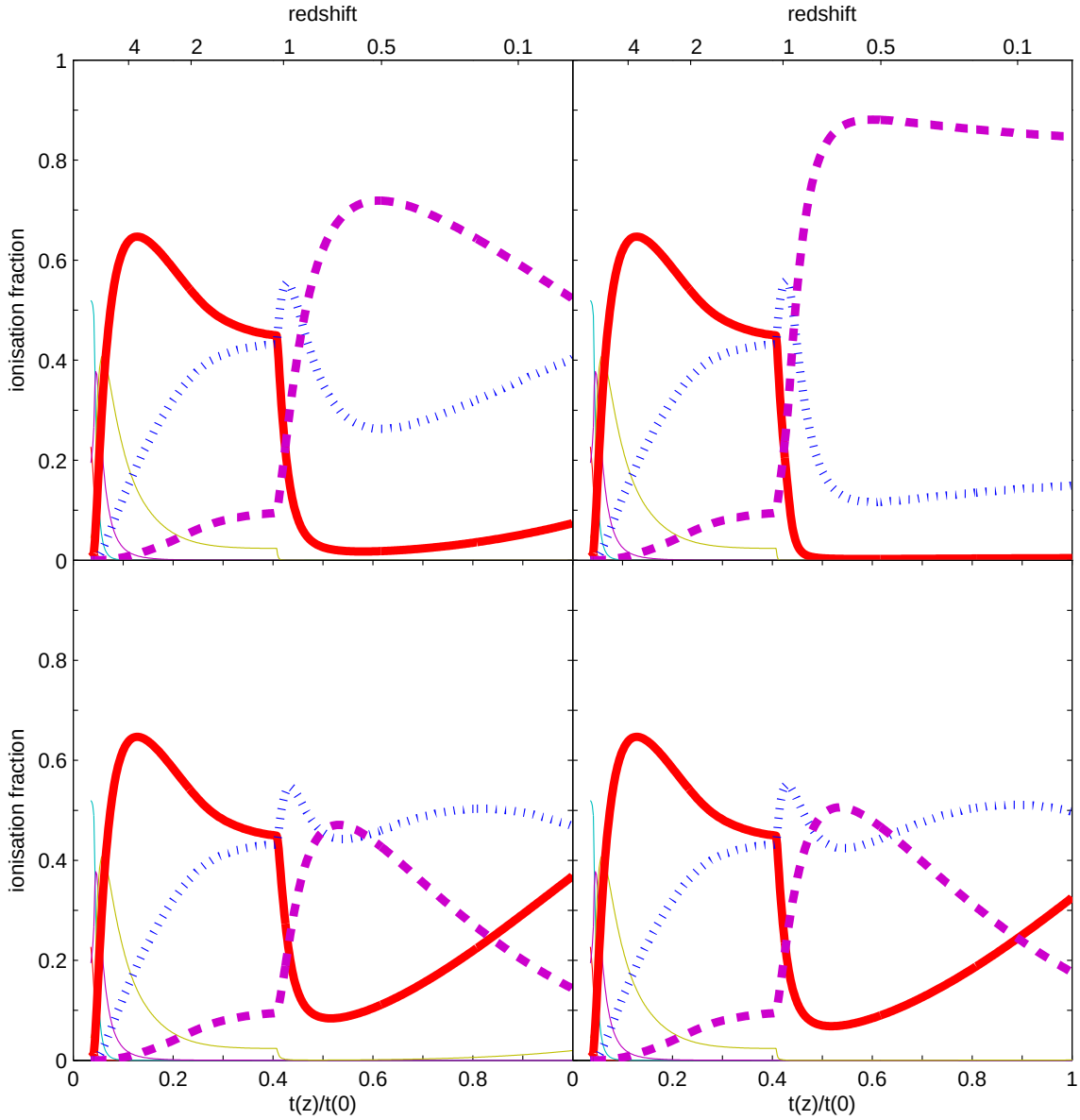

Figure 2.2: As in Figure 2.1, the OVII, OVIII and OIX ion fractions as a function of time, for the four different Y&S models but calculated with `Timedep`. The thin lines show the decaying ion fractions in the lower states, omitted by Y&S.

Chapter 3

`Timedep` Runs in a Static Medium

3.1 Introduction

In this chapter, I discuss the first use of the `Timedep` code, performing simple test models of the ionisation of metals in constant environments. Each run solved the time-dependent ionisation equations for gas that starts neutral and evolves to ionisation equilibrium, given constant density and temperature values and a constant UV spectrum. These zero-dimensional tests effectively model the ionisation in uniform volumes of gas. Fourteen different heavy elements were included along with hydrogen and helium. The runs have two uses. Firstly, by using a range of input parameters, it was possible to test how long various heavy elements take to reach ionisation equilibrium in different steady-state conditions. Secondly, these runs test of the accuracy of the `Timedep` code by comparing the equilibrium ionisation fractions with those calculated in a simulation with the same input conditions run with `Cloudy`, a widely used code for simulating astrophysical plasmas in ionisation equilibrium.

Table 3.1: Inputs for the four different static runs, used by both `Timedep` and `Cloudy`, along with the spectrum given in Equation 3.1.

U	n_H (cm^{-3})	T (K)
0.01	1.259×10^{-3}	27,660
0.03	4.169×10^{-4}	35,220
0.1	1.259×10^{-4}	46,160
0.3	4.169×10^{-5}	60,250

3.2 Static Model Inputs

The UV spectrum in these tests was a power-law with a spectral index $\alpha = 1.5$ and a mean intensity per unit frequency, J_ν:

$$J_\nu = J_L \left(\frac{\nu}{\nu_L} \right)^{-1.5} . \tag{3.1}$$

This form for the metagalactic UV background is normalised by $J_L = 3 \times 10^{-22}\,\mathrm{erg\,cm^{-2}s^{-1}str^{-1}Hz^{-1}}$. This is the mean intensity of the background radiation at the Lyman edge, the ionisation threshold frequency for neutral hydrogen $\nu_L = 3.288 \times 10^{15}\,\mathrm{Hz}$. This is a typical quasar-like spectrum, and is often used in simulations, e.g. by Rauch et al. (1997).

These tests were repeated using different values of the ionisation parameter U, the ratio of ionising photons to hydrogen atoms. The spectrum of the background radiation was the same in each run, and different gas densities (given in Table 3.1) were used to give the necessary ionisation parameters.

The input file for `Timedep` includes the number densities for each included element. For these runs, sixteen elements are included (H, He, Li, B, C, N, O, Ne, Mg, Al, Si, S, Ar, Ca, Fe and Ni) with metallicities of 0.01 solar, taking the solar abundances from `Cloudy`. These elements include all of the metals most commonly observed in the diffuse IGM. Another fourteen metals (all of the other elements up to zinc) were also tested, but did not give accurate results because of a lack of some radiative recombination rates. This resulted in these elements taking extremely long times to reach equilibrium, and producing unrealistic final distributions of ion states compared to `Cloudy` (which includes additional sources of recombination data for these elements). Therefore, the sixteen most important elements with the best understood rates are included in the tests in this chapter.

The comparison run of Cloudy 90.05 for each of the four cases was performed first (using the same inputs), and the equilibrium temperature that it calculated was used in the Timedep input file as the steady-state gas temperature (see Table 3.1).

These runs clearly model a very simplified case, to demonstrate the form of the ionisation solution rather than trying to model a real situation. Seeing no evolution of the temperature, density or external radiation field over the cosmological timescales of these runs is quite unrealistic, as is starting the runs with all elements neutral. By keeping these external parameters constant, the code also omits physical effects of feedback from the recombination processes which would contribute to the gas temperature and the UV spectrum. However, these simplifications provide a simple model which can easily be compared with Cloudy's results. If Timedep is run as part of a simulation code in the future (rather than for separate models like this, or post-processing complete simulations as in Chapter 4) then the feedback effects would be included, computation time permitting.

3.3 Cloudy and its Inputs

For comparison with the Timedep results, the same static IGM models were run with Cloudy (http://www.nublado.org/ ; Ferland et al., 1998), a publicly available code for simulating conditions in astronomical plasmas and predicting the emitted spectra. The models were repeated with two versions of the code: c90.05 and c08.00. Cloudy is a very well-established programme, having been updated continuously since its creation in 1978, and includes a thorough range of plasma physics. It is widely used in modelling the IGM, and specifically for calculating equilibrium ionisation (e.g. Songaila and Cowie, 1996; Simcoe et al., 2006; Agafonova et al., 2007). This section provides a review of how Cloudy works and how it calculates the equilibrium ionisation fractions with which I compare the Timedep results. This section is based on the documentation for Cloudy, specifically Ferland (1996, Vols. 1 and 2), where many more details of the programme's operation can be found. This section ends with a list of the specific inputs used to produce the runs.

Cloudy generates 1-dimensional models through a slab of gas under some incident spectrum of radiation, and calculates the statistical and thermal equilibrium, atomic and molecular processes, and the resulting radiation spectra. Cloudy works by splitting the modelled nebula into a series of concentric shells, each thin enough to have roughly constant physical conditions. For an optically thick HII region this is typically 100

to 200 zones, but for the optically thin models in this chapter, with nearly constant conditions, only four zones were needed. Conditions across the four zones are very similar, e.g. the equilibrium temperature calculated in each of the four zones of the $U = 0.01$ run was $27,660$K to four significant figures. Ion fraction results are given as means along the 1D model, and averages of other quantities (temperature, n_H, etc.) are given in addition to the results from each individual zone. Only the mean values are used for the comparison against the `Timedep` results.

`Cloudy` includes in its calculations all 465 ionised states and the 30 neutral states of the first 30 chemical elements, and calculates the distribution of ionisation states assuming ionisation equilibrium. For the H and He iso-sequences (ions of any element with only one or two remaining electrons) this calculation is more detailed than for ions with more than two electrons, most of which are treated considering only the ground term and the continuum for each ionisation stage (Ferland, 1996, Vol. 2, §8.1).

As well as the ionisation and recombination processes modelled by `Timedep`, which move atoms up and down the ionisation states, `Cloudy` also includes processes which remove atoms from this "ionisation ladder" altogether, such as molecular processes and advection. However, for the models considered in this chapter, these processes should make a negligible or zero contribution.

To calculate ionisation equilibrium, the rates of change $\partial n_{ij}/\partial t$ ($\mathrm{cm^{-3}s^{-1}}$) of the number density of any given ion state must be set to zero. In a simple model this only involves neighbouring states of a given element i, balancing the rates of destruction and creation of its ion j to give the ratio of number densities of the neighbouring states as $n_{j+1}/n_j = D_{j\to j+1}/C_{j+1\to j}$. For pure photoionisation and radiative recombination, $D = \Gamma_{j\to j+1}$ and $C = n_e\alpha_{j+1}$. To find the ionisation balance for an element i with J_i ionisation states, it is necessary to solve the system of $J_i - 1$ such equations plus the abundance conservation law $\sum_{j=1}^{J_i} n_{ij} = n_i$.

Other atomic processes such as Auger electron ejection, couple non-neighbouring ionisation states, so detailed balance cannot be assumed. `Cloudy` introduces these rates as corrections to the bidiagonal matrix of the above equations for neighbouring states:

$$n_j\left(D_{j\to j+1} + \sum_{k\neq j+1} D_{j\to k}\right) = n_{j+1}\left(C_{j+1\to j} + \sum_{k\neq j+1}\frac{n_k}{n_{j+1}}C_{k\to j}\right). \qquad (3.2)$$

`Cloudy` solves this ionisation balance matrix equation using standard linear algebra methods (Ferland, 2004, Vol. 2, §11.19) many times while it solves the equations of statistical and thermal equilibrium for each zone. Each time, the density ratios needed

in Equation 3.2 are taken from the previous solution, reducing the matrix to bidiagonal form again. Abundances are only calculated for ionisation states between some lower and upper limits that are constantly updated to exclude any states with negligible abundances. The other states are given an abundance of zero.

The atomic data included in the version 90.05 of `Cloudy` is discussed in Ferland (1996, Vol. 2). The main sources of the data are listed here. Photoionisation cross-sections are taken from fits by Verner et al. (1996) and Verner and Yakovlev (1995). Auger electron yields are taken from Kaastra and Mewe (1993). Collisional ionisation rates are calculated with a routine by Verner using rates mainly taken from Arnaud and Raymond (1992) and Arnaud and Rothenflug (1985). Radiative recombination rates are again calculated by a routine by Verner, including fits taken from Arnaud and Raymond (1992); Verner and Ferland (1996); Shull and van Steenberg (1982) and by Landini and Monsignori Fossi (1990, 1991). Dielectronic recombination rates are taken from Nussbaumer and Storey (1983), with rates for other elements approximated by Ali et al. (1991) which is the 'kludge' copied to `Timedep`. At high temperatures and densities, the dielectronic recombination rates are also affected by Davidson (1975)'s suppression of the Burgess (1965) process. Charge transfer rates are taken from Kingdon and Ferland (1996) and Ferland et al. (1997).

The static IGM runs were performed with version 90.05 of `Cloudy` (Ferland, 1996) by Avery Meiksin, who supplied me with the output files, and then later repeated with version 08.00. As an example, the input options used to specify the model for the U=0.3 run were:

- **hden -4.38;** the logarithm of the hydrogen number density $n_H = 4.17 \times 10^{-5}\mathrm{cm}^{-3}$,

- **table power law spectral index -1.5 low=0.009135 hi=100;** a power law continuum with a spectral index of -1.5. As a default the spectrum has breaks in the infrared and X-rays, here set at 0.009135Ryd and 100Ryd (or 0.1243eV and 1361eV). As a default, the spectrum has slopes of +2.5 at energies below the IR break, down to a limit of 1.001×10^{-8}Ryd ($\lambda \approx$10m) and a slope of -2 at energies above the X-ray break up to a limit of 100MeV $\approx 7.354 \times 10^{6}$Ryd.

- **nuF(nu) = -4.907;** intensity specified as (the logarithm of) $\nu F_\nu = 4\pi\nu J_\nu$, given at the default input frequency, the Lyman edge ν_L (1Ryd; 3.288×10^{15}Hz), with $J_L = 3 \times 10^{-22}\,\mathrm{erg\,cm^{-2}s^{-1}str^{-1}Hz^{-1}}$, giving $log_{10}(\nu F_\nu) = -4.907$.

- **metals -2;** Use the default solar metallicities, reduced by 2 dex (i.e. 0.01 solar).

The other input commands given were 'iterate' to perform a (recommended) second calculation of the model since it is optically thin; 'stop neutral column density 13' to stop the calculation when $N_{HI} \geq 10^{13}\text{cm}^{-2}$; and some 'print' options to specify the outputs. For the other runs, the density 'hden' was given as -2.9 ($1.259 \times 10^{-3}\text{cm}^{-3}$ for $U = 0.01$), -3.38 ($4.169 \times 10^{-4}\text{cm}^{-3}$ for $U = 0.03$) and -3.9 ($1.259 \times 10^{-4}\text{cm}^{-3}$ for $U = 0.1$). Recall that these inputs used with the static runs of `Cloudy` were the same as used for the static runs of `Timedep`.

3.4 Results: Timescales for reaching equilibrium

Figure 3.1 shows plots of the carbon ionisation fractions f_{ij}, found as a function of time for the $U = 0.01$ `Timedep` model with static temperature, density and UV spectrum. All of the models evolve from neutral towards equilibrium, with each subsequent ion fraction curve showing a characteristic shape as more atoms ionise into and then out of that state, until it approaches its equilibrium value. Note that all of the curves for one element at any time sum to unity. The equilibrium ion fraction results from `Cloudy` are used in the next section to compare with the equilibrium fractions found at late times in these runs, as in this plot.

A number of different methods were tested for detecting when a given species had reached equilibrium. Numerical noise may cause slight variations in a given ionisation fraction even once equilibrium has been reached, but this will lie within some interval (e.g. $\pm 1\%$) around the equilibrium solution. Before equilibrium is reached, the fraction will lie outside this range. The equilibrium time for each state ij, was taken as the last time that ion fraction entered a given range around a given measure of the equilibrium value. A number of intervals were tested for the equilibrium-detection method, including $\pm 1\%$, $\pm 5\%$ and $\pm 10\%$, and all of these offered reasonable equilibrium-times as judged by eye.

For states with $f_{ij} > 10^{-6}$, the $\pm 5\%$ interval was chosen to produce the results given below, but it should be noted that these times are not unique and a different detection method could have been used which would have given slightly different equilibrium times. This method could have centred the interval on the equilibrium value f_{eqm} calculated by `Timedep` at each timestep, but this is only available for the CVode results as the equilibrium calculation was not included in the original Euler's method version of `Timedep`. Therefore the mean of the last five f_{ij} values was taken as the equilibrium

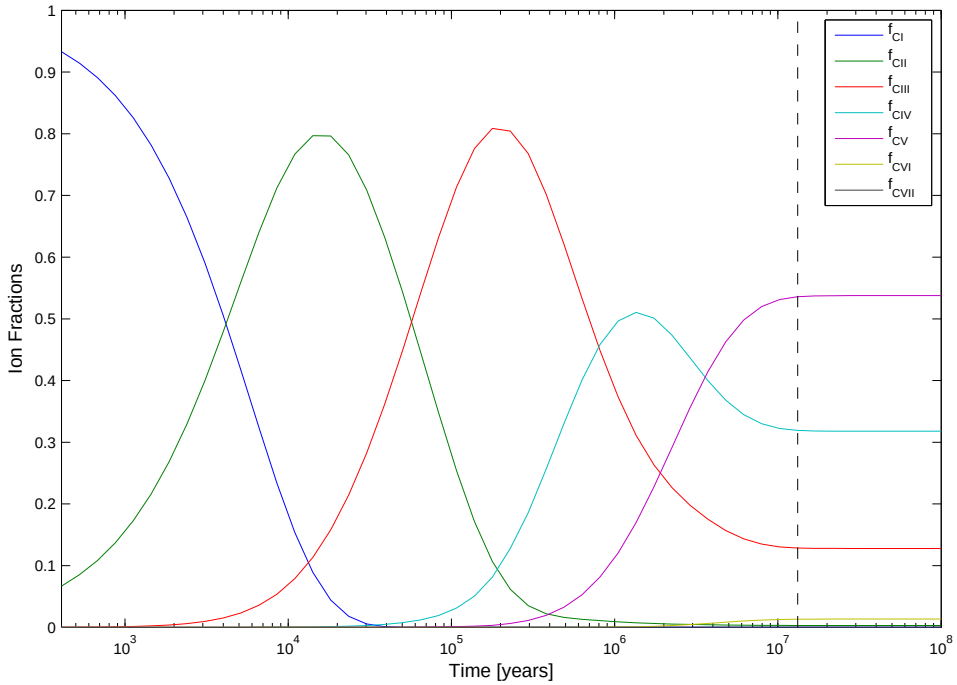

Figure 3.1: The carbon ion fractions as a function of time (logarithmic scale) for the $U = 0.01$ run with $n_H = 1.259 \times 10^{-3}\mathrm{cm}^{-3}$. Note that for any time, the seven values of f_j sum to unity. The vertical dashed line marks the equilibrium-time, detected as described in the text, at 13.2Myr for carbon.

fraction for comparison, as this can be applied to both the CVode and Euler's method results.

States with $f_{ij} < 10^{-6}$ are assumed to be effectively zero, and the equilibrium time was taken as the last time the ion fraction dropped below that threshold. For each run of the code (with $U = 0.01$, 0.03, 0.1 and 0.3) the time taken to reach ionisation equilibrium was recorded for each state of each element. This detection of the equilibrium-times for each species is carried out after the `Timedep` runs, post-processing the outputted ion fractions. The equilibrium times identified by this method for each species ij match well with values chosen 'by eye'. For each element i, its equilibrium time is taken as the equilibrium time of the last of its states ij to reach equilibrium.

The ion fraction curves for the 16 elements in the $U = 0.01$ model are shown in Figure 3.4. The time axis is again plotted as a logarithmic scale. Vertical dashed lines are marked at the equilibrium-times, detected as above. The times taken for each element to reach equilibrium are given in Table 3.2. For the $U = 0.01$ model, these range between 0.63Myr for H, to 17.0Myr for Li, Ar and Ca. After H, the next elements to reach equilibrium are Ne (in 2.89Myr), Fe and Ni (in 6.18Myr), and He and O (in 7.96Myr). The remaining elements, which took all took between 10–17Myr to reach equilibrium are N, B, C, Mg, Al, Si, S, Ar, Ca and Li.

These results calculated by `Timedep`, using CVode to solve the rate equations, can be compared with earlier results for the same model ($U = 0.01$) calculated using Euler's method. Generally, all of the elements behave in a similar way (i.e. which of them have shorter or longer equilibrium times) but they nearly all reach equilibrium sooner than in the CVode calculations. On average, the results with Euler's method reach equilibrium in 0.89 of the time taken for that element with CVode. As with CVode, the fastest element to reach equilibrium is H in 0.56Myr (compared with 0.63Myr). The longest equilibrium times found with Euler's method are for B, C, Ca (in 13.0Myr) and Li (in 14.3Myr), compared with Ar, Ca and Li (in 17.0Myr) for the CVode results.

Table 3.2: Equilibrium times (in Myr) for sixteen elements.

$U = \frac{n_\gamma(\mathrm{cm}^{-3})}{n_H(\mathrm{cm}^{-3})}$	`Timedep` method	H 1	He 2	Li 3	B 5	C 6	N 7	O 8	Ne 10	Mg 12	Al 13	Si 14	S 16	Ar 18	Ca 20	Fe 26	Ni 28
$0.01 = \frac{1.259\times10^{-5}}{1.259\times10^{-3}}$	CVode	0.63	7.96	17.0	13.2	13.2	10.3	7.96	2.89	13.2	13.2	13.2	13.2	17.0	17.0	6.18	6.18
	Euler	0.56	6.66	14.3	13.0	13.0	9.75	8.06	2.83	11.8	11.8	11.8	9.75	11.8	13.0	5.51	6.06
$0.03 = \frac{1.259\times10^{-5}}{4.169\times10^{-4}}$	CVode	0.814	10.3	36.4	46.9	36.4	36.4	36.4	13.2	36.4	36.4	36.4	36.4	28.2	36.4	17.0	17.0
	Euler	0.615	8.87	30.6	40.8	33.7	33.7	33.7	14.3	33.7	33.7	33.7	33.7	27.9	33.7	17.3	15.7
$0.1 = \frac{1.259\times10^{-5}}{1.259\times10^{-4}}$	CVode	1.74	10.2	60.4	129	129	100	100	77.8	100	100	100	100	100	77.8	77.8	60.4
	Euler	0.462	10.7	49.7	116	116	96.2	96.2	65.6	96.2	96.2	96.2	96.2	96.2	79.5	65.6	49.7
$0.3 = \frac{1.259\times10^{-5}}{4.169\times10^{-5}}$	CVode	2.24	13.2	77.8	276	356	356	276	276	276	276	276	276	276	276	214	166
	Euler	0.508	11.8	65.6	249	302	302	249	276	249	249	249	249	276	227	187	155

The other three models have higher ionisation parameters U, with lower gas densities. The UVB is the same in each run so the photoionisation rates will be the same. The rates of all collisional processes will be lower for the runs with lower density. Most importantly, the rates of radiative and dielectronic recombinations per second, $n_e(r_{ij} + d_{ij})$, are proportional to the number density of electrons and in turn to n_H. Therefore the recombination rates will decrease for each run with higher U, so the recombination timescales for each of the states ij will increase. Some of these states may reach equilibrium more quickly than the others, but in the results the occupied states of any element are seen to reach equilibrium at roughly the same time. Therefore, it is expected that the increasing recombination timescales in models with higher U, will make the equilibrium timescales of all of the metals longer.

As expected, the equilibrium times found using CVode for models with other ionisation parameters, are longer for higher U. As an example, the equilibrium times found for carbon in the different models are 13.2Myr for $U = 0.01$, 36.4Myr for $U = 0.03$, 129Myr for $U = 0.1$ and 356Myr for $U = 0.3$. These times scale as the inverse of n_H to within a few percent, and within the errors of the large timesteps. This shows how the equilibrium times for this metal are being dominated by the recombination timescales (in these runs which have the same photoionisation rates). The last elements to reach equilibrium in the different runs are Li, Ar and Ca at 17.0Myr, B at 46.9Myr, B and C at 129Myr, and C and N at 356Myr. As expected, hydrogen does not behave like the heavier elements. Hydrogen is the fastest element to reach equilibrium in all of these models, at 0.63, 0.81, 1.74 and 2.24Myr respectively. For the conditions in these models, its photoionisation rate dominates over its recombination rate, giving final equilibrium distributions that are over 99.9% ionised. As explained by Meiksin (2009), the dependence of the equilibrium timescale for hydrogen on the timescales of its individual rates is non-trivial, but for cases with fast photoionisation ($\Gamma_{HI} \gg n_H r_{HI}$) the hydrogen should approach equilibrium on the photoionisation rate timescale. It is clear that the timescales found for hydrogen in these models are not following the recombination timescales like the metals. Instead, the hydrogen equilibrium timescales do not change greatly, and in particular with Euler's method they stay relatively constant, which is consistent with the photoionisation rate dominating.

As with $U = 0.01$, the other models when calculated using Euler's method mostly show shorter equilibrium times than when using CVode. The ratios of the Euler to CVode equilibrium times, are distributed with a mean 0.889 and standard deviation 0.150, meaning that on average most elements reach equilibrium around 10% faster in

the Euler's method calculations but the scatter is large enough that a few take longer than with CVode. The longest equilibrium times are 14.3Myr for Li with $U = 0.01$, 40.8Myr for B with $U = 0.03$, 116Myr for B and C with $U = 0.1$, and 302Myr for C and N with $U = 0.3$. These longest equilibrium times found with Euler's method for the different runs are 0.84, 0.87, 0.90 and 0.85 times the longest results found with CVode.

Before comparing the equilibrium ion-fractions with those calculated by `Cloudy`, there are some conclusions that can be drawn from the equilibrium-time results.

The timescales found for IGM metals to reach equilibrium can be very long. For example, timescales of around 10^8 years are equal to or longer than estimates of the typical lifetimes of a quasar. This suggests that if any quasar that we observe, turned on in a region of the IGM with neutral (or not very ionised) metals, some of these metals are probably still out of equilibrium.

The models calculated in this chapter present an extreme case, where the metals start neutral, resulting in long equilibrium-times. However, at most epochs that we can observe the IGM, metals nearby to a new source may already be ionised to some degree by the metagalactic UVB, suggesting that the equilibrium-times found here are an upper limit for such sources turning on. The ionisation state of any metals will depend on its photoionisation thresholds, so there are situations in which metals will start neutral and the equilibrium-times may represent a more accurate estimate of the equilibrium-times. For example, before the epoch of helium reionisation, any element with all of its ionisation thresholds at higher energies than the HeII threshold will still be neutral, and even more metals will be neutral before the earlier epoch of hydrogen recombination.

The metagalactic UVB is expected to result from the contributions of a large population of quasars whose radiation percolates throughout the IGM. The spectrum used in these static models is a typical approximation to the UVB, and so the models apply to any general location (for example, at an early time) rather than specifically to locations close by to a quasar. As in the hydrogen proximity effect (e.g. Murdoch et al., 1986), nearby to an individual quasar, the UV intensity would be even stronger, suggesting higher levels of ionisation and shorter ionisation timescales, creating a metal proximity effect.

It is interesting to consider whether or not the results of these four models can predict which elements respond fastest or slowest to changes in the local UV intensity.

If all of the elements always reached equilibrium in the same order, then scaling each element's equilibrium times by those of a particular element (for example, silicon) in the relevant models, would remove the dependence of the equilibrium-times on the ionisation parameter U. Scaling the times in this way reveals the relative equilibrium times between each element, in the four different models. The large errors on the time values make the results difficult to interpret but it is quite clear that the relative timescales are not constant between the models with different U. However, a few elements do obey certain trends with respect to each other. Mg, Al and Si all have the same equilibrium-times in all four runs. H, He, Ne, Fe and Ni are all notably quicker to reach equilibrium in all of the runs, and B and C always take at least as long as Si to reach equilibrium.

In line with expectations, equilibrium times go with U, i.e. for the spectrum used in these models, the IGM metals will reach equilibrium in a time that varies inversely with the gas density. The assumption of ionisation equilibrium is more likely to be valid in the densest regions for metals, and may become increasingly inaccurate for lower density gas.

It is clear from the models in this chapter that metals in the IGM could be out of equilibrium over long timescales. It is therefore worth including time-dependent ionisation calculations in full IGM simulations to understand what the effects may be. Assuming ionisation equilibrium when modelling the IGM metals may be a valid approximation, but it will give misleading results if interpreting observations of absorption in non-equilibrium regions. Accurate interpretation of observations may well require modelling of time-dependent ionisation.

Having now shown that the timescales for IGM metals to reach equilibrium might be long for typical IGM densities, the next chapter will give an example of including the time-dependent ionisation calculations in a full simulation. As well as providing an insight into the conditions and ionisation of the IGM, the simulations will also (if the equilibrium ionisation is also calculated) give another opportunity to investigate the importance of time-dependent ionisation calculations. Another possible extension to the investigation in this chapter would be to perform a wider grid of models for a thorough range of T, n_H and J_ν. The next logical step would be to relax the constraint of having static conditions, and model the ionisation of metals with some realistic evolution of T, n_H and J_ν. This could be individual cells from a cosmological numerical simulation, and that is exactly what is done in Chapter 4. Before this however, the next section provides an evaluation of the accuracy of the `Timedep` code.

3.5 Results: Equilibrium distribution of ion fractions

The ion fraction curves plotted in the last section show how the metals evolve towards ionisation equilibrium in the time-dependent results. At late times, they reach ionisation equilibrium and the distribution of ionisation states (i.e. the fraction of all atoms which are singly ionised, doubly ionised, etc.) becomes basically constant. These values are compared in this section with the results of three other methods: the equilibrium values found by the time-dependent calculation using Euler's method, the fractions calculated by `Timedep` with Gauss-Jordan elimination assuming ionisation equilibrium, and the ion fractions calculated by `Cloudy` assuming ionisation equilibrium. The first is interesting to see whether both integration methods converge on the same solution, and the second also checks whether the solution found by these methods integrating through time is in fact the correct solution to the problem. Finally, comparing with `Cloudy` provides a check of the `Timedep` code against a well established programme, and shows whether both codes are actually solving the same problem. Note that the Gauss-Jordan elimination routine is used to calculate the ion fractions assuming ionisation-equilibrium *at each timestep*. Naively these results would be expected to be constant for a static-medium run, but these results evolve over time while the hydrogen and helium fractions change because the number density of electrons alters the atomic rates. The results used to compare with the main `Timedep` methods are the constant values once n_e has reached equilibrium. `Cloudy` by contrast, solves the equilibrium equations and calculates only the time-independent results including the equilibrium n_e.

For each of the four static medium runs, there are sixteen elements included, each of which has five calculated equilibrium distributions of its ion fractions. For example, Figure 3.2 shows the distribution of ion fractions for silicon in the $U = 0.01$ run, as calculated by the five methods. For the `Timedep` runs using CVode and Euler's method, the equilibrium ion fractions are taken as an average of the last five timesteps, long after all the elements have reached equilibrium. These two distributions are both plotted but are virtually indistinguishable, so both integration methods appear to work well for these experiments. The results of `Timedep`'s equilibrium calculation (using Gauss-Jordan elimination) are also indistinguishable in Figure 3.2, from the two time-dependent `Timedep` distributions. This shows that the two integration methods used by `Timedep` (Euler's method and CVode) are both converging at late times on the true solution of this problem (as dictated by the algorithm, the atomic rates used

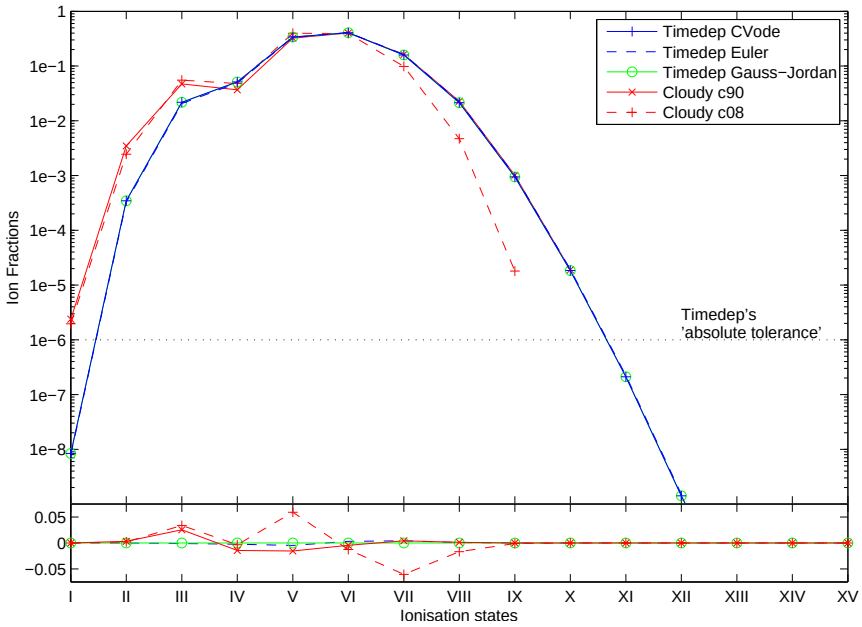

Figure 3.2: The equilibrium silicon ionisation fractions (logarithmic scale) found for the $U = 0.01$ model by four methods: at the end of the time-dependent calculation by `Timedep` (using CVode); at the end of the calculation using an old version of `Timedep` using Euler's method; the solution found by `Timedep` assuming ionisation equilibrium (using Gauss-Jordan elimination); and the equilibrium ion fractions calculated by two versions of `Cloudy`. The lower panel shows the differences of the latter four methods from CVode.

and the input data for this run). This is true for all of the runs. For example, the largest difference between any of the equilibrium ion fractions calculated by `Timedep` with either CVode or Gauss-Jordan elimination, for $U = 0.03$ is less than 10^{-9}, and for $U = 0.3$, less than 10^{-12}. The time-dependent solutions are therefore converging extremely well onto the equilibrium solutions, so the Gauss-Jordan results will not be plotted on the remaining figures to make it easier to see the other distributions.

The `Timedep` results are also a good match to the results from `Cloudy` 90.05, with excellent agreement for f_{SiV} and above. `Cloudy` 90.05 gives the peak abundances as $f_{SiV} = 0.324$, $f_{SiVI} = 0.402$ and $f_{SiVII} = 0.163$. `Timedep` finds $f_{SiV} = 0.334$, $f_{SiVI} = 0.409$ and $f_{SiVII} = 0.163$. Note that around 90% of the silicon atoms lie in one of these three states. My code does appear to under-predict the fractions in the lowest ion states compared with `Cloudy`. The source of this discrepancy remains unclear, but could be due to small differences in the atomic rates data used. For the ions SiVII and higher, `Cloudy` 08.00 calculates lower fractions than all of the other methods. This is likely due to changes in the atomic rates data used by `Cloudy` between the versions of the code, as discussed further below. The rates data included in `Timedep` are closer to the data in `Cloudy` 90.05 and these results match well.

Figure 3.5 shows the equilibrium ion fraction distributions for the sixteen elements in the $U = 0.01$ run. Some of the elements, such as H, He, N, O, Ne, S, Ar, Ca, Fe and Ni, have good agreement between CVode, Euler's method and `Cloudy` 90. The only exception is that the Euler's method fractions are low for the lower ion states of S, Ar, Ca, Fe and Ni. Other elements have good agreement between the two `Timedep` methods, but under-predict the fractions of atoms in lower ion states compared with `Cloudy` 90's results (Li, B, C, Mg, Al and Si). `Cloudy` 08 matches the `Timedep` results as well as `Cloudy` 90 does for the modelled elements up to Ne, but shows differences in the results for the heavier eight elements. In particular, it underestimates the fractions of ions in higher-ionised states, and by Fe and Ni it is clear that `Cloudy` 08 is producing a less ionised distribution of atoms.

Figure 3.3 shows the equilibrium Si ion fractions for the four different runs (with just the CVode results connected by solid lines and the `Cloudy` 90 results connected with dashed lines). This illustrates how the increasing ionisation parameter ionises the IGM to higher states. The maximum occupied state of silicon increases with U: SiVI for $U = 0.01$, SiVII for $U = 0.03$, SiVIII for $U = 0.1$ and SiIX for $U = 0.3$.

The results of the other three static models are similar (in terms of the equilibrium distribution found by different methods for a given element) compared with the

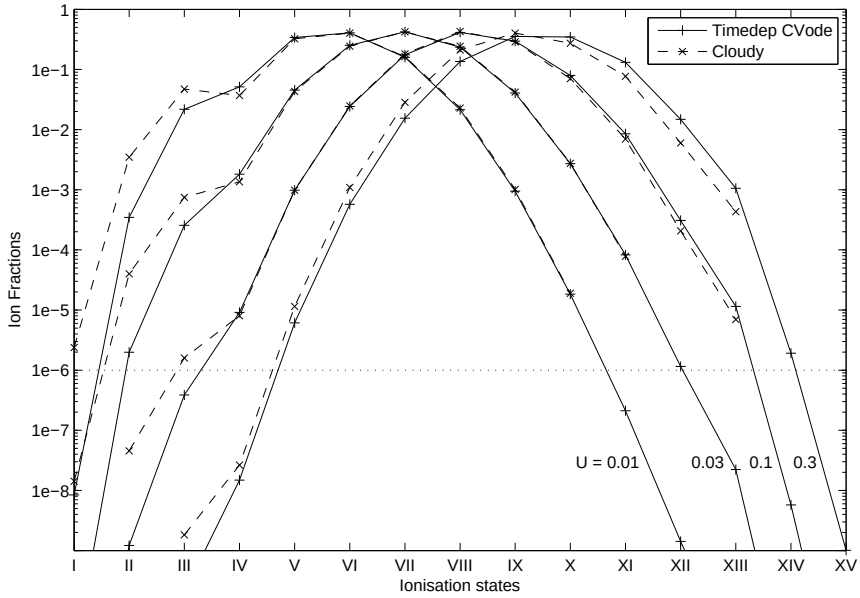

Figure 3.3: The equilibrium silicon ionisation fractions (logarithmic scale) found in four runs with different ionisation parameters U. Results from two methods are shown: from `Timedep` (using CVode) connected by solid lines, and from `Cloudy` 90, connected by dashed lines.

$U = 0.01$ model discussed above. For any model, each element can be classified by either showing good agreement between methods for all occupied states; showing good agreement between methods except for `Timedep` under-predicting the occupancy of low ion states relative to `Cloudy`;

H, He and Ni show good agreement between the four plotted methods for all four models. Li, B and C (and for the high U models, N and O) generally agree very well between the methods, but `Timedep` underpredicts the ion fractions in low states of these elements relative to `Cloudy`. The CVode results also agree very well with the `Cloudy` 90 results for Fe and Ni, for Si except at $U = 0.01$, and for S, Ar and Ca except at high U. Otherwise, for these elements along with Mg and Al, `Timedep` underpredicts the fractions relative to `Cloudy` 90, for low ion states. S, Ar and Ca (as well as Fe and Ni in the $U = 0.01$ model) show that Euler's method underpredicts the ion fractions in the lowest states relative to CVode.

The heavier eight elements modelled, from Mg to Ni, all show significant differences between the `Cloudy` 08 results and the other methods, especially for the models with higher U. The atomic rates used by `Cloudy` 08 produce a lower level of ionisation in these elements. Performing these models with two different versions of `Cloudy` has demonstrated how our best values of ionisation and recombination rates have varied

over the years, and how this affects the results. This shows how important it is that both the authors and the users of codes which model astrophysical metal ionisation carefully select, understand and publish which rates are used in their codes. With so many individual rates needed for an accurate code, and the published rates data being so patchy, there have often been some ambiguities in the published accounts of which rates a code is using (e.g. exactly when `Cloudy` is interpolating for missing data). Of the elements modelled here, H, He, C, N, O and Ne are the only ones for which `Cloudy`'s rates have not significantly changed the results between versions c90.05 and c08.00.

When comparing the results of `Timedep` and `Cloudy`, there are a few differences to consider. Firstly, although the atomic data (the ionisation and recombination rates coefficients) used by the codes are mostly the same, there are some differences. When developing `Timedep`, the atomic data selected was not copied exactly from any version of `Cloudy`. Instead, a more simple set of data was selected, mostly from the website of Verner (2000), with at least one source of data for each process to give a realistic set of rates. There is a lot of freedom to make different choices of rates, and studying the differences between them and the selection of the best data would itself be a very large research project. The atomic data used in `Timedep` is a realistic set of rates, and is close to that used by `Cloudy` 90. The differences between them are however, likely to be responsible for the different equilibrium ionisation results.

The other major difference between the two codes is that `Timedep` does not include feedback on the temperature and UV spectrum. The lack of heating or cooling will not be significant for the ionisation results since the temperatures of these tests are taken from the `Cloudy` 90 equilibrium solutions. The lack of re-emitted radiation in `Timedep` from the recombination processes is clearly not the cause of the differences between the results of the two methods, since the `Timedep` results are over- not under-ionised relative to `Cloudy`'s.

3.6 Summary and Conclusions

A set of four IGM models has been presented with constant UVB, four different constant densities (giving different ionisation parameters), and constant temperatures. The time-dependent ionisation of the heavy elements in these models has been calculated with two different versions of the `Timedep` code (using Euler's method and the stiff-equation solver CVode respectively). The popular code `Cloudy` (versions 90.05 and 08.00), and a Gauss-Jordan elimination routine were also used to calculate the ion fractions of the

elements in these models assuming ionisation equilibrium.

The times at which the different elements reached equilibrium were recorded for the different methods. These equilibrium times are very long, ranging (for the CVode results) from 6.3×10^5 years to 3.56×10^8 years, The timescales are longer for the runs with higher ionisation parameters U. The two different integration methods (Euler's method and CVode) find slightly different equilibrium-times, but the timestep resolution in these tests was very low so the errors on these times are relatively large. I believe the results are close enough to suggest that both methods might be converging on the same equilibrium-times.

Five sets of equilibrium distributions are calculated for each model, and all three calculated by `Timedep` match very well. The very good match between the two time-dependent calculations and the equilibrium calculation suggests that the time-dependent methods are converging well with time on the correct equilibrium solution to the problem. The results from `Cloudy` 90 were matched by `Timedep` very well except for the lowest states of a few elements. Differences in the results of the two codes are likely due to differences in their atomic rates data. The good match overall suggests that other differences between the two codes (such as the lack of diffuse emission by radiative recombination in `Timedep`) do not to affect the results greatly.

`Timedep` seems to model the ionisation well. The evolution of ion fractions found by both Euler's method and CVode match well. The good match of these equilibrium distributions to `Cloudy`'s, suggests that `Timedep` is functioning well. It is worth noting that the sixteen elements which are modelled here, include all of the elements most often seen in quasar absorption spectra, e.g. Verner and Yakovlev (1990) list twelve such elements (H, He, C, N, O, Ne, Mg, Al, Si, S, Ca and Fe) all of which are in the sixteen included in these `Timedep` models.

Performing the models with two versions of `Cloudy` had demonstrated the effect of our changing knowledge of ionisation and recombination rates data over time. For the heavier metals modelled here, `Cloudy` 08 calculates significantly lower levels of ionisation compared to version 90. However, for most of the important elements the differences are much smaller, and the ion fractions calculated by `Timedep` match both versions of `Cloudy`.

The equilibrium-timescale results have large errors, each being selected as one of the timesteps of the static-medium runs, but they provide a good illustration of the times taken by each element. Both of the time-integration methods used in `Timedep` (Euler's method and CVode) give similar timescales within these errors. There is

no way to say which method performs better without an independent check, but both appear to function well for these models. However, it is known that Euler's method will fail for other models. CVode was first included in the `Timedep` code when developing the code for processing the simulations in the next chapter, where Euler's method cannot give accurate results and CVode functions well.

The models that were run in this chapter could be viewed as an independent test of `Cloudy`, although not much can be said because of the small sample of just four models, the omission of some elements and the use of rates which correspond to an old version of `Cloudy`. It is a very large programme, and although it is rigourously tested by its developers, the supporting documentation is not up-to-date, and it is possible that changes made to the programme since its earlier versions are not understood by everyone who uses `Cloudy` in their research. It is so well established that it is widely used, but rarely independently tested. It is therefore worth asking whether the results obtained by users of `Cloudy` should always be trusted, although the work here barely starts to address this question. Indeed, §1 of Ferland (2008, Vol. 3) discusses the limits, assumptions and reliability of `Cloudy`, but the first part of this documentation (Ferland, 2008, Vol. 1) also knowingly comments that "nobody ever reads this document". The first question is whether the results are correct for the given assumptions. The four tests done in this chapter show a good match between these two independent codes for commonly observed elements. Although `Cloudy` appears to produce realistic equilibrium ion fractions for these elements, the results may not be perfect and are clearly seen to change as new rates are measured more accurately. The second question in assessing `Cloudy`, and the general conclusion of this chapter, is whether it is justified to assume ionisation equilibrium when modelling the IGM.

The very long timescales seen for the metals in these models to reach equilibrium, suggest that common metals in the IGM may sometimes be out of equilibrium. This suggests that it is worth calculating the time-dependent ionisation of metals in future work to model the IGM. For example, the grids of static IGM models often used to interpret observations (e.g. by Simcoe et al., 2006, using `Cloudy`) typically assume ionisation equilibrium. The IGM that is observed however, may well be out of equilibrium, especially near a bright, new source such as a quasar. Including time-dependent ionisation in the models used to interpret spectra would make the interpretation more difficult, as the time-dependent effects will likely be degenerate with other factors such as the UV intensity, but ignoring the possible non-equilibrium effects may lead to a mis-

interpretation of the observations. The other area of modelling which should include time-dependent ionisation effects, is in large dynamic IGM simulations, which could lead to a much better understanding of the implications of non-equilibrium metal ionisation in the IGM.

The models that were run in this chapter are very simple, and could easily be made more realistic (although therefore less general). The first extension would be to perform simple non-static models, for example using the UVB intensity and the mean density and temperature of the IGM as a function of redshift, calculated analytically. An alternative approach which would be more detailed but again, less general, would be to take the density and temperature history of a single structure in the IGM, and this is effectively the models performed for each cell of the simulation in the next chapter.

In this chapter, the long ionisation equilibrium-times possible in the IGM have been demonstrated. To investigate the effects of time-dependent ionisation calculations further, more realistic modelling will be presented next. A simulation of a quasar turning on is performed in Chapter 4, to study the effects of this on the ionisation of metals in the IGM, and as an example of using the `Timedep` code in a full cosmological simulation.

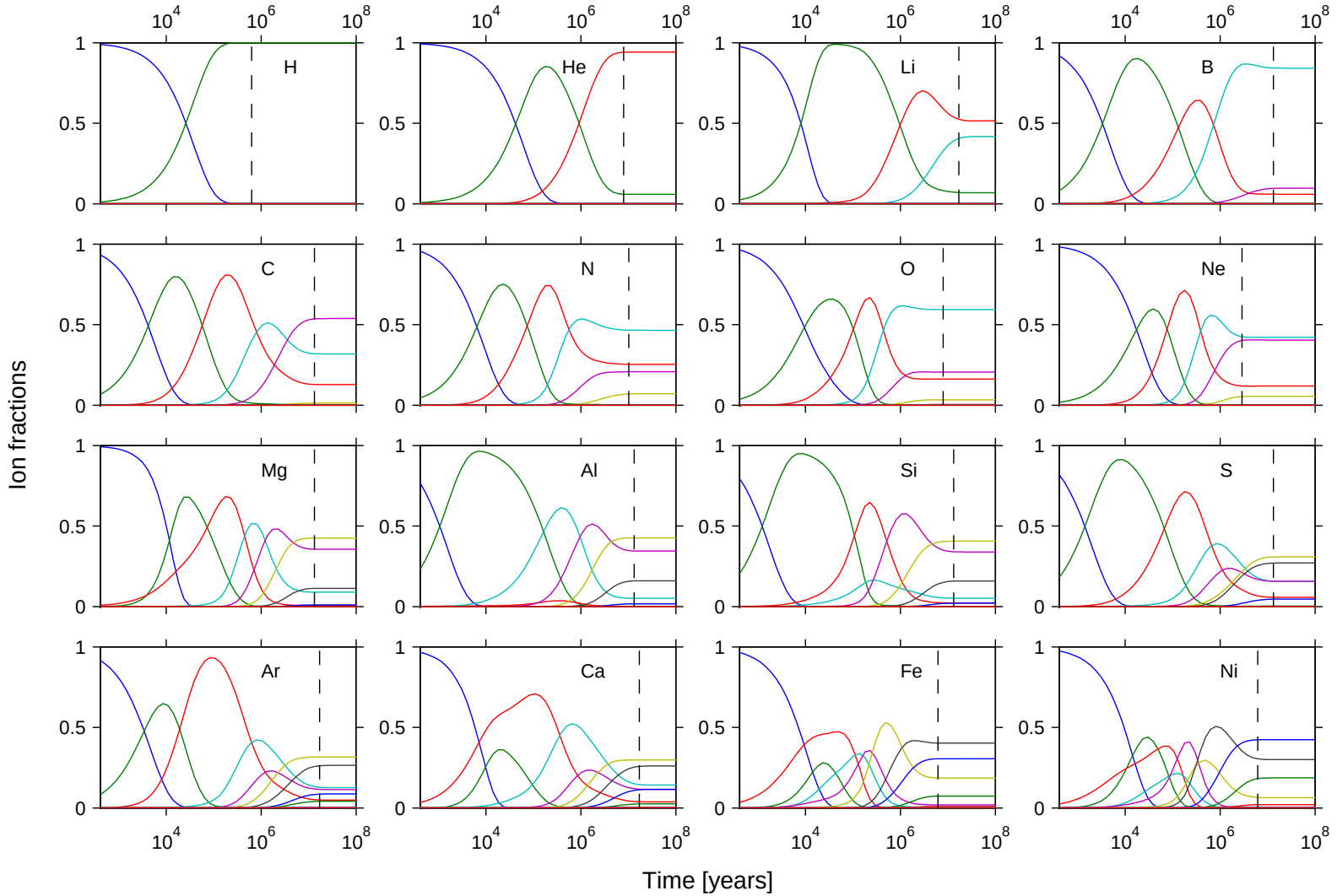

Figure 3.4: The ionisation fractions as a function of time (shown on a logarithmic scale from 400 years to 100 megayears) for each element in the $U = 0.01$ model. The vertical dashed lines represent the measured times at which each element reaches equilibrium.

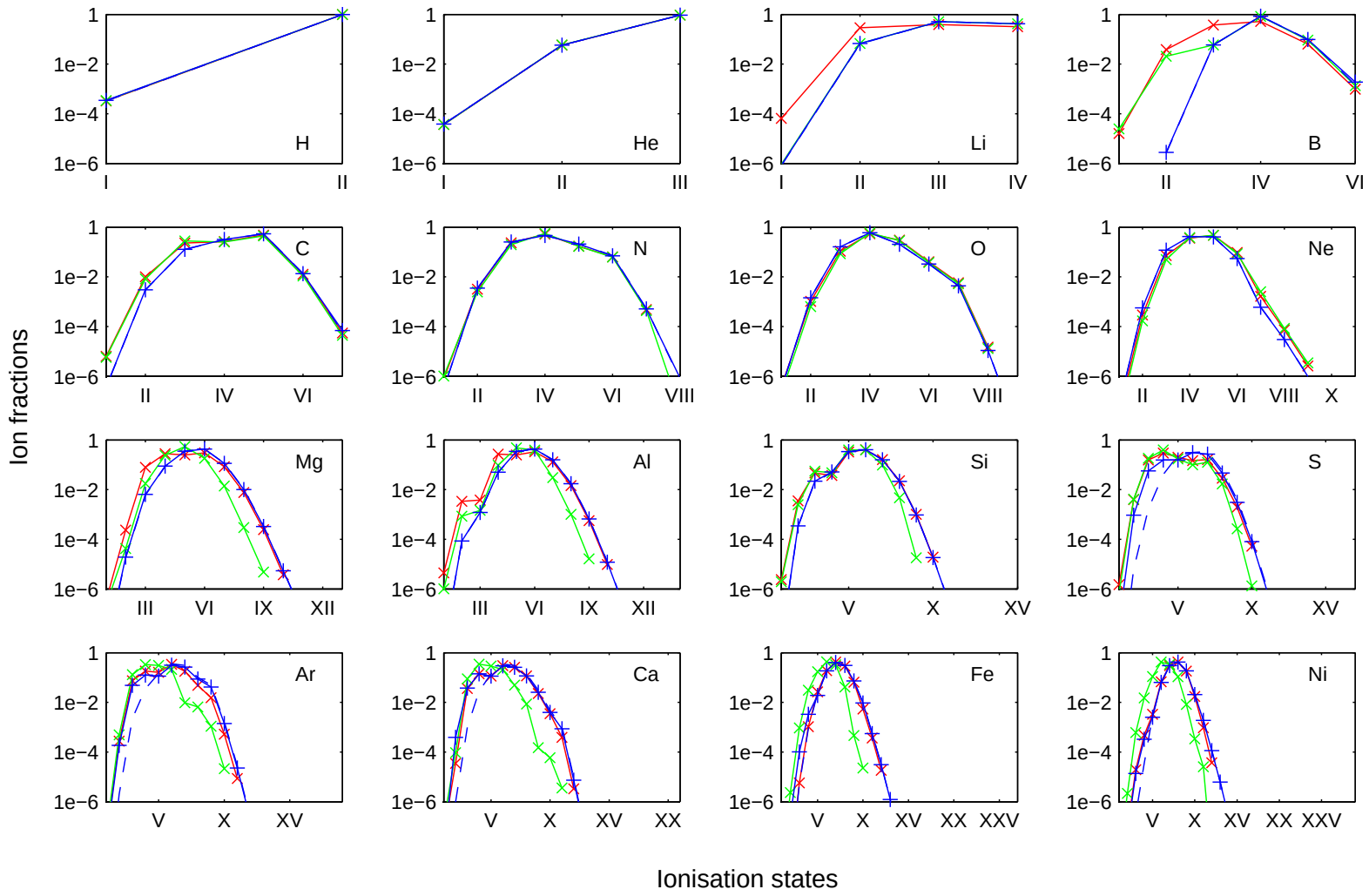

Figure 3.5: The equilibrium ionisation fractions (logarithmic scale) found for $U = 0.01$ by `Timedep` with CVode (blue plus signs and solid lines) and Euler's method (blue dashed lines), compared with the equilibrium fractions from `Cloudy` 90.05 (red crosses and solid lines) and `Cloudy` 08.00 (green crosses and solid lines).

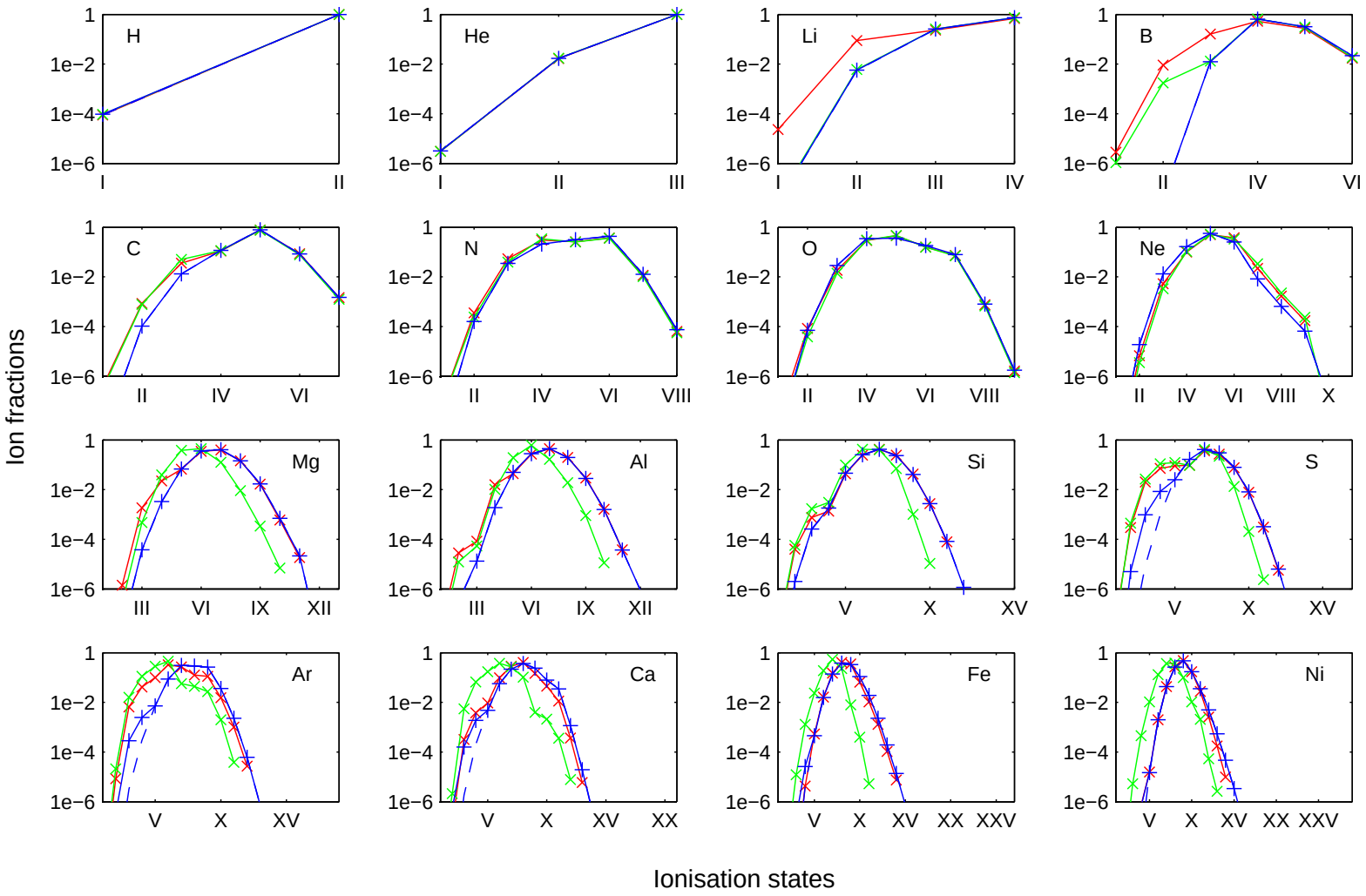

Figure 3.6: The equilibrium ionisation fractions (logarithmic scale) found for $U = 0.03$ by `Timedep` with CVode (blue plus signs and solid lines) and Euler's method (blue dashed lines), compared with the equilibrium fractions from `Cloudy` 90.05 (red crosses and solid lines) and `Cloudy` 08.00 (green crosses and solid lines).

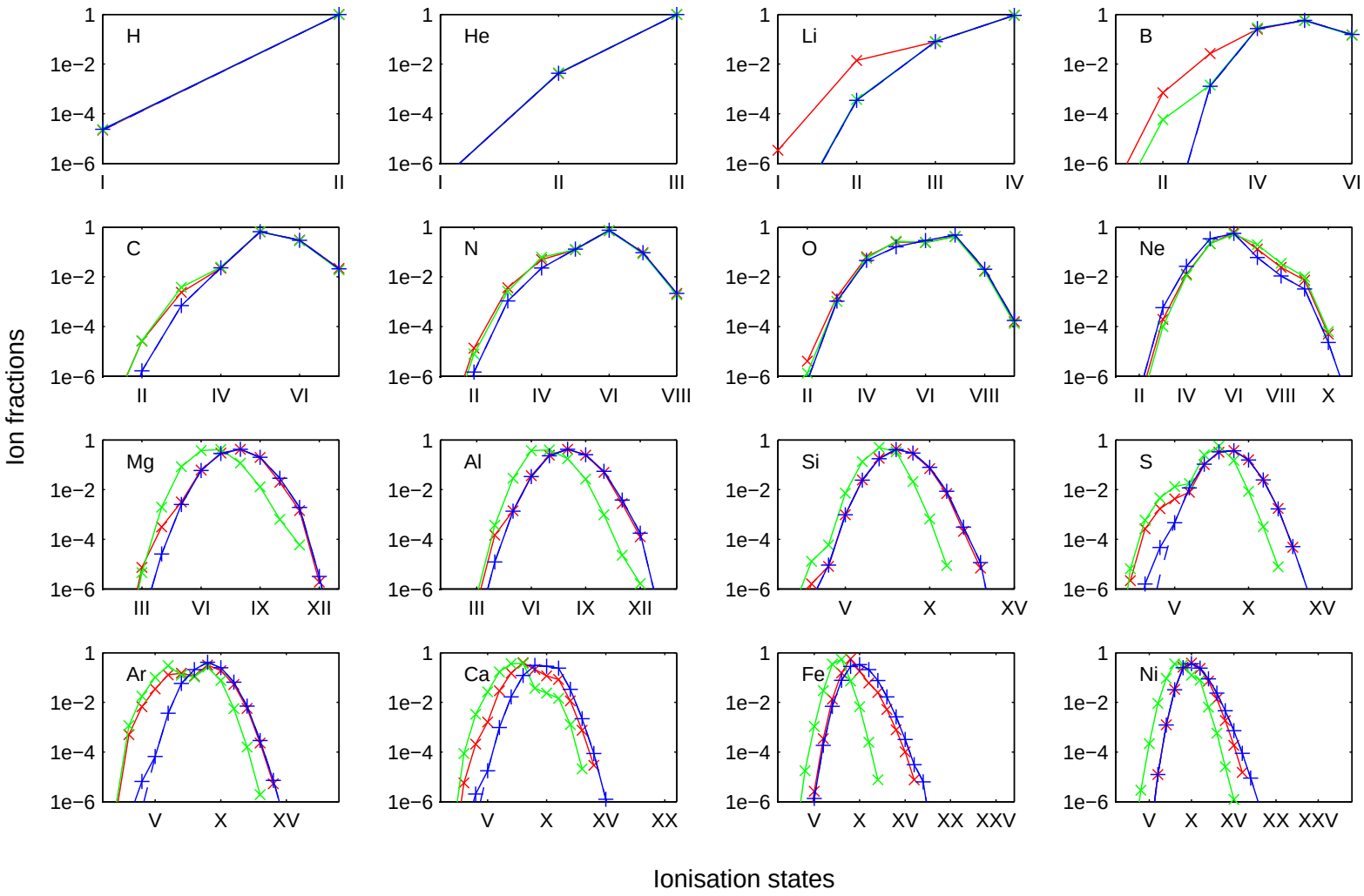

Figure 3.7: The equilibrium ionisation fractions (logarithmic scale) found for $U = 0.1$ by `Timedep` with CVode (blue plus signs and solid lines) and Euler's method (blue dashed lines), compared with the equilibrium fractions from `Cloudy` 90.05 (red crosses and solid lines) and `Cloudy` 08.00 (green crosses and solid lines).

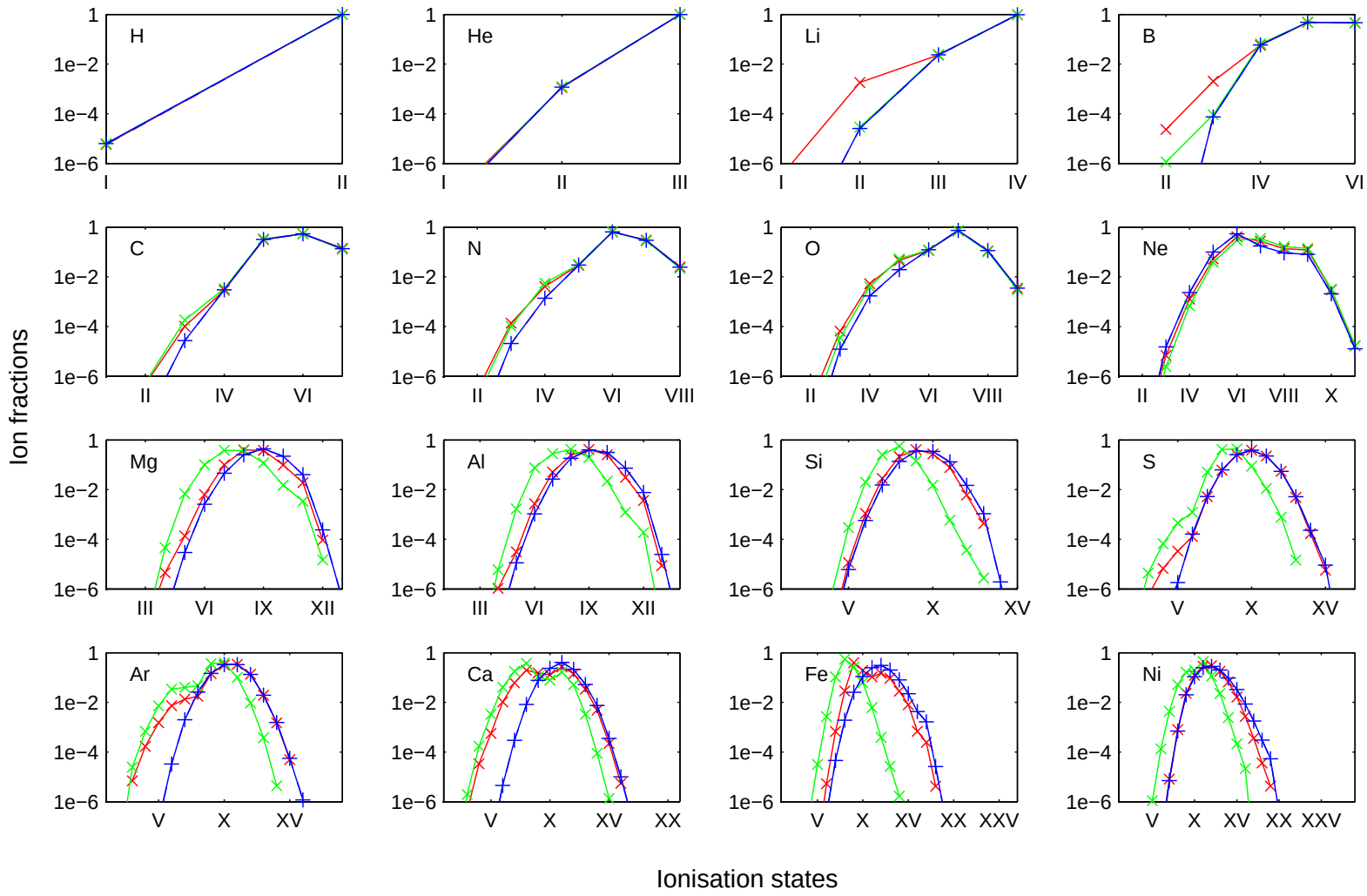

Figure 3.8: The equilibrium ionisation fractions (logarithmic scale) found for $U = 0.3$ by `Timedep` with CVode (blue plus signs and solid lines) and Euler's method (blue dashed lines), compared with the equilibrium fractions from `Cloudy` 90.05 (red crosses and solid lines) and `Cloudy` 08.00 (green crosses and solid lines).

Chapter 4

Non-Equilibrium Ionisation Around a Young Quasar

The main application of the `Timedep` code to date, has been an example of its use with a full cosmological IGM simulation. This was used to investigate the ionisation of heavy elements in the IGM around a young quasar turning on in a region of the IGM after the Epoch of Reionisation with hydrogen and helium-1 preionised. The original simulation was performed by Eric Tittley and Avery Meiksin with their `PMRT` code on a polar-grid with the source at the centre (Meiksin et al., 2010). In this chapter I present an overview of how the simulations were set up, followed by details of the `Timedep` runs. The results of the calculations are then presented and discussed.

4.1 `PMRT` quasar simulations

`PMRT` (Tittley and Meiksin, 2007; Meiksin et al., 2010) consists of a particle-mesh (PM) N-body simulation code combined with a radiative transfer (RT) code (see Section 1.4). It was designed for cosmological simulations of an ionisation front passing through a volume of the intergalactic medium, from early in the Universe until after the Epoch of Reionisation. The RT algorithm is used to accurately calculate the ionisation and temperature structure of gas in the N-body simulations. Full details of the `PMRT` code,

which can be found in the references above, will not be reproduced here as I was not involved in its development, but the relevant details are given in this section.

The core N-body simulations were performed with the PM code of Meiksin et al. (1999, Appendix B therein). This models a single matter density field (dark matter plus baryons) as being collisionless, interacting only through gravity.

The RT algorithm, originally due to Abel et al. (1999), uses a probabilistic method to calculate the number of photoionisations in each cell along rays emanating from point sources of radiation. The original algorithm which solved for the ionisation of hydrogen only, was extended to also solve for helium by Bolton et al. (2004). This method was then coupled with the PM code to solve for the propagation of radiation along lines of sight from a single source, in either a plane-wave geometry with the source outside one side of a cubic volume (Tittley and Meiksin, 2007), or in a polar geometry with the source at the centre (Meiksin et al., 2010). The N-body particles do not carry temperature or ionisation-fraction information as they move between cells, which allows the radiative transfer along each line of sight to be treated completely independently. A large number of these lines of sight (256) are generated through the PM simulation volume. These lines of sight are all selected in a single plane through the simulation volume, simply to aid visualisation of the ionisation front. This effectively creates a two-dimensional simulation with full RT, within the original three-dimensional N-body simulation volume. However, as the lines of sight are independent, the results are equivalent to having drawn the LOS randomly from the whole volume.

The `PMRT` simulations which were processed with the `Timedep` code, model a quasar turning on in a pre-ionised region of the IGM. The central source begins as a starburst galaxy spectrum at $z = 8$. A quasar then turns on at some z_{QSO}, and the spectrum evolves smoothly until at $z = z_{QSO} - 1$ it is a hard, pure power-law spectrum $L_\nu = L_L(\nu/\nu_L)^{-\alpha}$ with $\alpha = 0.5$. The `PMRT` simulation used for this study is taken from a range of 24 simulations, with three different quasar turn-on redshifts ($z_{QSO} = 3.5$, 4.5 and 5.5), four different normalisations of the source luminosity ($L_L = 10^{28}, 10^{29}, 10^{30}$ and $10^{31}\mathrm{erg\,s^{-1}Hz^{-1}}$), and with the source centred on either a density maximum or minimum within the PM volume. The comoving volume of the PM simulation was $(25h^{-1}\mathrm{Mpc})^3$, with 256^3 particles and a grid size of 512^3 mesh-points. The boundary conditions were periodic, which allowed the polar RT to be re-centred relative to the original cube. The distances of the RT cells on each LOS from the source, are calculated with a nominal comoving distance of $1h^{-1}$Mpc between the source and the first cells. This represents the scale on which the source is expected to have completely ionised the

H and He early on, so it is assumed to be fully ionised, allowing significant improvements in the computation time. A ΛCDM model was assumed, with $h = 0.71$, $\Omega_b h^2 = 0.022$, $\Omega_m = 0.268$ and $\Omega_\Lambda = 0.732$ (Spergel et al., 2003).

4.2 `Timedep` quasar runs

The `Timedep` code has been used to model the ionisation of metals in some of these quasar simulations, one of which is presented in detail in the rest of this chapter. `Timedep` is perhaps better suited to being used with Lagrangian simulations, where the ion fraction information would move with packets of gas. However, the gas in the `PMRT` simulations mostly stays within the comoving cells so these simulations offer an acceptable example application of the `Timedep` code. By assuming that the gas does not move between cells, the `Timedep` code can be used to model the ionisation evolution of each cell of the simulation *independently*.

For this application, the `Timedep` code was used to *post-process* the output from completed simulations. At a number of output redshifts, `PMRT` saves the temperature, hydrogen number-density, proper distance from the source, and integrated column-densities from the source for H and He, for each cell. `Timedep` linearly interpolates these values to any time during the simulation, to allow the necessary rates to be calculated.

The local UV intensity is not stored by `PMRT`, so this has to be recalculated by `Timedep`, as described below. This is not as accurate as the full radiative-transfer calculation solved by `PMRT`, but offers a reasonable approximation as confirmed by reproducing the H and He ion fractions. The same source spectrum is taken, by using the matching model spectrum from `PMRT`: either a quasar power-law, a starburst galaxy, a blackbody, a mini-quasar, or a hybrid model that starts with a starburst spectrum and then evolves to a power-law spectrum after a quasar turns on. The luminosity function from `PMRT` was already selected at compile-time, and linked into the `Timedep` executable file. The spectrum incident on any cell of the simulation is then calculated by `Timedep` by attenuating the source luminosity for geometry and absorption, as follows. The `PMRT` runs are either performed with the plane-wave approximation and the radiation moving from one side to the other of the simulation volume, or on a polar grid with the radiation emitted from a source at the centre of the volume. For the latter case, the source spectrum is geometrically attenuated by $1/R^2$, using the cell's distance from the source, R, stored by `PMRT`.

Table 4.1: Fit parameters for calculating the photoionisation cross-sections with Equation 4.2. Fits taken from Osterbrock (1989).

	σ_T (cm^2)	ν_T (Hz)	β	s
HI	6.30×10^{-18}	3.282×10^{15}	1.34	2.99
HeI	7.83×10^{-18}	5.933×10^{15}	1.66	2.05
HeII	1.58×10^{-18}	1.313×10^{16}	1.34	2.99

In both geometries the luminosity of the source is attenuated by $e^{-\tau_\nu}$ where the optical depth τ_ν is assumed to have a negligible contribution from metal absorption, so is calculated for H and He absorption only. The column densities N_{HI}, N_{HeI} and N_{HeII} stored by `PMRT` are used along with fits to the photoionisation cross sections $\sigma_\nu(ij)$ taken from Osterbrock (1989) to calculate the optical depth as follows:

$$\tau_\nu = N_{HI}\,\sigma_\nu(HI) + N_{HeI}\,\sigma_\nu(HeI) + N_{HeII}\,\sigma_\nu(HeII), \tag{4.1}$$

$$\sigma_\nu = \sigma_T \left[\beta \left(\frac{\nu}{\nu_T}\right)^{-s} + (1-\beta)\left(\frac{\nu}{\nu_T}\right)^{-s-1}\right] \quad \text{for} \quad \nu > \nu_T. \tag{4.2}$$

The fit parameters σ_T, ν_T, β and s are given in Table 4.1.

The ion fractions of IGM metals are not sensitive to the number density of the metals themselves (see Section 2.1). Therefore, the time-dependent fraction results of this chapter do not require the metal abundances to be specified (in contrast to the spectra results in Chapter 5, generated from the same simulations). The metal abundances are assumed to be small, thus giving negligible contributions to the cooling and to the electron density. This also maintains the original spectrum and temperature model of the original simulations for consistency (including accurate modelling of cooling and heating from H and He). Different distributions of metals could be applied to the ion fraction results since each cell is independent, allowing a physical interpretation. One very simple model is to assume a homogenous metal abundance relative to hydrogen so that the metal density simply traces the gas density around the quasar. This is a good model if the metals polluting the IGM have been well mixed in the quasar's environment, for example by a galactic wind preceding the quasar phase. Although it is not necessary to apply any distribution of metals when considering the ion fractions, this simple model allows an easy interpretation of the results, where any ion fractions multiplied by the hydrogen number density would trace out the ion number density. Maps of the ion fractions therefore can be understood by noting the overdensities and voids.

The initial ionisation fractions for hydrogen and helium were taken from the first PMRT output file, while the metals were started from ionisation equilibrium under the temperature, density and UV background at the time of the first PMRT output (Section 2.5.1).

From the available PMRT simulations, the one analysed first and presented here has $z_{QSO} = 3.5$, $L_L = 10^{31}\mathrm{erg\,s^{-1}Hz^{-1}}$, and is centred on a density maximum. PMRT simulations calculate the ionisation of hydrogen and helium, including full radiative transfer, so Timedep does not need to model the ionisation of these two elements itself. However, hydrogen and helium were included in the Timedep application described below, with the intention of reproducing PMRT's ion fraction results as an independent test of the new code. Although not expected to be identical, the results from the two codes for hydrogen and helium are expected to be close enough to show whether Timedep is working correctly. This test proved useful, as it showed up two bugs and a solution to one of those. This is discussed in detail below with the other results.

Note that initial tests of Timedep on PMRT simulation data revealed the problems of solving stiff equations with Euler's method, so the version of Timedep used throughout the rest of the thesis uses CVode to solve the ionisation equations. The system of equations for each metal is independent of the others when the number density of electrons is already known from Equation 2.5, either taking the hydrogen and helium densities from PMRT, or calculating them with Timedep at the start of each timestep by assuming that the charge-transfer processes make a negligible contribution to the H and He rates because of the low metal abundances. Therefore, the ionisation of different metals can be solved separately on different processors. As an example, a run of Timedep for the full volume and duration of the simulation with just two metals, carbon and silicon, plus hydrogen and helium, took roughly 2 hours 40 minutes on a 2.66GHz Xeon Linux computer. This produced two binary output files, each 1.7GB in size, a mask file recording errors for each cell, formatted as an ASCII file of integers, 129KB in size, and another text file recording the log messages printed by the code to *stdout*. Routines were written with C, Matlab and IDL for reading in these output files for analysis and displaying.

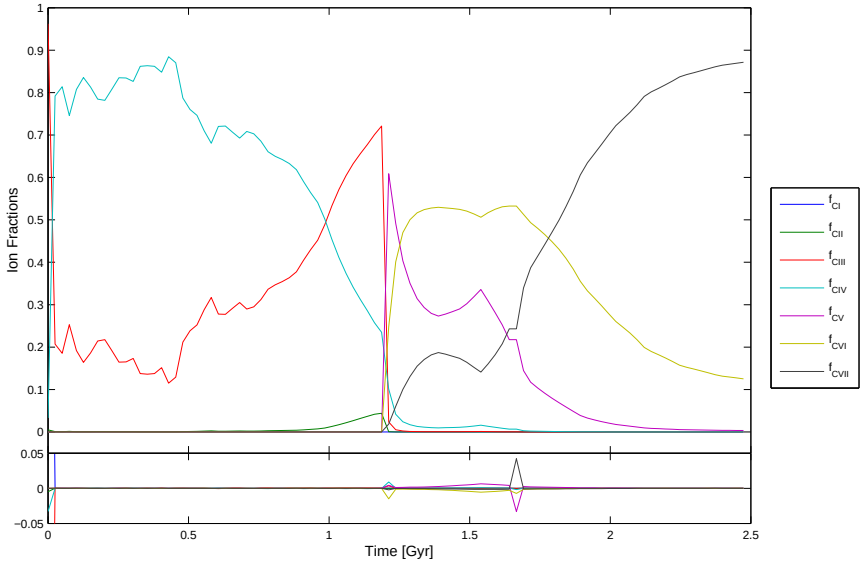

Figure 4.1: The carbon ion fractions f_{Cj} as a function of time for cell (49,9), and the deviations from equilibrium $f_{eqm,\,Cj} - f_{Cj}$. The carbon starts in ionisation equilibrium at time $t \approx 2.07 \times 10^{16}$s, and then evolves as the physical conditions in the simulation change. The quasar turning on at $t \approx 5.83 \times 10^{16}$s can clearly be seen to rapidly ionise the carbon to higher ion states.

4.3 Results & Discussion

Time-dependent ionisation

The main output of the `Timedep` runs is the set of ionisation fractions for each element in each cell at each time. Even for carbon alone, it is not possible to plot all of the resulting data here (7 ions $\times$ 256^2 cells $\times$ 100 timesteps) so the discussion will focus on certain ions. After presenting and discussing the time-dependent ionisation results, they are then compared with the equilibrium results, along with a discussion of the ionisation of silicon, followed by a discussion of the global properties. A summary of the main results is given below in Section 4.5.

Figure 4.1 shows the evolution of the carbon ionisation fractions with time in one cell, (49,9) i.e. the ninth cell in the forty-ninth LOS, at a comoving distance of $879h^{-1}$kpc from the source. The figure shows the initial equilibrium ion fractions, with the majority of carbon atoms as CIII and some small fraction of CIV and CII (unlike Figure 3.1 with the neutral initial conditions of the static medium runs). The most obvious feature in Figure 4.1 is the turn-on of the quasar at $t \approx 5.8 \times 10^{16}$s, which quickly ionises most of the carbon in this cell to CV, and further through CVI to

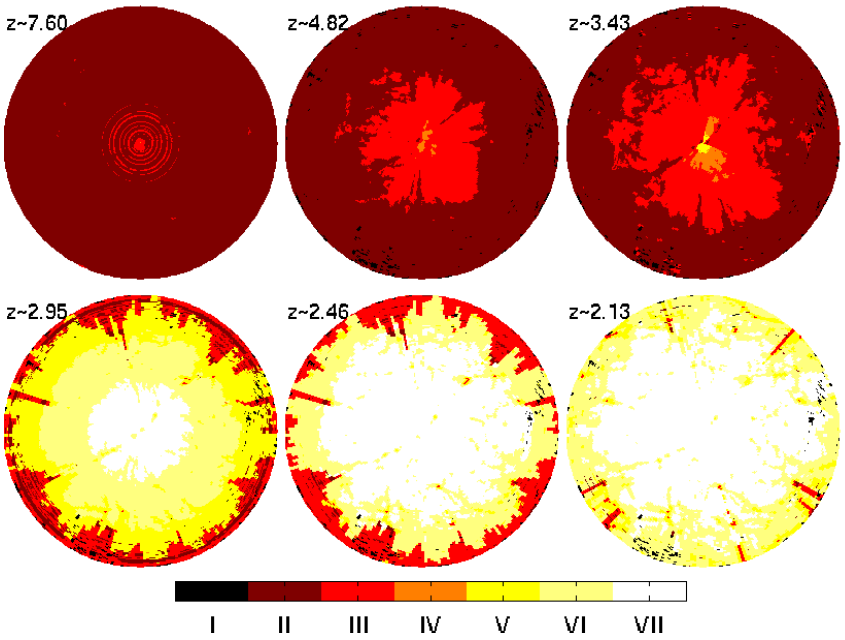

Figure 4.2: Maps showing the most highly occupied ion state of carbon in each cell, from neutral CI to fully ionised CVII. Maps are shown for six timesteps through the simulation with (in rows, from top left) $z \approx 7.6$, 4.82, 3.43, 2.95, 2.46 and 2.13 . Narrow circular features such as the bands of CII and CIII near the centre at $z \approx 7.6$ and near the outside at $z \approx 2.95$, are anomalous and not physical. The starburst source can be seen to ionise most of the carbon to CII and CIII, before the hard quasar spectrum turns on from $z = 3.5$ and ionises most of the nearby carbon to CVII.

CVII while the quasar increases in luminosity. Although the distribution of ionisation states appears to be approaching some steady level at late times, the carbon is already in ionisation equilibrium so this evolution must be caused by the evolving physical conditions in the cell.

The ionisation of the carbon across all cells of the simulation is shown in Figure 4.2, with six 'snapshots' at $z \approx 7.6$, 4.82, 3.43, 2.95, 2.46 and 2.13 . Each map shows the dominant ion state in each cell at that time. Some of the features seen in this figure which are discussed in detail below, show what appear to be the effects of two different bugs remaining in the results, one causing the concentric patterns within CIII regions and the other creating an HI region around the periphery of the volume at certain times (seen mapped out in CIII in the fourth and fifth maps). However, the rest of the carbon states, the rest of the time during the simulation, and the rest of the volume in the fourth and fifth maps, all seem to be well behaved, producing reliable data on the

ionisation of metals in this simulation.

When the simulation begins at $z = 8.0$ the carbon is started in ionisation equilibrium by balancing the equilibrium rate equations. At the second timestep (which is not plotted) there is a central CIII region less than 182kpc (three cells) in radius (with 95.8% CIII, 3.8% CIV and 0.4% CII in the first cell). The fraction of CII increases with radius until $f_{CII} = 1.0$ at 248kpc (ninth cell) and the rest of the volume is singly ionised.

By the third timestep, plotted in the first map in Figure 4.2, the `Timedep` results show a tiny CIV region just 175kpc (two cells) wide. Beyond this are concentric circular features that are anomalous, alternating between a maximum ion state of CIII and CII. Since the radiative transfer is solved along radial lines of sight, and the ionisation is solved independently in each cell, there seems to be no reason for coherent structures perpendicular to the lines of sight, in some cases just one cell thick. No such structures are seen in the input data (`PMRT`'s temperatures or densities) or in the results for silicon. These features are assumed to be non-physical, and caused either by a 'bug' in the `Timedep` code or plotting routines, or by a numerical effect. Examining the ion fractions in the CII and CIII features shows that the CII bands have a mix of $f_{CII} = 1.0$ (precisely) but also a tiny fraction of neighbouring states, whilst the CIII bands show a plausible balance between CIII and other states. I therefore propose that the CIII results are true and represent a large central CIII region which has anomalous CII bands superposed on it, rather than the other way around. Beyond the outer CIII feature, the rest of the carbon is singly ionised CII. However, any such interpretation should be viewed with caution given the obvious presence of a bug. The main motivation for understanding these circular features is as a diagnostic of this outstanding bug rather than for scientific interpretation.

By $z \approx 5.0$ the starburst galaxy's spectrum has ionised an even larger CIII region and created a larger CIV region. This is asymmetric because of dense regions near the source increasing the optical depth and so reducing the radiation intensity along those lines of sight. This shadowing is more pronounced by the time the quasar turns on at $z = 3.5$. The CIV regions have grown and a CV region appears, but both only where the radiation can escape past the two overdensities. The two regions will at later times form the local density maximum on which the `PMRT` simulation was centred. They are dense enough to be self-shielding and so form small CII regions.

By $z \approx 3.0$ the quasar has further ionised the whole volume, creating an inner CVII region with concentric regions of lower ionisation further out. Around the edge

of the volume is a CIII region which corresponds with the HI region found by the `Timedep` code. Unfortunately no such HI region is found by `PMRT`. The hydrogen and helium calculations in `Timedep` are not expected to produce identical results to `PMRT` since they do not include full radiative transfer. However, this hydrogen front is a significant difference between the results of the two codes, and may indicate a bug in the `Timedep` code instead of just the effect of using different methods. Since `PMRT` finds no hydrogen front within the simulation volume at this time, I assume that this front found by `Timedep` is incorrect. The cause of this result has not yet been identified. As noted above, the hydrogen and helium calculations were only included as a test, and the helium results accurately reproduce those from `PMRT`.

The equilibrium carbon ionisation-fractions calculated by `Timedep` (and discussed in detail below), do not show the CIII region on the periphery at $z \sim 3$–2, which again suggests a bug in the code. The hydrogen fraction used in the code (which was calculated by `Timedep`) should only affect the ionisation of metals through the number density of electrons, as the HI column density used in calculating the local radiation intensity is taken from `PMRT`. Silicon also shows the same region with cells dominated by SiIV or SiII, whereas behind the hydrogen front is mostly SiVIII. The CIII region also shows unphysical circular fully-CII features, similar to the CII features in the CIII region at $z \approx 7.6$.

Calculating the ionisation of hydrogen in `Timedep` has indicated the possible presence of the bug causing the anomalous HI region around the periphery of the volume, but as yet this question has not been solved. New `Timedep` runs will use the H and He fractions calculated by `PMRT` when calculating the ionisation of metals, so the effect of the H will not be an issue and I expect not to see this CIII region. However, the rest of the volume of the present simulation remains unaffected by the HI region around the outer edge, so can be treated independently for the rest of the analysis given here.

The bottom row of maps in Figure 4.2 show small, less-ionised features within the CVII region. Some if not all of these trace out the overdensities in the simulation volume. These overdense regions are particularly well shown in Figure 4.3 which maps f_{CVI}, the fraction of carbon atoms in each cell that are ionised to CVI, at different times once the quasar has turned on. Please note that these maps are *not* at the same timesteps as the previous figure, but instead show six timesteps after the quasar has turned on (as there is no CVI at earlier times). Before discussing the overdense structures clearly visible in the maps, it is first necessary to understand the general ionisation trends with radius and time. The source spectrum evolves from

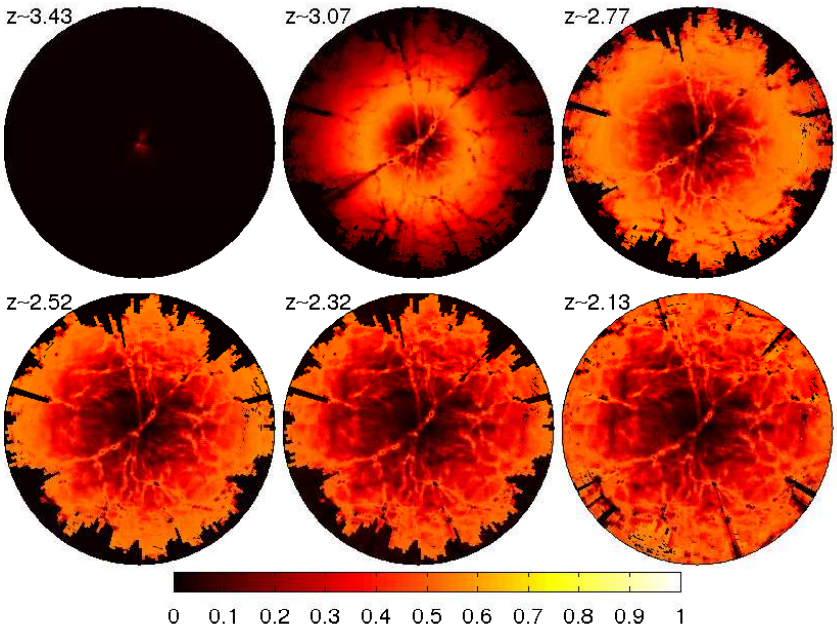

Figure 4.3: f_{CVI} maps following the turn-on of the quasar, at redshifts (in rows, from top left) $z \approx$ 3.43, 3.07, 2.77, 2.52, 2.32 and 2.13 . The colour in each cell represents the ion fraction from 0.0 to 1.0 on the scale shown. N.B. The timesteps are not the same as in Figure 4.2 since there is no CVI before the QSO turns on.

a starburst galaxy to a quasar spectrum between the times of the first and fourth maps shown ($z \approx$ 3.43–2.52). The bright ring in the second map at roughly half the radius of the volume, shows a high fraction of CVI and corresponds to the CVI region seen in the fourth map in Figure 4.2 a few timesteps later. The darker central region of the second f_{CVI} map is the CVII region, and outside the strongest CVI region the fraction of CVI drops, through the concentric regions dominated by lower ion states. Note the sharp drop to $f_{CVI} = 0$ in the anomalous HI and CIII region discussed above, seen here as the black regions at the outside of all maps except the first. The bright CVI region spreads to the outer regions of the volume by the later maps, while the dark inner CVII region expands to fill most of the volume. Against this broad ionisation structure surrounding the quasar, the dense filaments and nodes are traced out as being less ionised. In Figure 4.3, these overdensities appear dark in outer regions, showing lower ion states dominate over CVI, and appear light in the central CVII region showing CVI dominating. The densest nodes within the filaments appear dark again, showing they are not even ionised as far as CVI.

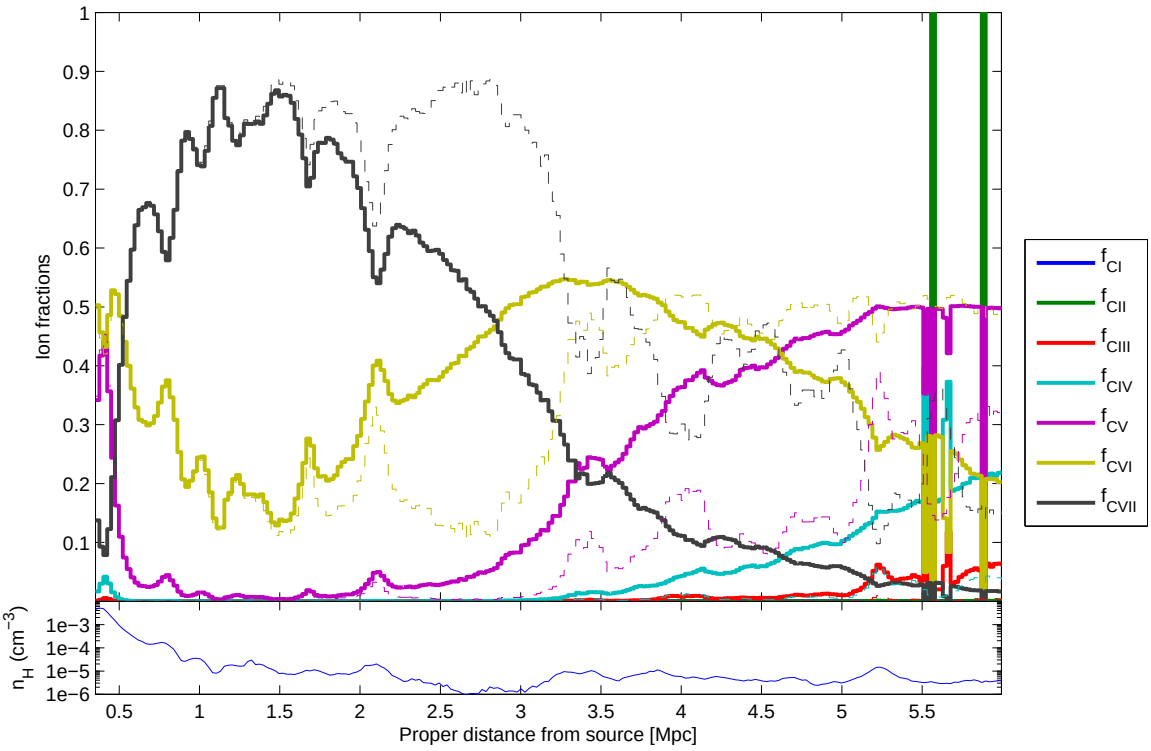

Figure 4.4: The carbon ion fractions f_{Cj} as a function of radial distance from the source, along the 22nd LOS, at $z \sim 2.95$. The solid lines show the `Timedep` carbon fractions and the dashed lines show the equilibrium fractions for comparison. Also shown is the number density of hydrogen, n_H (on a log scale). Note the ionisation structure tracing the overdensities and voids; the increasing deviation from equilibrium further from the source; and the two anomalous CII cells.

Figure 4.4 plots the carbon ion fractions along one radial LOS, at the same time as the fourth map in Figure 4.2 ($t = 7.09 \times 10^{16}$s, $z \approx 2.95$). The solid curves show how the ion fractions vary from cell to cell away from the source. As expected, the general trend is for lower ionisation with increasing distance from the source, caused by the lower intensity of ionising photons. It is clear that there are not sharp boundaries between the CVII, CVI and CV regions, but rather the ion fractions vary smoothly with distance away from the source. The carbon in these regions is mostly in the maximum occupied state shown in Figure 4.2, but there is a significant fraction of carbon atoms in other states as well. Figure 4.4 shows all cells in LOS 21 before the outer CIII region discussed above. For clarity, this region has not been plotted here as it is believed to be anomalous and also shows different behaviour to the rest of the volume (e.g. the CIII region starts abruptly at the 234th cell of this LOS, 6.02Mpc from the source, and virtually all of the carbon is CIII with very little in other states). The CIII region also shows a number of CII cells like the two seen in the figure. These are the non-physical circular CII features seen earlier in Figure 4.2. It is also clear that the carbon is highly ionised at large radii from the source, suggesting that the quasar ionises a larger volume of space than the whole simulation volume.

The lower panel in Figure 4.4 shows the hydrogen number density (on a log scale) calculated by `PMRT` for this LOS. The lower-ionisation features within the CVII region (i.e. the dips in f_{CVII} with corresponding increases in f_{CVI} and f_{CV}, around cells 18, 28, 57 and 75) clearly occur in overdensities seen as peaks in n_H. This matches the trend seen in the maps above. Similarly, the carbon is not fully ionised within the first ten cells closest to the quasar, but this is also the highest density region suggesting a high rate of recombinations.

The dashed lines in the main panel show the equilibrium fractions calculated by `Timedep` (see the following section). Within around 1.3Mpc of the quasar the carbon is in ionisation equilibrium. Further out the time-dependent ion fractions deviate from the equilibrium solutions, especially in the voids. The trend is for the time-dependent solutions to show the carbon as less ionised, with higher fractions of atoms in lower ion states compared with the equilibrium solutions. The results show that if the simulation had only calculated the equilibrium solutions, the general pattern of the spacial ionisation structure would have been similar, with lower ionisation at greater radii and no sharp boundaries between regions. The level of ionisation would have been higher without performing the time-dependent calculation.

The results presented so far have given a description of the ionisation of carbon (and

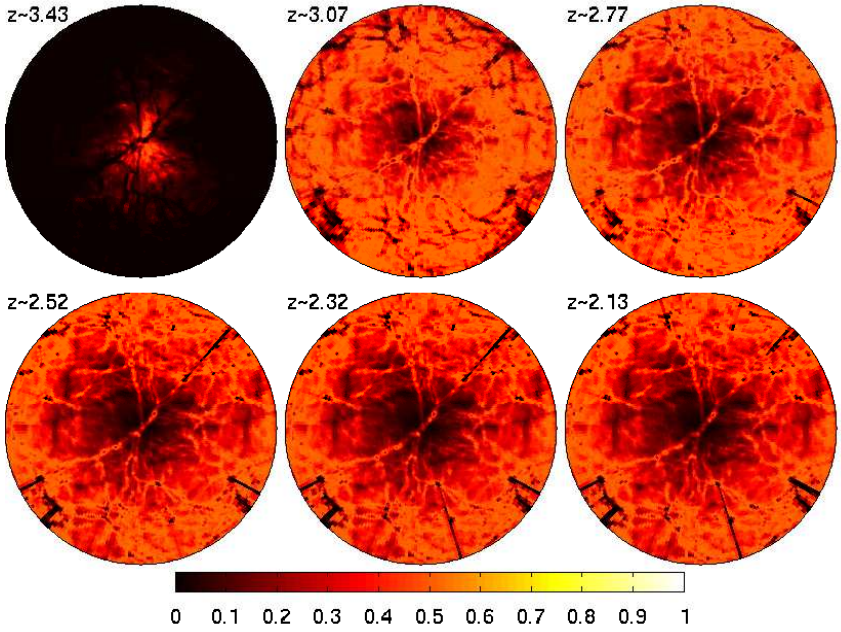

Figure 4.5: Maps of the equilibrium CVI ion fraction, $f_{CVI,eqm}$.

CVI in particular), and its variations across the volume and duration of the simulation. A more detailed comparison with the equilibrium results will be given in the next section, where maps for other carbon states and other elements are presented along with their equilibrium fraction maps.

Comparison with equilibrium

Figure 4.5 shows the equilibrium CVI ion fractions found by `Timedep`, using the same rates as its time-dependent calculation, for comparison with the time-dependent fractions in Figure 4.3. Figure 4.6 shows the absolute differences $(f_{eqm} - f)$ between them and Figure 4.7 shows the fractional difference $(f_{eqm} - f)/f_{eqm}$. These figures show that the equilibrium CVI ionisation fraction is mostly in good agreement with the time-dependent fractions[1], since the metals in the IGM are mostly in or close to ionisation equilibrium both before and a long time after the quasar turns on. However, the regions of interest for this investigation are those that are out of equilibrium while the IGM is

[1]N.B. For simplicity, I refer to the solutions of the equilibrium ionisation equations as the "equilibrium fractions" and to the solutions of the time-dependent ionisation equations as the "time-dependent fractions". It should be noted however, that even the time-dependent fractions are often in equilibrium, and of course both sets of results vary with time (i.e. are "time-dependent") as the radiation source and the IGM density and temperature evolve.

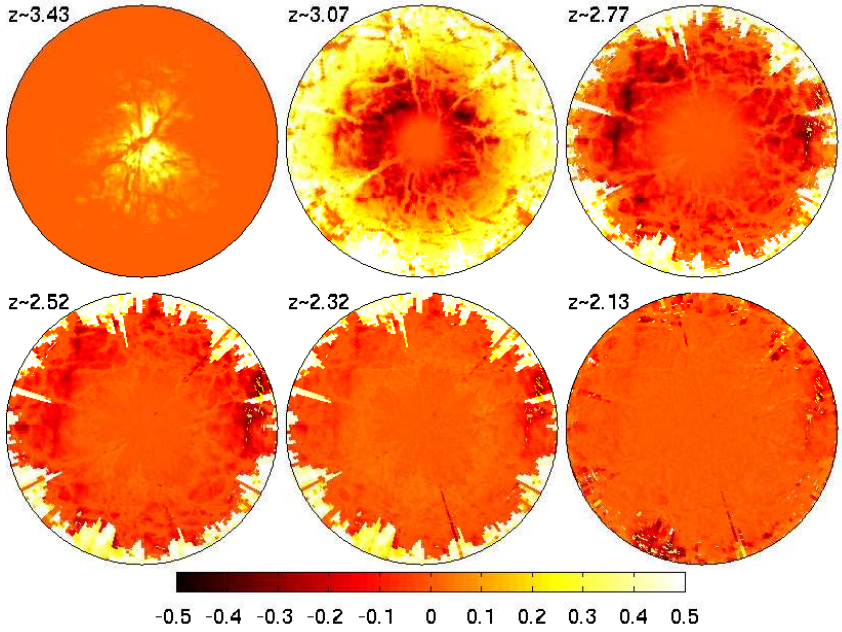

Figure 4.6: Maps of the CVI absolute difference from equilibrium, at six timesteps. The background colour shows cells with zero absolute difference, $f_{eqm} - f = 0$; darker cells show $f > f_{eqm}$; lighter cells show $f < f_{eqm}$.

reacting to the young quasar.

The most obvious difference between the Figures 4.5 and 4.3 is the lack of the CIII region in the equilibrium results (as discussed above). The first map in Figure 4.5 shows a region of CVI created as the quasar turns on, which is much larger than that seen in the time-dependent results. This shows that following the rapid change in conditions by the quasar turning on, the IGM immediately surrounding the quasar has not had time to reach ionisation equilibrium. The second map in Figure 4.6 shows how the central region nearest the source has reached equilibrium by 250Myr after the quasar turns on. The subsequent maps show how gas at larger radii takes longer to reach equilibrium (seen as an expanding central region of equilibrium).

It appears that the regions of the simulation which have CVI furthest from equilibrium are the voids. Between $z \approx 3.07$–2.52, certain radii (outside the central region in equilibrium) show an excess of CVI where the carbon is less ionised than if it had yet reached equilibrium, but traced out against these dark regions are the dense structures seen in the background (zero) colour, showing very low deviation from equilibrium. However, the timescales of scientific interest are those (shorter ones) which do show transient effects with non-equilibrium ionisation.

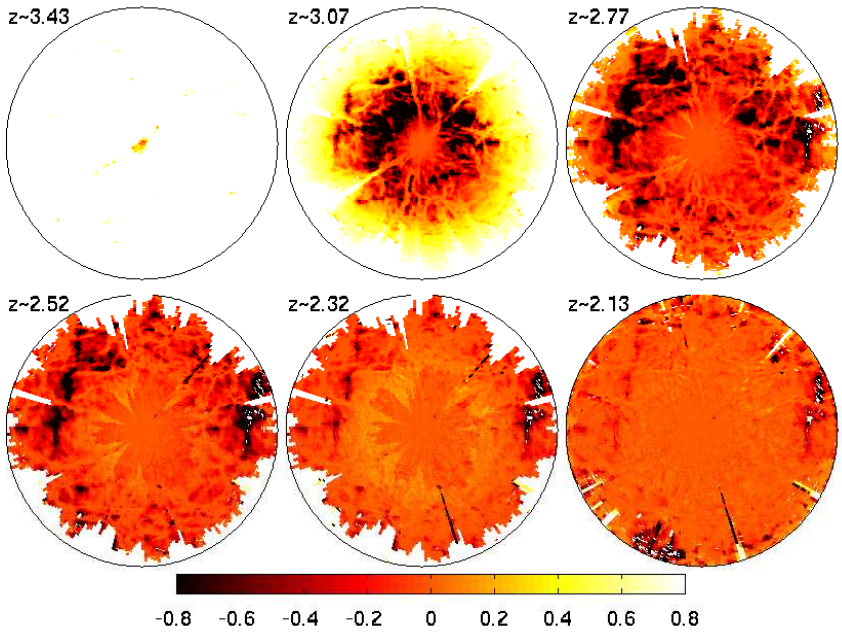

Figure 4.7: Maps of the CVI fractional difference from equilibrium, at six timesteps after the QSO turns on. The background colour shows cells with zero fractional difference, $(f_{eqm} - f)/f_{eqm} = 0$; darker cells show $f > f_{eqm}$; lighter cells show $f < f_{eqm}$.

This simulation models the ionisation in the immediate vicinity of a quasar, so it is not surprising that the metals become extremely ionised, and that lower ionisation states (which are more commonly observed, such as CIV, CII, SiII and SiIV) are not very occupied. However, these lines are easily observed not only due to their abundance but also their the wavelength and strengths of their resonance transitions. Therefore it is interesting to study the effect of the `Timedep` calculation on the abundances of these species, as they may be observable even if they are not the dominant species.

The CIV ion fraction is mapped in Figure 4.8 at six timesteps throughout the simulation. At the start of the simulation there is no CIV but by the time the quasar turns on at $z \sim 3.5$, the starburst galaxy has already ionised the nearby IGM which is not shielded by dense regions, to produce CIV. The quasar then further ionises the carbon, reducing the fraction of atoms as CIV, until by $z \sim 2.5$ there is already virtually no CIV (except in the anomalous HI/CIII region). Figure 4.9 shows six consecutive timesteps over a period of 126Myr as the quasar turns on. While the luminosity increases during the first three steps, the CIV fraction increases most obviously in the pre-ionised regions. The CIV front then blasts out (even into the previously shadowed regions)

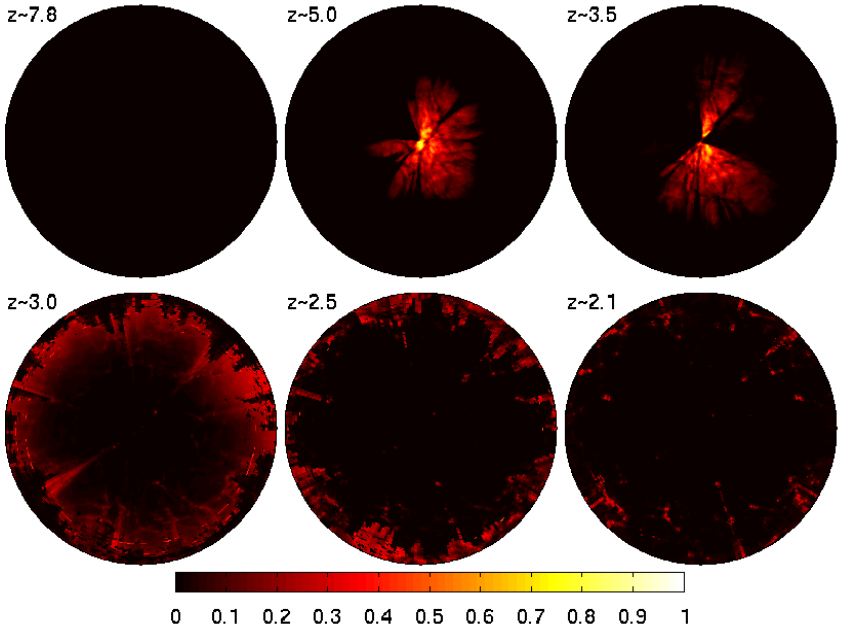

Figure 4.8: Maps of the CIV ion fraction.

by $z \sim 3.35$. The expanding CIV region which fills most of the simulation volume by $z \sim 3.27$ is replaced by the expanding regions of higher ionisation which replace CIV as the dominant ion state throughout most of the volume by $z \sim 3.0$.

Figures 4.10 and 4.11 show the absolute difference between the equilibrium and time-dependent CIV ionisation fractions ($f_{eqm} - f$) for the same timesteps. The background orange colour in both figures shows regions where the time-dependent fractions are in ionisation equilibrium. The colour-scale in Figure 4.10 is narrower, and shows the small differences in modelling the starburst's CIV ionisation. Figure 4.11 has a wider scale and shows the stronger deviation from equilibrium as the quasar turns on. The yellow regions indicate that the time-dependent f_{CIV} is less than the equilibrium value, showing that under the assumption of ionisation equilibrium, the quasar would ionise the surrounding carbon (in all directions) to CIV much more quickly. The black region marks the time-dependent calculation's strong CIV front (which exceeds the equilibrium calculation's CIV fraction). The central orange region shows the time-dependent results are in equilibrium, having a very low CIV fraction.

Figures 4.12, 4.13 and 4.14 show the CII fraction time-dependent results, equilibrium results, and the difference between them, all at the same six timesteps throughout the simulation. In the first maps at $z \sim 7.8$, the `Timedep` calculation has the carbon

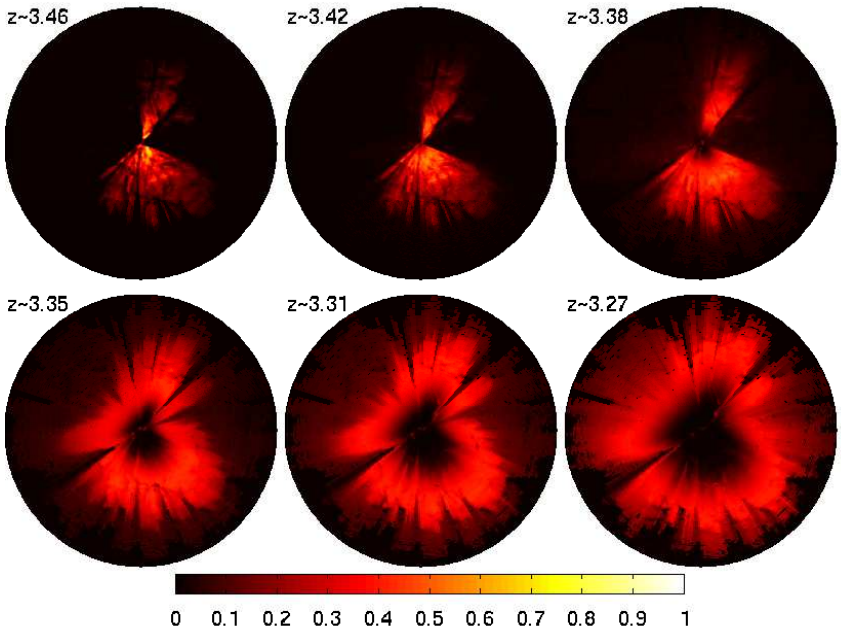

Figure 4.9: Maps of the CIV ion fraction as the quasar turns on.

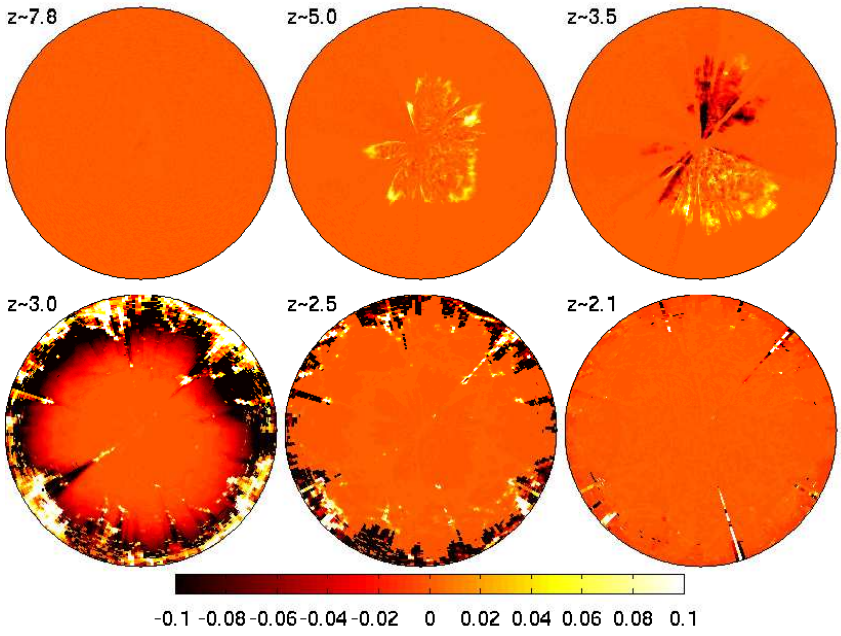

Figure 4.10: Maps of the CIV absolute difference from equilibrium, at six timesteps. The background colour shows cells with zero absolute difference, $f_{eqm} - f = 0$; darker cells show $f > f_{eqm}$; lighter cells show $f < f_{eqm}$.

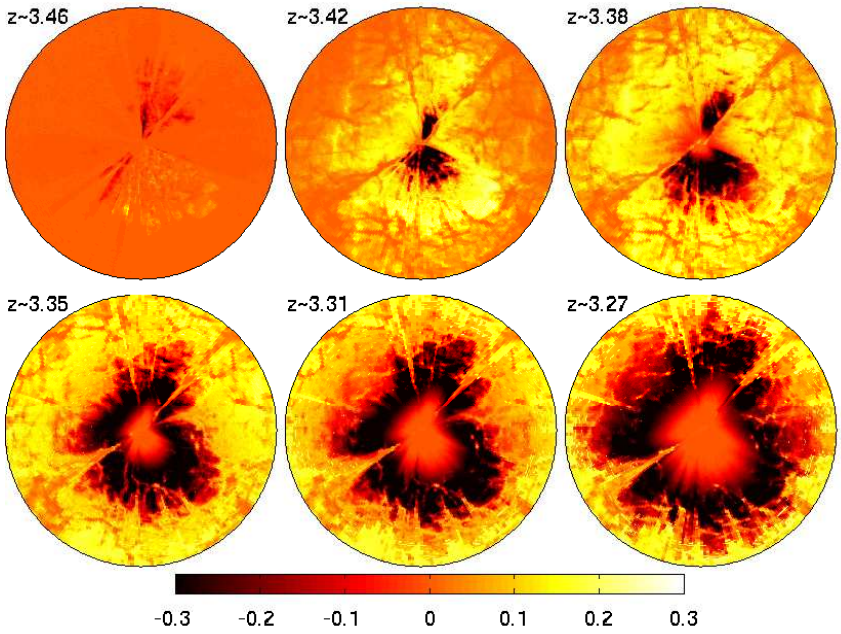

Figure 4.11: Maps of the CIV absolute difference from equilibrium, at six timesteps while the QSO turns on. The background colour shows cells with zero absolute difference, $f_{eqm} - f = 0$; darker cells show $f > f_{eqm}$; lighter cells show $f < f_{eqm}$.

virtually all singly-ionised to CII, whereas the equilibrium results show very little CII, giving a big difference in Figure 4.14. After this, the time-dependent and equilibrium results are very similar. CII dominates throughout most of the volume while the starburst galaxy is the only source of ionising photons, except for a central region dominated by CIII (seen as the dark region in the second and third maps of Figures 4.12 and 4.13, and also seen in Figure 4.2). The absolute difference map at $z \sim 5$ in Figure 4.14 shows a darker ring just at the front of the CIII region, showing a slight excess of CII relative to equilibrium suggesting the CIII front has moved less far. By $z \sim 3.5$ the central region is becoming brighter as more of the CII in the time-dependent calculation is ionised out of equilibrium. Once the quasar turns on there is no CII throughout most of the volume in either set of results. Figure 4.14 clearly shows the 'noise' in the `Timedep` results creating an artificial difference from equilibrium. As has been noted earlier, these changes in some cells at certain radii particularly affect CII and CIII fractions. This noise is prominent in the second to fifth time-dependent ionisation maps, and absent from the equilibrium maps, therefore showing up clearly in the absolute difference maps.

The behaviour of silicon in this simulation is broadly similar to carbon. The results

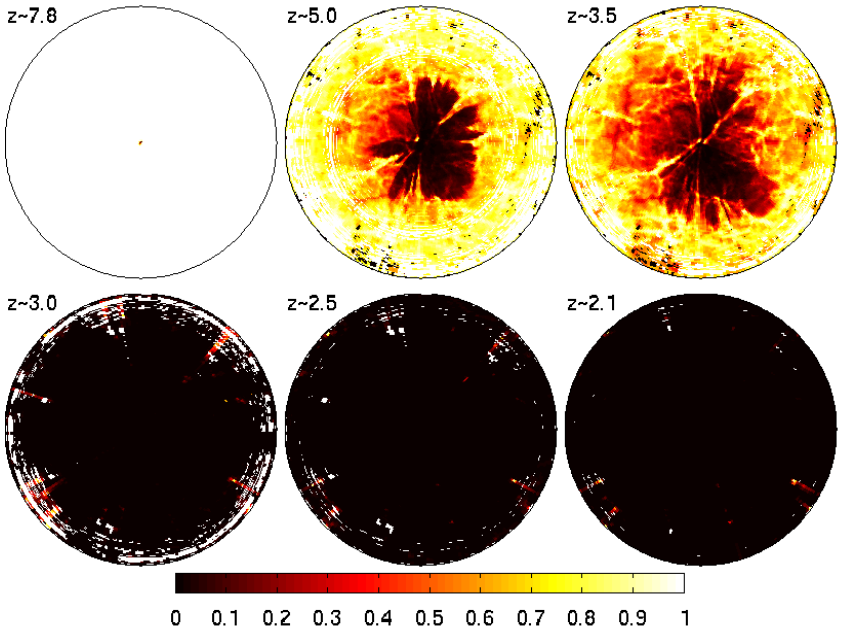

Figure 4.12: Maps of the CII ion fraction.

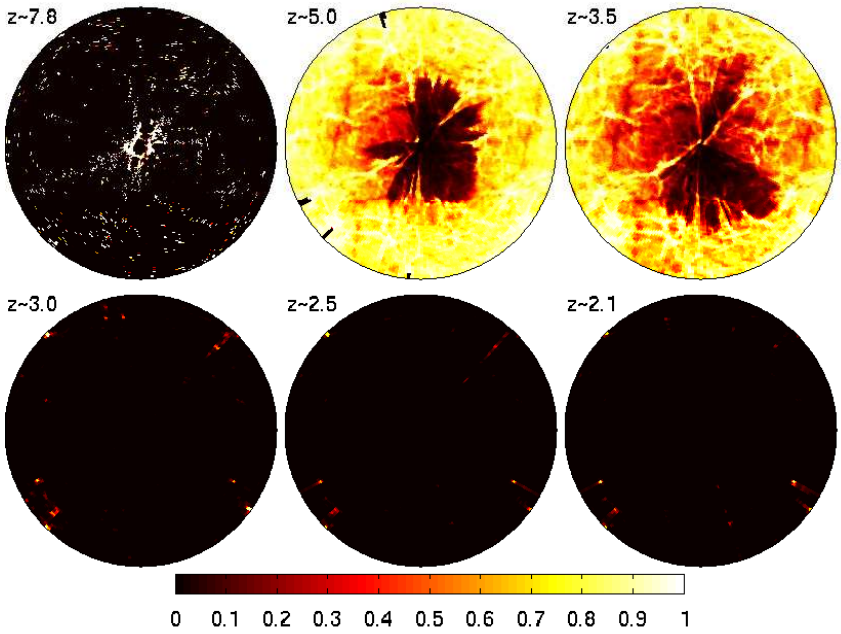

Figure 4.13: Maps of the equilibrium CII ion fraction.

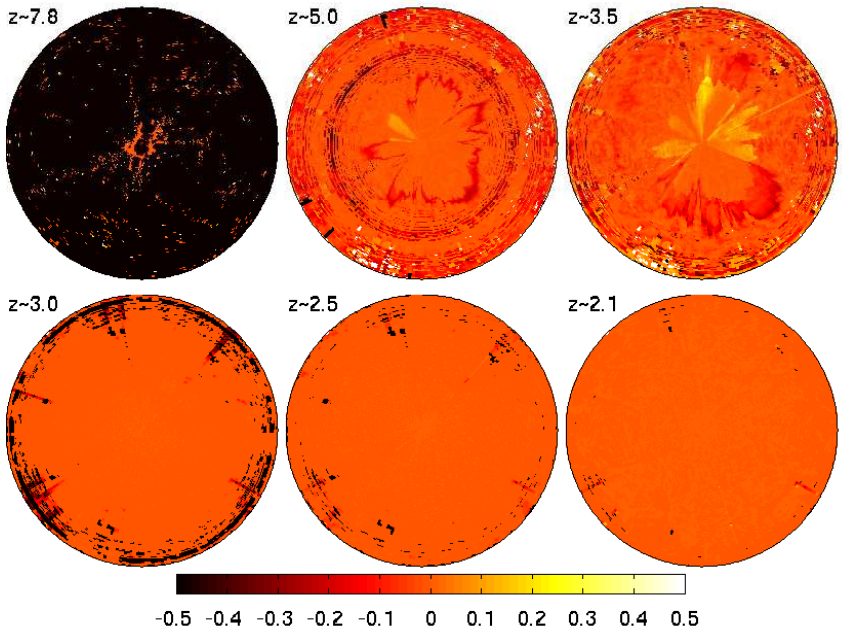

Figure 4.14: Maps of the CII absolute difference from equilibrium, at six timesteps. The background colour shows cells with zero absolute difference, $f_{eqm} - f = 0$; darker cells show $f > f_{eqm}$; lighter cells show $f < f_{eqm}$.

for SiIV are plotted in Figures 4.15, 4.16 and 4.17. As for the CIV in Figures 4.8 and 4.9, there is a small SiIV fraction in a central region during the starburst phase. When the quasar turns on, a SiIV front followed by other higher fronts blast through the surrounding IGM. By $z \sim 3.01$ there is no SiIV in the volume except in the anomalous HI/CIII region along the periphery. During the starburst phase, there are some radial regions that are black in the second to fourth panels of Figure 4.17. This shows that the time-dependent SiIV fraction is higher than in equilibrium, showing how some sightlines from the quasar are being ionised out of equilibrium (although these differences are only small). The other features during the starburst phase, show the SiIV region has not reached as far as it would under the assumption of equilibrium. The SiIV absolute difference map at $z \sim 3.35$ corresponds to the same timestep as the fourth CIV map in Figure 4.11. Again, the outer yellow region shows that the metals are not as ionised in the time-dependent calculation, i.e. the silicon in the outer regions has not yet had enough time to respond to the changing radiation field. The black region and central orange region show the expanding SiIV region and the inner region of higher ionisation (which has a very low SiIV fraction so appears as equilibrium) at $z \sim 3.35$.

SiII maps are not included here because even the starburst spectrum is strong

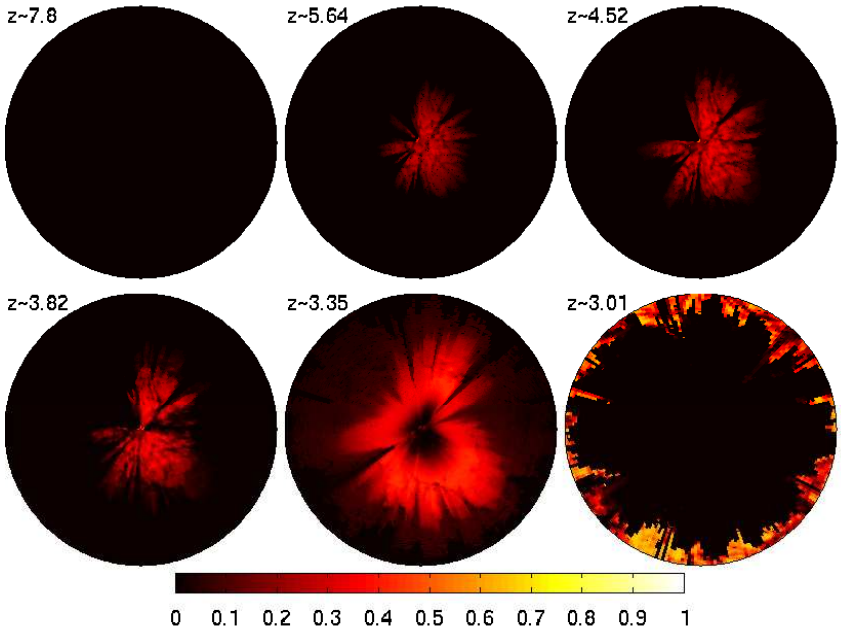

Figure 4.15: Maps of the SiIV ion fraction.

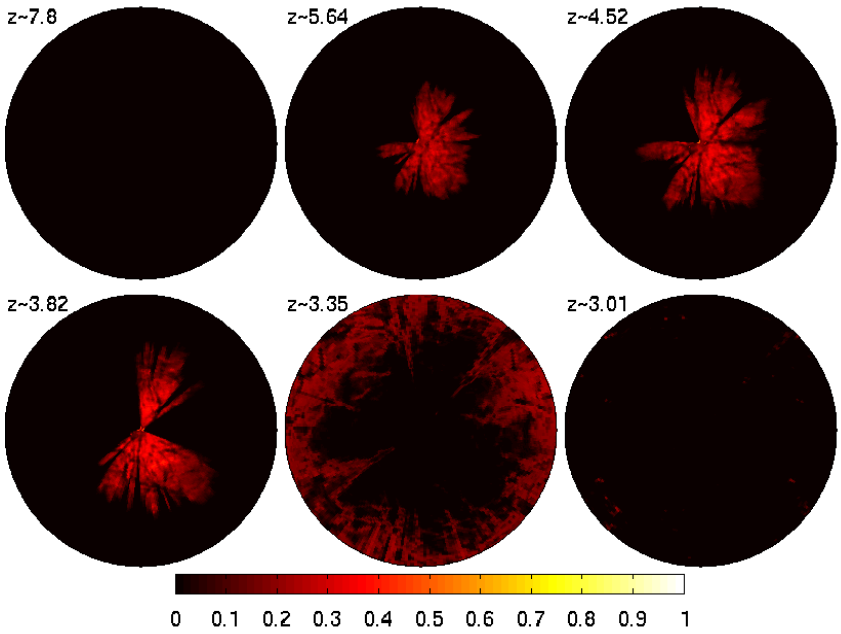

Figure 4.16: Maps of the SiIV equilibrium ion fraction.

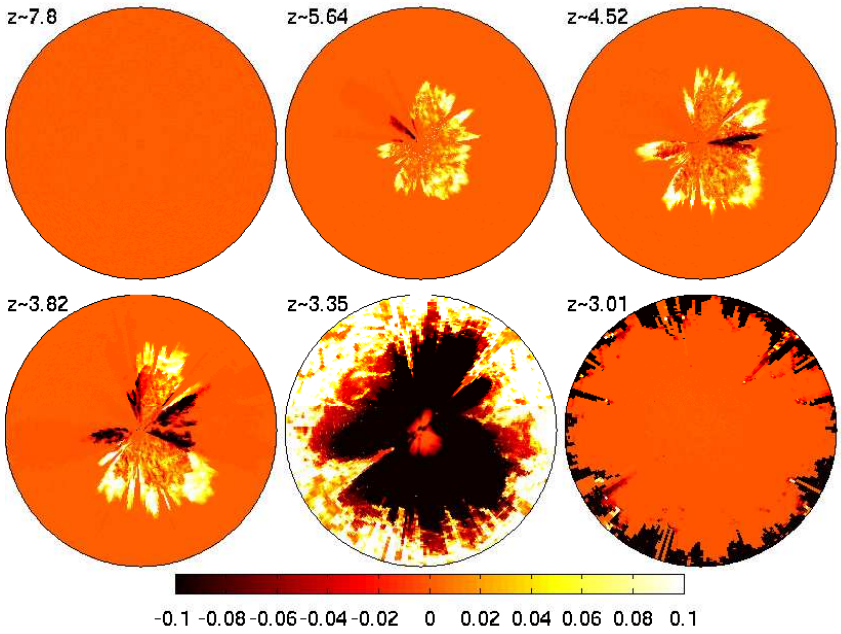

Figure 4.17: Maps of the SiIV absolute difference from equilibrium, at six timesteps. The background colour shows cells with zero absolute difference, $f_{eqm} - f = 0$; darker cells show $f > f_{eqm}$; lighter cells show $f < f_{eqm}$.

enough to ionised the Si past this state. At $z \sim 7.8$ the silicon is all SiII, but it quickly ionises to higher states and for the rest of the simulation, the only SiII is in the outer HI/CIII region or a few anomalous cells. Instead, the SiIII ion fraction is plotted in Figure 4.18 at the same timesteps as the SiIV plots. At the start of the simulation and again by $z \sim 3$ there is no SiIII (except in the outer HI/CIII region). During the starburst phase, the majority of the silicon is SiIII, with a lower fraction close to the source where there is a significant fraction of SiIV, and in the anomalous outer region. Figure 4.19 shows that the SiIII is mostly well in equilibrium in most regions at the six plotted timesteps. The outer HI/CIII region is shown in white as the anomalous time-dependent f_{SiIII} is lower here than the equilibrium value (1.0) that should have been found out to the edge of the volume. The black features at the edge of the central region during the starburst phase show that the SiIV region is not spreading as fast as in the equilibrium results. The fifth map, at $z \sim 3.35$ shows a central region in equilibrium, which has a very low SiIII fraction, as in the final map. The majority of the volume is black, showing the lower equilibrium SiIII fraction than the time-dependent result, as the ionisation to higher states in the `Timedep` results is lagging behind the changing physical conditions.

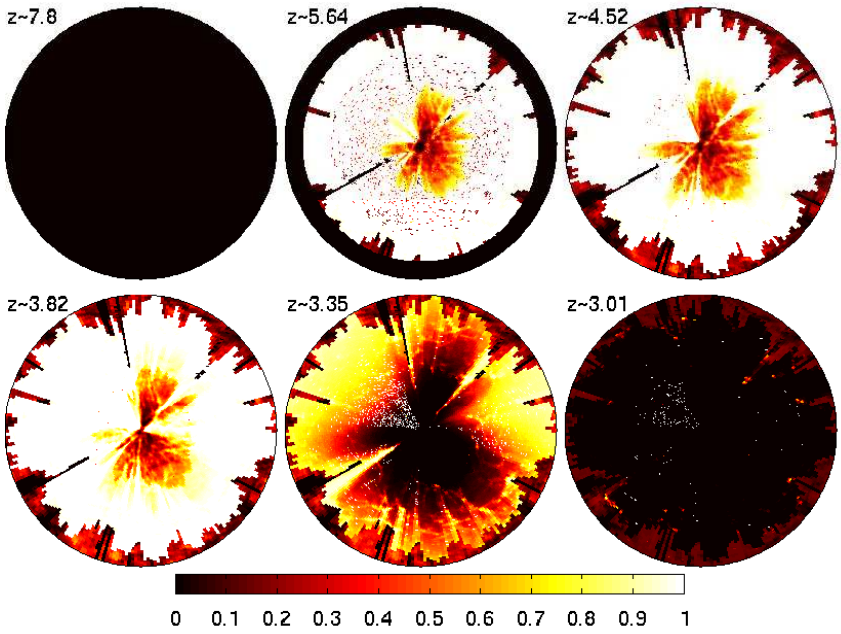

Figure 4.18: Maps of the SiIII ion fraction.

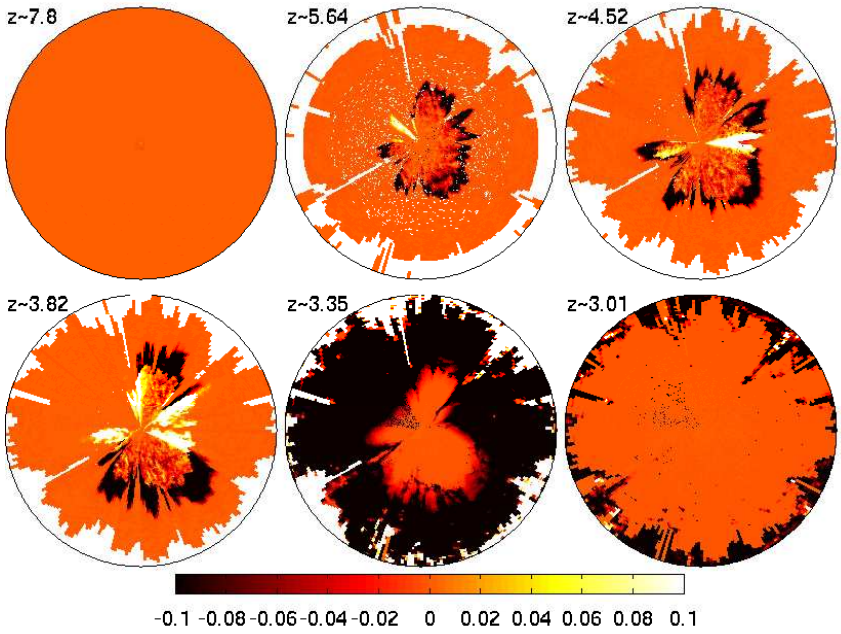

Figure 4.19: Maps of the SiIII absolute difference from equilibrium, at six timesteps. The background colour shows cells with zero absolute difference, $f_{eqm} - f = 0$; darker cells show $f > f_{eqm}$; lighter cells show $f < f_{eqm}$.

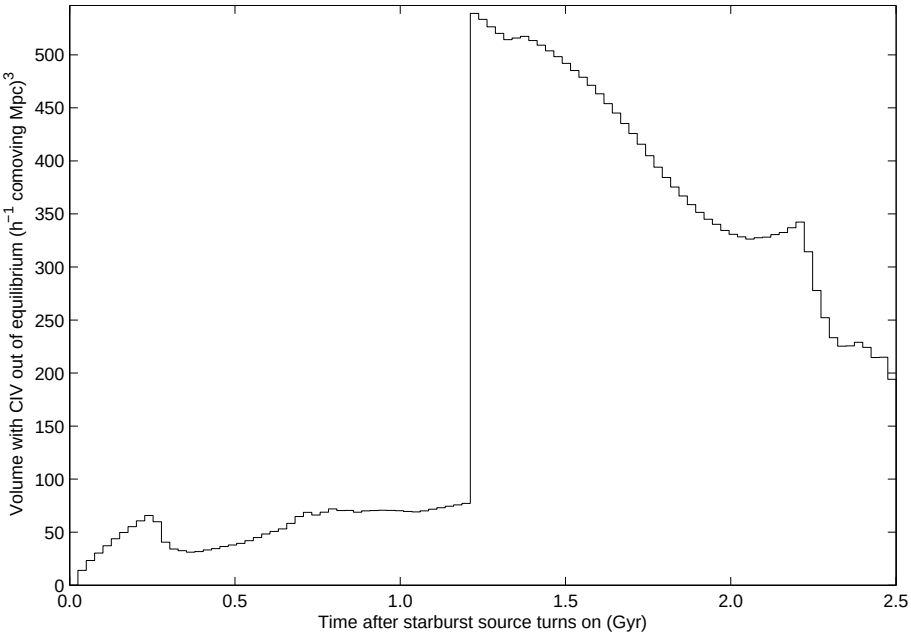

Figure 4.20: The volume of the simulation which has CIV out of equilibrium, as a function of time. A cell's CIV is 'out of equilibrium' if $|f_{CIV,eqm} - f_{CIV}|/f_{CIV,eqm} > 0.1$ (and only cells with $f_{CIV,eqm} > 10^{-4}$ are included). The limit of the y-axis is the volume of the full simulation, $546(h^{-1}\mathrm{Mpc})^3$ comoving. Notable features are the small volume with CIV out of equilibrium during the starburst phase; the time of the quasar turning on, leaving the CIV out of equilibrium throughout the volume; and the gradual return to equilibrium for most of the volume.

Global properties

Next, the ionisation behaviour of CIV is discussed for the whole simulation volume throughout the duration of the run. Figure 4.20 shows as a function of time, the (comoving) volume of the simulation which has CIV out of equilibrium. The limit of the y-axis is the volume of the full simulation, $546(h^{-1}\mathrm{Mpc})^3$ comoving, so the plot also shows the 'filling factor' of non-equilibrium CIV. The non-equilibrium volume is calculated by summing the volume of all cells at each timestep which meet some criteria, here that the fractional difference $|f_{CIV,eqm} - f_{CIV}|/f_{CIV,eqm}$ is greater than 0.1, and that the equilibrium fraction itself is greater than 10^{-4}.

After the starburst source turns on at the beginning of the simulation ($z = 8$), the comoving volume which has CIV out of equilibrium increases, as carbon in the region nearby to the source lags behind the equilibrium ionisation. A few hundred megayears later, the inner region reaches equilibrium, reducing the non-equilibrium CIV volume. This non-equilibrium volume then expands gradually in the simulation frame, before

settling down (still under the starburst UV spectrum) and staying at around 12% of the comoving volume until the QSO turns on at $z = 3.5$. Throughout the whole volume this leaves the CIV out of equilibrium, as the quasar's high UV flux would ionise the carbon in the equilibrium model, but in the more realistic time-dependent model, the carbon cannot react so quickly to the changing conditions. Over time, the non-equilibrium volume decreases as the time-dependent CIV reaches equilibrium and also the carbon is further ionised by the quasar radiation, so the CIV fraction drops.

The importance of this plot is in showing the huge fraction of the volume which has CIV out of equilibrium when the source turns on, and the rate at which the volume then returns to equilibrium (over a very long time, rather than immediately returning to equilibrium, or the whole volume staying out of equilibrium for example). Producing the same plot, but weighting each cell by its (final) fraction of the total simulation mass gives Figure 4.21. This confirms that the cells with CIV out of equilibrium are not simply under-dense voids, but that much of the *mass* of the IGM near a quasar can be left out of equilibrium when it turns on. Indeed, half of the mass is still out of equilibrium one gigayear after the quasar turned on.

Figure 4.22 shows how long different fractions of the simulation (comoving) volume had CIV out of equilibrium with $|f_{CIV,eqm} - f_{CIV}|/f_{CIV,eqm} > 0.1$, and $f_{CIV,eqm} > 10^{-4}$. The plot is a histogram of cells, each weighted by their volume, and the bars all sum to the total simulation volume. The maximum period that each cell's CIV spent out of equilibrium has been calculated from the number of consecutive timesteps at which it met the same criteria as in Figure 4.20. The large spike in the data shows that a large fraction of the simulation volume (14%) has CIV out of equilibrium for a maximum of 1.29Gyr. This corresponds to the time between the quasar turning on and the end of the simulation. As seen in Figure 4.20, more than 36% of the simulation volume still meets this CIV non-equilibrium condition at the end of the simulation (seen in maps to be cells at the outside of the simulation, furthest from the source). Of these cells, the spike in Figure 4.22 represents those which were constantly out of equilibrium since the quasar turned on, leaving (almost) the entire volume out of equilibrium. Figure 4.23 shows the histogram of cells weighted by their fraction of the total simulation mass. Cells have not been counted for this plot at timesteps when they returned an error. This histogram has other peaks showing large fractions of the mass out of equilibrium for coherent lengths of time. These times mostly correspond to small peaks in Figure 4.22, therefore showing regions with relatively high mass (i.e. with high densities) out of equilibrium for coherent lengths of time. Figure 4.23 also has the strong peak at 1.29Gyr, showing

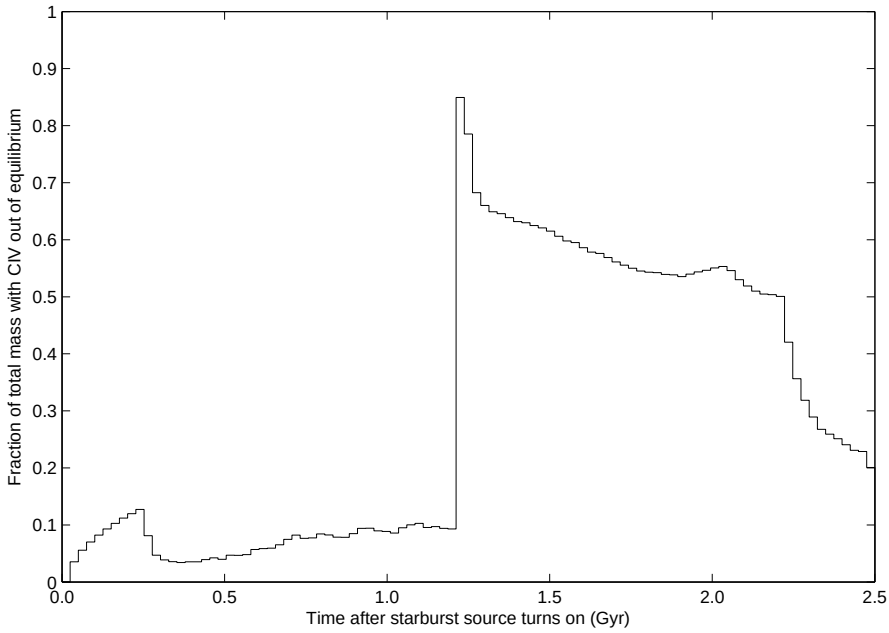

Figure 4.21: As Fig. 4.20 but with cells weighted by their fraction of the total simulation mass, showing the mass-fraction of the simulation which has CIV out of equilibrium, as a function of time. A cell's CIV is 'out of equilibrium' if $|f_{CIV,eqm} - f_{CIV}|/f_{CIV,eqm} > 0.1$ (and only cells with $f_{CIV,eqm} > 10^{-4}$ are included). Notable features are the small mass with CIV out of equilibrium during the starburst phase; the time of the quasar turning on, leaving up to 85% of the simulation's mass with CIV out of equilibrium; and the slow return to equilibrium, with 50% of the mass still out after 1Gyr.

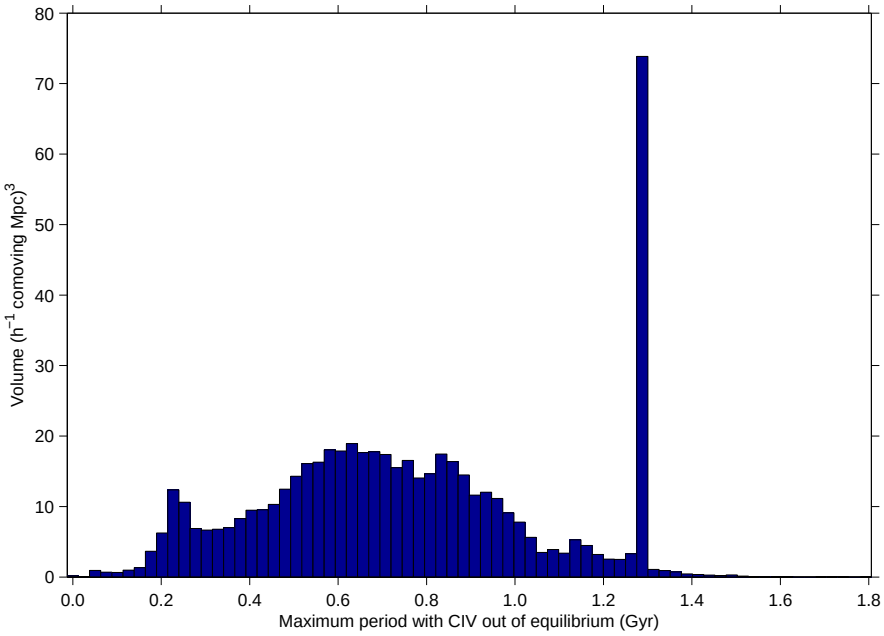

Figure 4.22: A histogram of the simulation cells weighted by their volumes, showing the maximum time the CIV in each cell was out of equilibrium. Note that the bars sum to the total volume $546.4(h^{-1}$ comoving Mpc$)^3$. The large peak shows the volume of the simulation which remains out of equilibrium from the turning-on of the quasar until the end of the simulation.

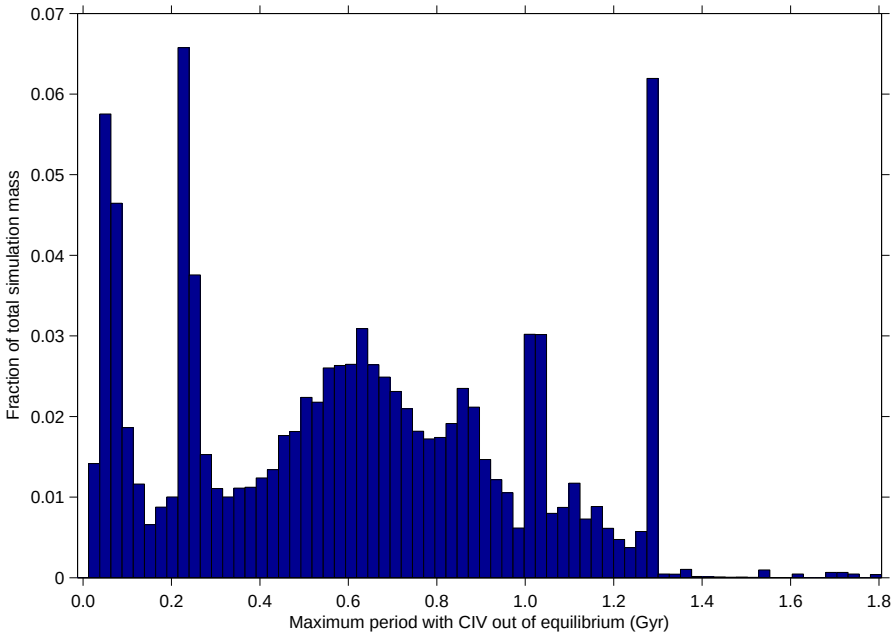

Figure 4.23: A histogram of the simulation cells as in Fig. 4.22 but with cells weighted by their fraction of the total simulation mass, showing the mass-fractions which have their CIV out of equilibrium for the given maximum times. Note that the bars sum to unity. Most of the large peaks correspond to features in Fig. 4.22, therefore showing high-density cells out of equilibrium for coherent lengths of time.

that a large amount of the IGM mass around the quasar still has CIV out of equilibrium (according to the chosen thresholds) at the end of the simulation. This shows the huge timescales over which a bright source can keep IGM metals out of equilibrium.

4.4 Quasar death

The simulation analysed in this chapter deals only with the ionisation around a new quasar that turns on in a region of the IGM. It is also of interest to consider the time-dependent ionisation of metals in the IGM nearby to a quasar when it turns off. In this section, results from such a simulation will briefly be presented (before returning to the main simulation in the next chapter to produce mock spectra).

As with the previous `PMRT` simulation, this one has an initial starburst galaxy spectrum which turns on at $z = 8$. In the new simulation, the quasar phase begins earlier at $z_{QSO} = 4.5$, with the spectrum completing its transition to a pure quasar spectrum by $z = 3.5$. The quasar spectrum is again a hard power-law spectrum $L_\nu = L_L(\nu/\nu_L)^{-\alpha}$ with $\alpha = 0.5$, but has a lower luminosity with $L_L = 2 \times 10^{30}\mathrm{erg\,s^{-1}Hz^{-1}}$. The central source ends its quasar phase at $z_{off} = 3$ and the spectrum is turned off, while the simulation continues until its end at $z = 2$. The other details of the simulation are the same as described for the previous simulation in Section 4.1.

Figure 4.24 shows maps of the most highly occupied ion state of carbon throughout the simulation, at six different timesteps. The first two maps show ionisation by the starburst spectrum. By $z = 3.5$ the source has become a quasar and is ionising the carbon to higher states. The carbon stops becoming more ionised when the source turns off at $z = 3$. The lower three maps therefore show evolution of the ionisation while there is no photoionisation source. The IGM begins to recombine to lower ionisation states. Towards the end of the simulation, the recombination slows and some regions return to a higher ionisation state.

Figures 4.25 and 4.26 show the evolution of the CIV fraction in the simulation, and its deviation from equilibrium. As seen in Figure 4.24, the starburst spectrum has ionised a small region of CIV nearby to the quasar by $z \sim 7.6$, and this region grows over time, becoming anisotropic because of overdensities casting shadows that shield some regions from the galaxy's radiation. By the third map at $z \sim 3.43$, the quasar is rapidly ionising the carbon. CIV has a significant fraction throughout most of the volume except in two wide and two narrow shielded regions, and it dominates in an expanding region seen around a third of the way out through the simulation

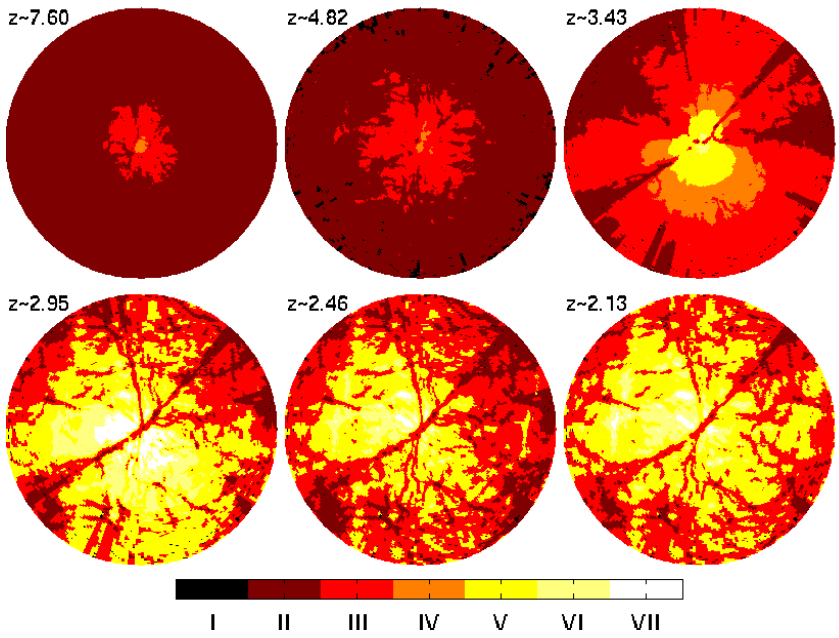

Figure 4.24: Maps showing the most highly occupied ion state of carbon in each cell, from neutral CI to fully ionised CVII, at six timesteps. See the text for a description of the source's evolution and its effect on the ionisation.

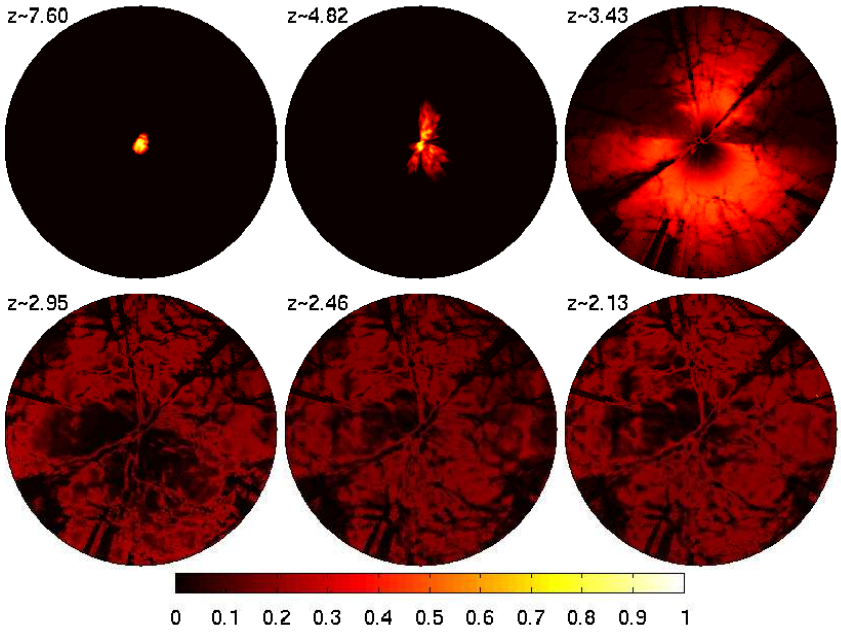

Figure 4.25: Maps of the CIV ion fraction.

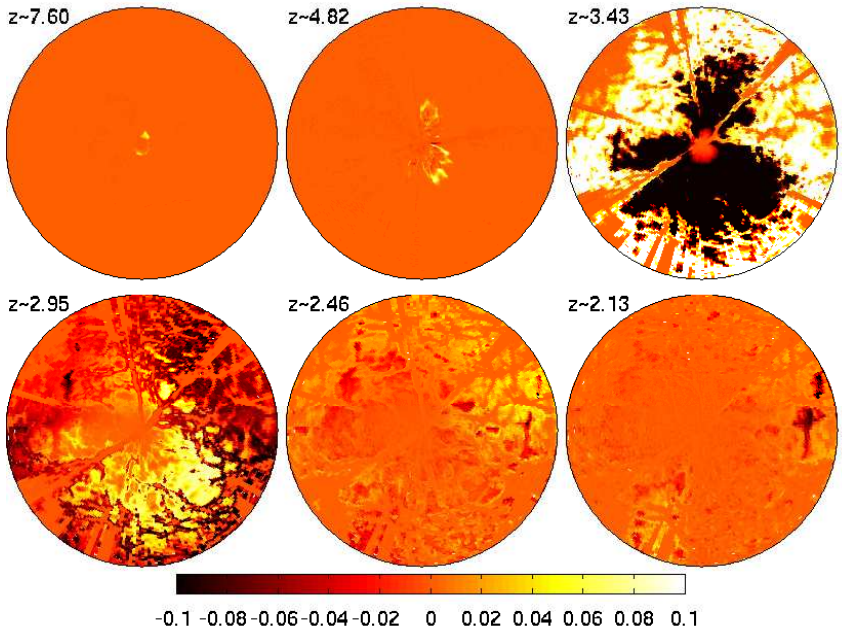

Figure 4.26: Maps of the CIV absolute difference from equilibrium, at six timesteps. The background colour shows cells with zero absolute difference, $f_{eqm} - f = 0$; darker cells show $f > f_{eqm}$; lighter cells show $f < f_{eqm}$.

from the source. By the time the source turns off at $z = 3$, the quasar has ionised the carbon throughout most of the volume to CV and CVI, with some outer regions still dominated by CIII. The fourth panel of Figure 4.25 shows the CIV fraction seen throughout the CV and CIII regions. As the gas continues to recombine in the absence of ionising radiation, the CVI region returns to being dominated by CV or CIII, and its CIV fraction increases. The CIV fraction then remains rather constant throughout the volume until the end of the simulation, even while some regions see a decrease in CIII and an increase in CV.

Comparing the first two panels of Figures 4.25 and 4.26 shows that the CIV region created by the starburst spectrum is mostly in equilibrium. The quasar then knocks the CIV out of equilibrium as the gas takes time to respond to the increased level of flux. The third panel of Figure 4.26 shows regions in yellow and white where there is a lack of CIV as the time-dependent fractions have not had yet time to ionise to match the equilibrium CIV fraction. The dark region in that map shows an excess of CIV where the gas has not had time to ionise past CIV to the higher states found in the equilibrium fractions. A small region at the centre of the simulation is seen to be in equilibrium, but in this region both sets of fractions have ionised past CIV so agree on

a negligibly small fraction.

The photoionisation rates for the carbon ions is not the only way that the quasar affects the carbon's ionisation balance. The quasar's photoionisation of the hydrogen and helium raises the gas temperature and the number density of electrons, which has big effect on metal ionisation. The fourth panel in Figure 4.26 shows the CIV out of equilibrium after the source has turned off at $z = 3$. When the quasar did turn off, the carbon's photoionisation rates drop to zero, which immediately affects the equilibrium fractions. By contrast, the temperature and the number density of electrons take time to relax once the source turns off, so the effect on the carbon equilibrium fractions of turning off the quasar is slower than would be expected by considering the photoionisation rates alone. This allows the time-dependent carbon fractions to stay closer to equilibrium than expected while they recombine. By $z \sim 2.46$, most of the simulation volume has nearly recombined to equilibrium (with yellow showing regions with not enough CIV), and by $z \sim 2.13$, only small regions remain with CIV out of equilibrium.

4.5 Summary

In this chapter, an application of the `Timedep` algorithm to a full cosmological IGM simulation has been demonstrated:

- `Timedep` was used to post-process the output from a joint particle-mesh and radiative-transfer simulation of the effect of a new quasar turning on in a region of the IGM that was pre-ionised by a starburst galaxy. Whereas the original simulation modelled the ionisation of just hydrogen and helium, `Timedep` is able to evaluate the time-dependent ionisation of heavy elements as well, and the results for carbon and silicon have been presented.

- The example of carbon shows that starburst spectrum ionises it to mostly CIII and CIV before the quasar turns on, and then after $z = 3.5$ the gas gets further ionised by the quasar's spectrum up to high fractions of CVI and CVII.

- The ionisation structure produced around the source galaxy does not have sharp boundaries between ionisation regions, but rather the relative fractions of different ion states vary smoothly with radius (as seen in Figure 4.4). Closer to the source, the stronger radiation field produces higher ion states.

- Whilst the majority of the simulation volume and timesteps show physical effects in the IGM, there are some features which suggest that there are still bugs in the `Timedep` code. With more time I will identify the cause of the HI region which appears at the periphery of the volume after the quasar turns on, to confirm that the same problem does not independently affect the metals. Also, concentric rings of alternating ionisation levels are seen in the CII and CIII results, and are again not expected to be physical, and investigation to date has not revealed their origin. An explanation of these 'bugs' will be investigated further, to confirm that there are no other unexpected influences. However, the majority of the results for metal ionisation appear to be independent of these bugs, producing reliable data.

- Mapping the difference between ion fractions calculated by `Timedep` or assuming ionisation equilibrium, at different times while the young quasar ionises the surrounding IGM, has shown the regions of the simulation which have certain elements or states out of equilibrium. Although different thresholds can be chosen as showing gas 'out of equilibrium', it is clear to see that, at least for some important states, the IGM metals take a very long time to reach ionisation equilibrium. For a CIV fractional difference from equilibrium greater than 0.1 (for cells with $f_{CIV,eqm} > 10^{-4}$), over 99% of the simulation volume has CIV out of equilibrium for more than 10^8 years and 23% is out for over 10^9 years. 14% of the volume has not reached equilibrium by the end of the simulation (1.29×10^9 years after the quasar turns on), and of the rest of the volume, the volume-weighted mean time that the CIV is out of equilibrium is 6.7×10^8 years. This is the same order of magnitude as estimates for the lifetimes of quasars, and highlights the significance of this time-dependent ionisation work for future IGM observations or simulations where bright sources may make ionisation-equilibrium a poor approximation.

- Finally for this simulation, the fractions of the whole simulation volume and mass, which have (as an example) CIV out of ionisation equilibrium, have been studied, and how long the different cells remain out of equilibrium. The results show that the non-equilibrium effects revealed by the time-dependent ionisation calculations are important through a large fraction of the volume and mass of the IGM around a young quasar.

- Another simulation was presented in which the new quasar is later turned off, and the subsequent recombination of the carbon has been studied. The time taken for

the temperature and electron density to relax after the source turns off reduces the carbon's deviation from equilibrium during this recombination.

Chapter 5

Mock Quasar Absorption Spectra

5.1 Introduction

One of the main tools for understanding quasar absorption features is the production of simulated absorption spectra from lines of sight (LOS) placed through IGM simulation volumes. Since we can receive no other information about the IGM, the ability to reproduce the observed absorption features has been essential to forming our current understanding — that the gas in the IGM behaves like that in cold dark matter simulations, collapsing under gravity along with the hierarchical formation of dark matter structures, to form sheets, filaments and spherical halos that show increasing column densities (Rauch, 1998).

The IGM simulations provide spacial information on the density of the absorbing baryon species (e.g. n_{HI} or n_{HeII}) which is then integrated along some chosen LOS through the volume for each frequency to give the optical depth τ_ν. The transmitted flux which would be observed along the line of sight, after absorption from some incident flux normalised to unity, is then given by $e^{-\tau_\nu}$. This *transmission function* can then be compared with observed spectra normalised to a unity continuum level, or be multiplied by some mock quasar emission spectrum and convolved with a typical instrument broadening function to produce spectra resembling those that we observe.

In this chapter I will discuss the production of transmission functions through the quasar simulations described in Chapter 4, and discuss the effects of the time-dependent

ionisation calculations on the results, by comparing to transmission functions produced from simulation results which assume ionisation equilibrium.

5.2 Generating transmission functions

I was provided with a programme (written in C and IDL) for producing mock transmission functions along lines of sight through the `PMRT` simulations. This was written by Eric Tittley (used by Meiksin et al., 2010) based on a code by Meiksin and White (2001), and generates transmission functions for the hydrogen and the helium in `PMRT` simulations.

The x-axis of the transmission functions is given as the velocity of the absorbing gas relative to some arbitrary background source. For the gas in each cell of the simulation, this is equal to a Hubble velocity relative to the far side of the simulation box (which is different for each cell), plus the peculiar velocity of the gas relative to the simulation frame. Therefore, although the x-axis of the spectra broadly relates to positions across the volume, any of the spectral bins can include contributions from gas in different cells if they have different peculiar velocities. The transmitted flux $e^{-\tau_v}$ in each spectral bin v is therefore calculated by integrating along the line of sight x, all the contributions to the optical depth τ_v in that bin:

$$\tau_v = \int d\tau_v(x) = \int \sigma_0 \, \Phi_v(v_x, T_x, M_i) \, n_{ij}(x) \, dx. \tag{5.1}$$

In fact, this integral along the line of sight is calculated as a sum of the contributions from each simulation cell intersected by the line of sight. In cgs units,

$$\sigma_0 = \left(\frac{\pi e^2}{m_e c} \right) f_{lu}. \tag{5.2}$$

M_i and f_{lu} are the atomic mass of the element i and the upward oscillator strength of the transition being calculated. $\Phi_\nu(v_x, T_x, M_i)$ is the value at a frequency ν of the Voigt profile for a line caused by absorption in cell x, and $n_{ij}(x)$ is the number density of species ij in cell x. T_x is the temperature and v_x is the (Hubble plus peculiar) velocity of the gas in cell x.

$$\Phi_\nu = \frac{1}{\sqrt{\pi}\Delta\nu_D} H(a, u) \,, \tag{5.3}$$

where H is the Voigt function, $a \equiv c\gamma/(4\pi\nu_0 b)$ and $u \equiv (v - v_x)/b$, with the Doppler parameter $b = \sqrt{(}2k_B T_x/M_i)$.

I modified this programme, extending it to produce transmission functions for strong metal lines as well. For any such line, this new version of the programme reads in the

line-centre frequency ν_0, oscillator strength f_{lu} and damping constant γ from Table 2 of Vogel and Reimers (1995). To produce spectra from the `Timedep` results, it is also necessary to adopt some distribution of metals. For simplicity, homogenous metal abundances relative to hydrogen are adopted, so that the metal density simply traces the gas density around the quasar. As noted in the previous chapter, this is a good model if the metals polluting the IGM have been well mixed in the quasar's environment, for example by a galactic wind preceding the quasar phase. The metallicities used are 1% of the default solar abundances from `Cloudy` (versions 84–94) taken from meteoric abundances by Grevesse and Anders (1989) and Grevesse and Noels (1993). These abundances by number, relative to hydrogen, are multiplied by the hydrogen number densities $n_H(t)$ to give the number densities $n_i(t)$ of each metal. The number density of a given metal ion at some time t, is therefore found by multiplying this $n_i(t)$ by the time-dependent ion fraction f_{ij} calculated with `Timedep`.

Each spectral transition (e.g. each of the two lines in the CIV doublet) gives a different transmission function. These can be studied individually (see below) or could be multiplied together to give the total transmission function from a number of ion species. The absorption features are calculated as transmission functions in their local reference frames. These could then be redshifted by z_{abs}, and then multiplied on to a mock QSO continuum/emission spectrum at z_{em} to produce a mock observable spectrum. To compare directly with observed spectra, the mock spectrum could then be convolved with a typical instrument broadening function and have noise added to reproduce a possible measurement of the spectrum. However, this chapter will focus on the more general results from the normalised transmission functions plotted against velocity.

5.3 Analysis of an example LOS

Figure 5.1 shows an example of four transmission functions (or simply 'spectra') for both lines of the CIV doublet, the 1335Å CII line and the 1216Å Lyα line. The spectra are calculated from the simulation results at $z \sim 3.4$, along a line of sight passing 2.44Mpc away from the quasar. The graphs plot $e^{-\tau}$ for a range of velocities relative to a background source outside the simulation volume. A small section of the 1548Å CIV spectrum is shown in Figure 5.2 along with the spectrum calculated from the same simulated LOS but using the results produced by `Timedep` assuming ionisation equilibrium. The LOS passes through regions of the simulation that are receiving high

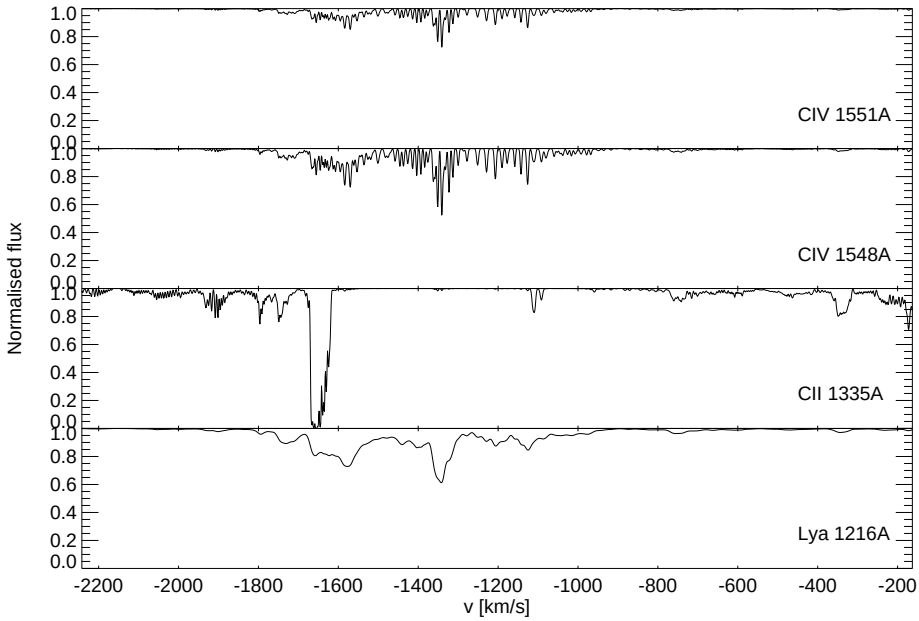

Figure 5.1: Transmission functions ($e^{-\tau_\nu}$) of four spectral lines along a line-of-sight through the simulation volume.

levels of UV flux from the young quasar at $z \sim 3.4$, but that have not yet had time to return to ionisation equilibrium. The metals in these regions (e.g. the yellow areas of Figure 5.4c) are therefore less ionised than an equilibrium calculation suggests, and therefore show less CIV absorption than is calculated assuming ionisation equilibrium. The most interesting implication is that observed absorption spectra may be getting misinterpreted by assuming they were caused by absorption by gas in ionisation equilibrium. This example LOS was selected to illustrate the differences in metal-line spectra that are possible between models which assume ionisation equilibrium and models which do not. The LOS was placed through regions that were both dense and far from equilibrium (at a given timestep). A scatterplot of all cells' absolute difference in their CIV fraction ($f_{CIV,eqm} - f_{CIV}$) against their density is given in Figure 5.3, for $z \sim 3.4$. Most cells that have f_{CIV} far from equilibrium have low density, while the most dense cells are close to equilibrium. Cells were selected by the cuts shown: with $n_H > 1.5 \times 10^{-5}\mathrm{cm}^{-3}$ and $(f_{CIV,eqm} - f_{CIV}) > 0.1$. All of these cells are shown in Figure 5.4a along with the cells through which the selected LOS passes to produce the spectra above. Also shown are maps of the hydrogen number density (in Figure 5.4b) and the absolute difference of the time-dependent CIV fraction from the equilibrium

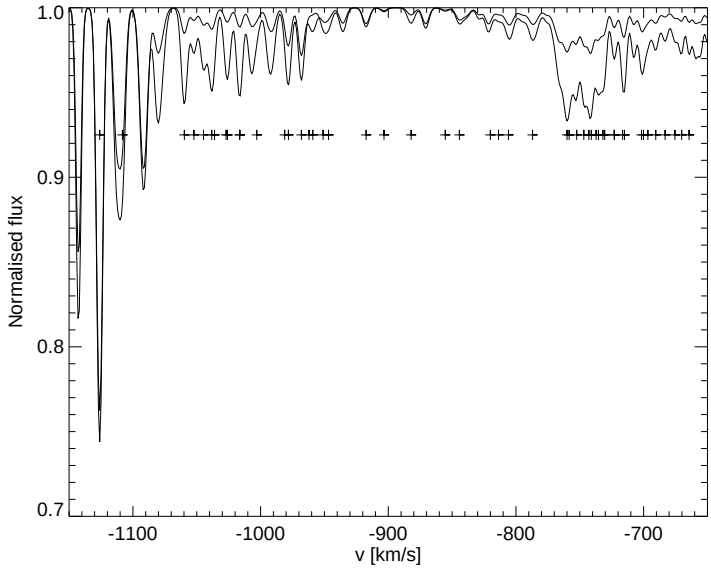

Figure 5.2: A section of the CIV 1548Å transmission function (in black, calculated by the time-dependent ionisation model) along with the transmission function from the equilibrium ionisation model (in grey). Note the range of the y-axis is shorter to show more detail. The plus symbols indicate the gas velocities (including Hubble flow and peculiar velocities) of the dense, non-equilibrium cells selected in Figs. 5.3 & 5.4a and intersected by the LOS.

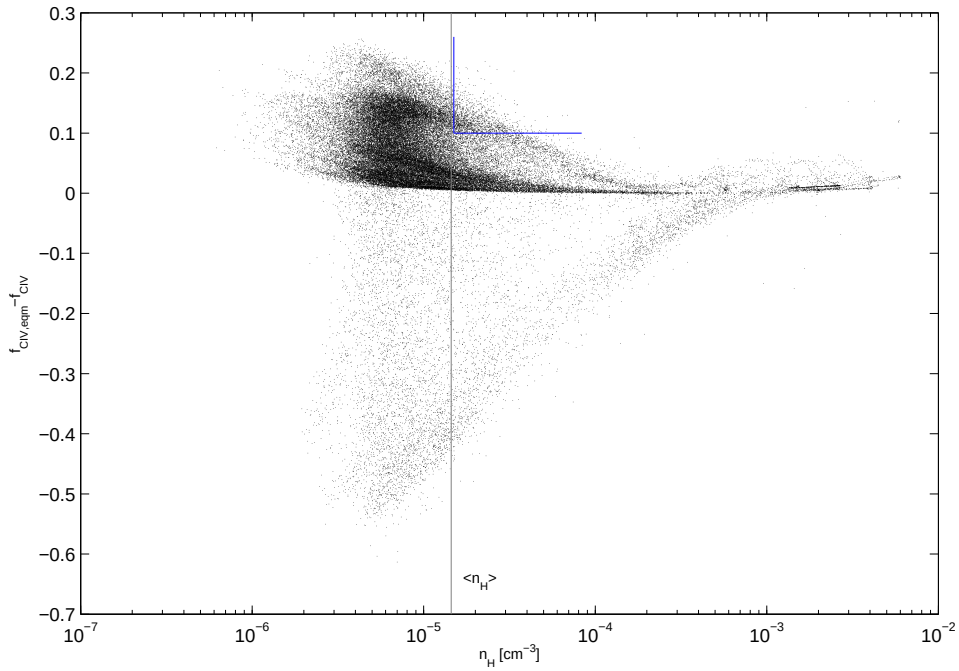

Figure 5.3: Scatterplot of all the cells in the simulation, showing their CIV absolute difference from equilibrium ($f_{CIV,eqm} - f_{CIV}$) and their hydrogen number density (n_H in cm^{-3}). The grey line shows the mean hydrogen number density at redshift $z = 3.4$, $\langle n_H \rangle = 1.45 \times 10^{-5}$cm^{-3}. The blue cuts select cells from the simulation with $n_H > 1.5 \times 10^{-5}$cm^{-3} and $(f_{CIV,eqm} - f_{CIV}) > 0.1$.

CIV fraction (in Figure 5.4c). As described in Section 4.3 (see Figure 4.11), the yellow regions of the absolute-difference plot show where the quasar's ionising radiation is sufficient at large radii that the carbon should have a high level of CIV (as in the equilibrium fraction) but the gas has not had time to reach equilibrium so the `Timedep` CIV fraction is still lower. At smaller radii the carbon has reached CIV but would be even more ionised in equilibrium, so $f_{CIV,eqm} < f_{CIV}$, producing the black regions. At the centre, both fractions are ionised to higher states, leaving zero CIV and thus zero absolute-difference.

Figures 4.10 and 4.11 in Chapter 4 showed the CIV ion-fraction absolute difference from equilibrium at more timesteps. The length of time that the yellow region exists in the simulation, showing $f_{CIV} < f_{eqm,CIV} - 0.1$, gives a measure of how long the CIV fraction is out of equilibrium. Examining similar maps made for other timesteps shows that these regions exist after the quasar turns on, from approximately $z \sim 3.44$ to 3.13, or for at least 200Myr. This is the same order of magnitude as the expected life-time for a quasar (10^8 years) so it is reasonable to assume that any CIV observed

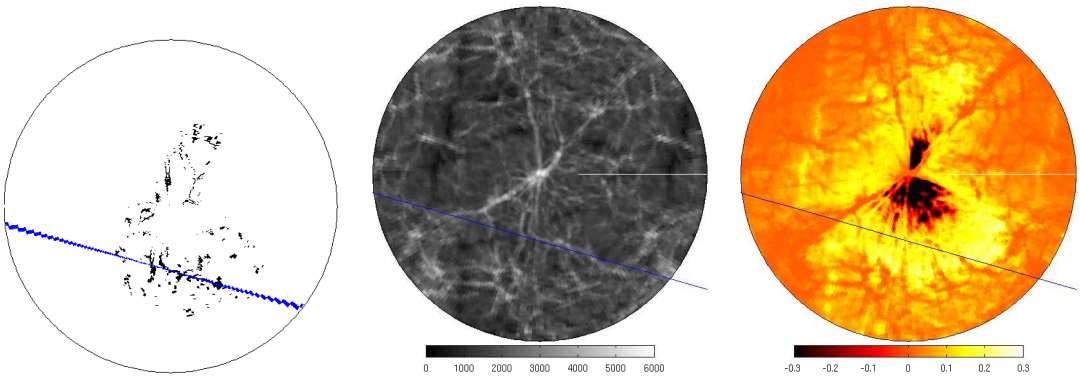

(a) Dense non-equilibrium cells (black) and LOS cells (blue).

(b) Hydrogen number-density n_H in m^{-3}.

(c) $f_{CIV,eqm} - f_{CIV}$.

Figure 5.4: Three maps of the simulation volume at $z \sim 3.4$ showing the LOS (in blue) producing the spectra in Fig. 5.1. Map 5.4a shows the cells (in black) selected by the cuts in Fig. 5.3 as being dense and having CIV out of equilibrium. Map 5.4b shows the hydrogen number-density n_H [cm^{-3}] (and recall, $n_C = 3.55 \times 10^{-6}\, n_H$). Map 5.4c shows the absolute difference of the CIV ion fraction from equilibrium, $f_{CIV,eqm} - f_{CIV}$.

as close to a quasar as the gas in this simulation, is likely to not be in ionisation equilibrium.

As an example of the implications of the use of the time-dependent metal ionisation data, the N_{CII}/N_{CIV} column density line-ratio has been calculated for some of the lines in the above spectra. The transmission functions plotted are $e^{-\tau_\nu}$. The equivalent width of a line in wavelength units is:

$$W = \int (1 - e^{-\tau_\nu})\, d\lambda = \frac{\lambda^2}{c} \int (1 - e^{-\tau_\nu})\, d\nu, \tag{5.4}$$

integrating only between the limits of the line. The column density of the line is:

$$N = \frac{\tau}{\sigma_0}, \tag{5.5}$$

where the optical depth is integrated across the line. For lines on the linear part of the Curve of Growth (with $\tau_\nu \ll 1$, see Section 1.2.3), $\tau_\nu \approx (1 - e^{-\tau_\nu})$. Therefore on the linear part of the Curve of Growth, the column density of a line can simply be taken as:

$$N = \frac{c\,W}{\lambda^2 \sigma_0} = \frac{1}{\sigma_0} \int (1 - e^{-\tau_\nu})\, d\nu. \tag{5.6}$$

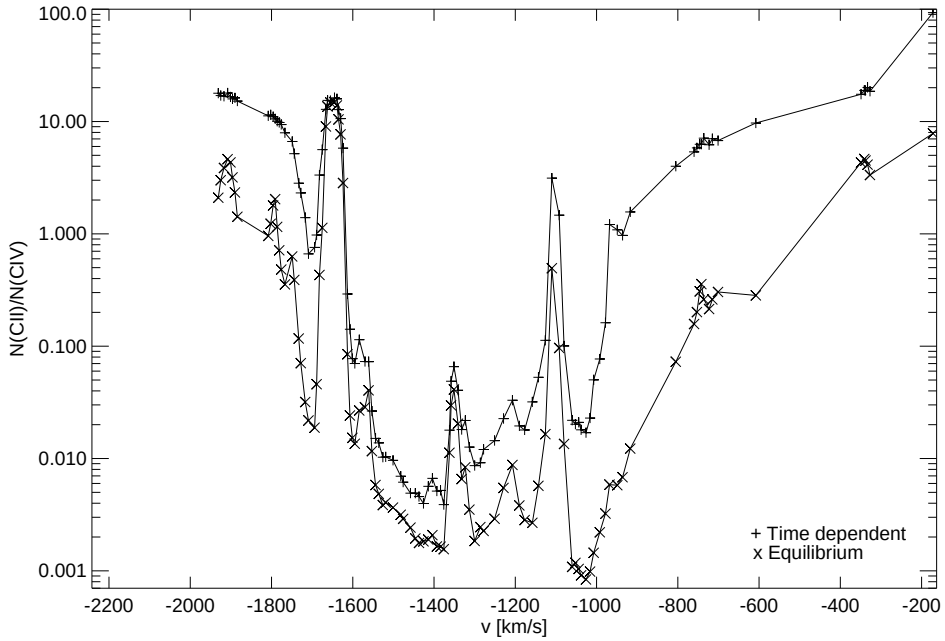

Figure 5.5: Column density line-ratios for all lines in Figure 5.1 with $e^{-\tau_\nu}$(CIV 1548Å)< 0.99, i.e. $\tau_\nu > 0.01$.

Note that this approximation for the column densities is not the only way that they could be calculated for the lines in the transmission functions. One alternative which would be used to analyse observed spectra, would be to use a line-fitting programme to identify the individual line profiles which make up the transmission function and calculate the column density of each line. The approximation in the equations above is much quicker to implement than line-fitting and produces column densities that are accurate enough to illustrate all of the points in the following analysis.

Figure 5.5 shows the N_{CII}/N_{CIV} column density line-ratio for all lines in the `Timedep` CIV spectrum, plotted against the velocities of the line centres. For this plot, all absorption lines have been identified by a very simple line-identifying routine. Any spectral bin that has a lower (CIV) flux $e^{-\tau_\nu}$ than both of its neighbours is selected as a line-centre. Successive bins out to both sides of each line-centre are selected as being in the line, so long as they have higher flux than the preceding bins (i.e. each selected line, is made up of all bins which show less absorption than the line-centre, out until the bins that show increased absorption from the next line).

Table 5.1: Column density and line-ratio results for the strongest CIV features. Note that both N_{CII} and N_{CIV} are calculated over the width of the CIV lines, whereas the N_{HI} values listed are measured over the wider Lyα lines at the corresponding velocities.

Line	N_{HI}	`Timedep`		Equilibrium		`Timedep`	Equilibrium
centre	(cm^{-2})	N_{CII} (cm^{-2})	N_{CIV} (cm^{-2})	N_{CII} (cm^{-2})	N_{CIV} (cm^{-2})	N_{CII}/N_{CIV}	N_{CII}/N_{CIV}
-1584	2.65×10^{13}	2.51×10^{12}	2.88×10^{11}	2.47×10^{12}	6.60×10^{10}	0.11	0.03
-1570	2.65×10^{13}	2.57×10^{12}	1.61×10^{11}	2.37×10^{12}	6.36×10^{10}	0.06	0.03
-1351	2.38×10^{13}	2.93×10^{12}	1.91×10^{11}	2.67×10^{12}	1.08×10^{11}	0.06	0.04
-1341	2.38×10^{13}	3.51×10^{12}	1.50×10^{11}	2.83×10^{12}	6.06×10^{10}	0.04	0.02
-1323	2.38×10^{13}	1.93×10^{12}	4.22×10^{10}	1.31×10^{12}	1.10×10^{10}	0.02	0.008
-1126	8.17×10^{12}	1.90×10^{12}	1.96×10^{11}	1.75×10^{12}	2.50×10^{10}	0.10	0.01

The two sets of points in Figure 5.5 show the line-ratios for the `Timedep` spectrum and the line-ratios of the results assuming ionisation equilibrium. The column densities were calculated using Equation 5.6 by integrating between the nearest maxima, so the lines do not all have the same widths because of blending. Line ratios have also been calculated for some strong lines using column densities integrated between other limits, from $\pm 5 \mathrm{km\,s^{-1}}$ to $\pm 50 \mathrm{km\,s^{-1}}$, and so long as both N_{CII} and N_{CIV} are calculated between the same limits, the line ratios fall on the same curves shown in Figure 5.5. Between approximately -1600km s^{-1} and -1000km s^{-1}, the line-ratio N_{CII}/N_{CIV} is less than 1.0, showing the excess of CIV relative to CII in the central region near the quasar. Further away from the quasar, the ionisation of the carbon atoms decreases and there is more CII than CIV. Along most of the spectrum, the CII to CIV line-ratio is lower in the equilibrium results, showing a higher level of CIV relative to CII. This higher level of ionisation in the equilibrium results is due to the carbon at this period in the `Timedep` simulation not having yet had time to ionise to the equilibrium level since the quasar turned on.

Of the CIV lines treated in Figure 5.5, the column densities and line ratios for the six strongest are given in Table 5.1, for both the time-dependent and the equilibrium spectra. Note that the quoted column densities for the corresponding Lyα lines are measured over the much wider Lyα features rather than just over the width of the CIV lines.

5.4 Observed difference from equilibrium

The next example use of the transmission functions drawn from the time-dependent ionisation results, is to look at the difference from equilibrium of all the CIV absorbers in a larger sample of lines of sight. The situation being considered is some future, high-resolution survey of CIV absorbers, and predicting what fractions of observed absorbers that might be close to a quasar may be out of ionisation equilibrium. If a significant fraction of the CIV absorbers might be out of equilibrium, then accurately interpreting such observations would require modelling with time-dependent ionisation of the metals. It is important to note that the results given in this section are just provided as an example use of this `Timedep` algorithm, and are not attempting to give accurate statistics which would require a wider range of simulations. For this application, eight tangential lines of sight are drawn through the simulation from Chapter 4 at each of three different impact parameters from the simulated quasar and at three

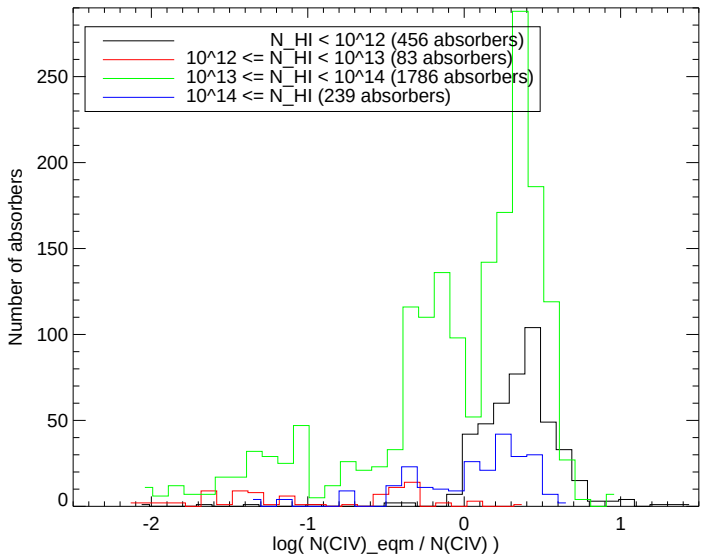

Figure 5.6: Histograms of the deviation from equilibrium of all CIV absorbers taken from 24 LOS in the simulation at $z = 3.4$, calculated by the column density ratio of each line in the equilibrium and time-dependent results' spectra, explained further in the text. The absorbers are split into different samples by the column density (cm^{-2}) of the corresponding Lyα line.

different times after the quasar turns on. This gives 24 LOS at each time, or 72 in total. The impact parameters are 1/4, 1/2 and 3/4 of the simulation radius. Each set of lines of sight are equally spaced around the quasar (i.e. are separated by 45°). LOS are produced at $z = 3.4$, 3.3 and 3.0. From each of these LOS, every CIV absorption line is identified using the simple routine from the previous section.

Figure 5.6 shows histograms of the deviation from equilibrium of CIV absorbers at $z = 3.4$, 63Myr after the quasar turns on. The plot shows the number of absorbers in bins of $log(N_{CIV,eqm}/N_{CIV})$, the logarithm of each absorber's column density ratio between spectra from the equilibrium and the time-dependent ionisation results. For example, the bar at 0 shows absorbers in equilibrium; the bar at 1 shows absorbers lacking CIV in the time-dependent results so that $N_{CIV,eqm} = 10N_{CIV}$; and the bar at -1 shows absorbers with an excess of CIV in the time-dependent results so that $N_{CIV,eqm} = 10^{-1}N_{CIV}$. The separate curves show different absorbers, split according to the column density N_{HI} of the corresponding Lyα line. The number of absorbers in each sample is given in the figure's legend. Note, however, that the absolute numbers of absorbers is not important, but rather each sample's relative distribution of line ratios.

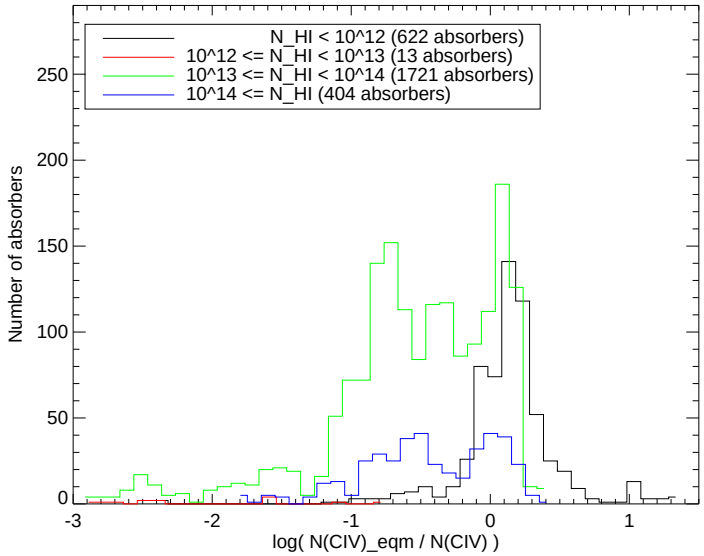

Figure 5.7: As Figure 5.6 but with lines of sight taken from simulation at $z = 3.3$.

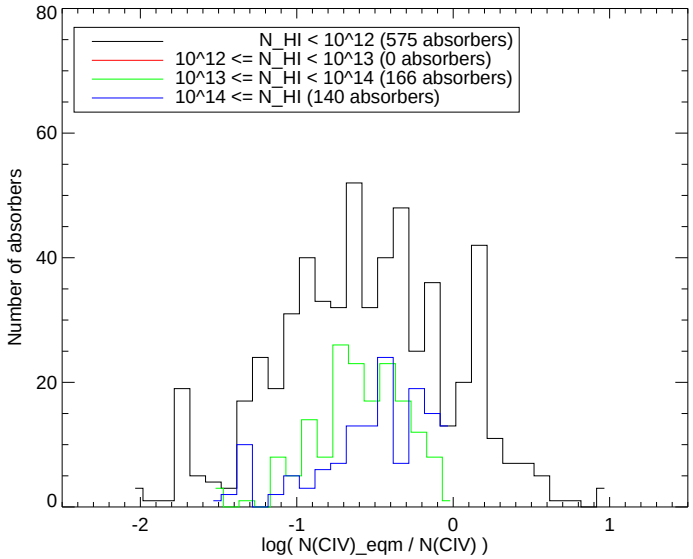

Figure 5.8: As Figure 5.6 but with lines of sight taken from simulation at $z = 3.0$.

Three of the curves have similar distributions peaked around $N_{CIV,eqm}/N_{CIV} \sim 10^{0.3}$, with long tails showing some CIV absorbers with $N_{CIV} \gg N_{CIV,eqm}$. The very low red curve shows absorbers with $10^{12} \leq N_{HI} < 10^{13}\text{cm}^{-2}$, which mostly have $N_{CIV,eqm}/N_{CIV} \sim 10^{-0.4}$. However, the number of absorbers in this sample is small so it is likely that its distribution is dominated by noise. The distribution of absorbers with $N_{HI} < 10^{12}\text{cm}^{-2}$ (black curve), drops off quickly below $N_{CIV,eqm}/N_{CIV} \sim 10^{0}$ showing these absorbers almost all have a lack of CIV relative to the equilibrium fractions. The two highest density samples (green and blue curves) have similar distributions. These absorbers have a wide range of line ratios, with the largest peak in the distribution showing that many have a lack of CIV relative to the equilibrium fraction, while both distributions also show a smaller second peak of absorbers with an excess of CIV, and a long tail of a few absorbers with very small $N_{CIV,eqm}/N_{CIV}$.

The histograms of line ratios for absorbers at $z = 3.3$ are given in Figure 5.7. The $N_{HI} < 10^{12}\text{cm}^{-2}$ absorbers (black curve) have a narrow distribution of line ratios centred close to equilibrium. The next cut in N_{HI} has very few absorbers (red curve) so is again does not show its true distribution because of noise. The two samples with the highest HI column densities (green and blue curves) again have similar distributions, here centred around $N_{CIV,eqm}/N_{CIV} \sim 10^{-0.4}$ but with some absorbers with $10^{13} \leq N_{HI} < 10^{14}\text{cm}^{-2}$ having $N_{CIV,eqm}/N_{CIV} \sim 10^{-2.9}$.

Figure 5.8 shows the degree to which the CIV absorbers are out of equilibrium by $z = 3.0$. Only three of the N_{HI} ranges have any absorbers, and these all have distributions similarly peaked around $N_{CIV,eqm}/N_{CIV} \sim 10^{-0.5}$. The $N_{HI} < 10^{12}\text{cm}^{-2}$ absorbers (black curve) include some that are further from equilibrium making this distribution slightly wider. The absorbers with $10^{13} \leq N_{HI}$ (green and blue curves) all show an excess of CIV compared to equilibrium, as there are none with $N_{CIV,eqm}/N_{CIV} > 10^{0.0}$.

This last figure shows that the CIV in the simulation is still out of equilibrium at $z = 3.0$. At later times in the simulation, it is expected that the time-dependent CIV fraction will reach equilibrium (see Figures 4.8 and 4.10). However, since this simulation includes a high luminosity quasar, there is actually very little CIV within the simulation volume at later times.

The histograms produced in this section have shown that CIV absorbers close to a quasar can have a significantly different column density compared to equilibrium. If some future CIV survey targets absorbers close to a possible quasar, it would certainly not detect all of the absorbers included here, as many would be too weak. These figures show however, that the absorbers that are detected are likely to include some that are

out of ionisation equilibrium, so assuming equilibrium in their analysis would lead to them being misinterpreted.

5.5 Summary

The work in this chapter has focused on creating mock quasar absorption from simulations:

- A new routine was made, for creating transmission functions for heavy-element absorption lines, from lines of sight placed through the `PMRT/Timedep` simulation volume described in Chapter 4. CII and CIV spectra made using the time-dependent metal ionisation results were presented, along with earlier Lyα spectra. The resulting metal lines are much narrower than the corresponding Lyα lines, revealing substructure that would perhaps be blended in practical observations.

- With metal abundances of 1% solar, strong metal features in these example spectra had column densities of $N_{CII} \sim 10^{11}\mathrm{cm}^{-2}$, $N_{CIV} \sim 10^{12}\mathrm{cm}^{-2}$ and $N_{HI} \sim 10^{13}\mathrm{cm}^{-2}$. Lower abundances would produce weaker lines, and to practically observe such lines would require extremely high signal-to-noise measurements, better than achievable today. However, the next generation of ground based telescopes currently being developed (so called Extremely Large Telescopes) may be able to push towards such capabilities so it is reasonable to consider such observations.

- Spectra have also been produced from the data calculated by `Timedep` using the assumption of ionisation equilibrium. These demonstrate how different the results of any IGM simulation could be if the time-dependent ionisation equations are solved, and show that the difference between spectra from gas that is in ionisation equilibrium and gas that has not had time to reach equilibrium might be large enough to observe. These spectra also suggest that observed metal features in quasar absorption spectra may be misinterpreted if the absorbing systems are modelled by assuming ionisation equilibrium.

- The relevant timescales for these non-equilibrium effects are discussed, and it was found that for example, the CIV nearby to a young quasar may not reach its equilibrium ionisation fraction for 200Myr, on the same order as the expected lifetimes of quasars themselves. This highlights that time-dependent metal ionisation

should be considered in future modelling of IGM metals, especially close to bright sources.

- The column density line-ratio N_{CII}/N_{CIV} has been calculated for the absorption systems along a LOS through the time-dependent simulation results, and the same LOS through the equilibrium simulation results. Line-ratios from the IGM around a young QSO in either set of data are found over some four orders of magnitude.

- At a given time following the turn-on of a young QSO, N_{CII}/N_{CIV} can be significantly different depending on whether or not ionisation equilibrium is assumed. For example, this line ratio for the strongest CIV lines at $z \sim 3.4$ is between 2–10 times higher for the time-dependent results than the equilibrium results, because of the delay in metal ionisation reacting to the young quasar's luminosity.

- A large sample of CIV absorbers have been identified in lines of sight drawn through the simulation volume. The column density ratio $N_{CIV,eqm}/N_{CIV}$ is used as a measure of how far out of equilibrium each absorber is. The distributions of this line ratio have been measured for sub-samples of these absorbers, showing how far out of equilibrium observed CIV systems might be.

The application of the `Timedep` code to this simulation of the IGM around a young quasar has demonstrated how the new algorithm can be used to offer new insight into the ionisation of metals. There are still more results to be extracted from the data produced, but it is hoped that this application has also shown how useful time-dependent ionisation calculations will be for other work modelling metals in the intergalactic medium for future simulations and observations.

Bibliography

Abel, T., Norman, M. L., and Madau, P.: 1999, ApJ **523**, 66

Adelberger, K. L., Shapley, A. E., Steidel, C. C., Pettini, M., Erb, D. K., and Reddy, N. A.: 2005, ApJ **629**, 636

Agafonova, I. I., Levshakov, S. A., Reimers, D., Fechner, C., Tytler, D., Simcoe, R. A., and Songaila, A.: 2007, A&A **461**, 893

Aguirre, A., Schaye, J., Kim, T.-S., Theuns, T., Rauch, M., and Sargent, W. L. W.: 2004, ApJ **602**, 38

Aguirre, A., Schaye, J., and Theuns, T.: 2002, ApJ **576**, 1

Aldrovandi, S. M. V. and Pequignot, D.: 1973, A&A **25**, 137

Ali, B., Blum, R. D., Bumgardner, T. E., Cranmer, S. R., Ferland, G. J., Haefner, R. I., and Tiede, G. P.: 1991, PASP **103**, 1182

Arnaud, M. and Raymond, J.: 1992, ApJ **398**, 394

Arnaud, M. and Rothenflug, R.: 1985, A&AS **60**, 425

Bahcall, J. N., Greenstein, J. L., and Sargent, W. L. W.: 1968, ApJ **153**, 689

Bajtlik, S., Duncan, R. C., and Ostriker, J. P.: 1988, ApJ **327**, 570

Becker, G. D., Rauch, M., and Sargent, W. L. W.: 2009, ApJ **698**, 1010

Bergeron, J., Petitjean, P., Sargent, W. L. W., Bahcall, J. N., Boksenberg, A., Hartig, G. F., Jannuzi, B. T., Kirhakos, S., Savage, B. D., Schneider, D. P., Turnshek, D. A., Weymann, R. J., and Wolfe, A. M.: 1994, ApJ **436**, 33

Bergeron, J. and Stasińska, G.: 1986, A&A **169**, 1

Bolton, J., Meiksin, A., and White, M.: 2004, MNRAS **348**, L43

Bottcher, C., Mccray, R. A., Jura, M., and Dalgarno, A.: 1970, Astrophys. Lett. **6**, 237

Burgess, A.: 1965, ApJ **141**, 1588

Cen, R. and Fang, T.: 2006, ApJ **650**, 573

Churchill, C. W.: 2011, *Cosmological Absorption Line Spectroscopy*, Cambridge University Press, Cambridge, in prep.

Cohen, S. D. and Hindmarsh, A. C.: 1996, *Computers in Physics* **10(2)**, 138

Cowie, L. L. and Songaila, A.: 1998, Nature **394**, 44

Cowie, L. L., Songaila, A., Kim, T.-S., and Hu, E. M.: 1995, AJ **109**, 1522

Crain, R. A., Theuns, T., Dalla Vecchia, C., Eke, V. R., Frenk, C. S., Jenkins, A., Kay, S. T., Peacock, J. A., Pearce, F. R., Schaye, J., Springel, V., Thomas, P. A., White, S. D. M., and Wiersma, R. P. C.: 2009, *ArXiv e-prints, 0906.4350*

Croft, R. A. C.: 2004, ApJ **610**, 642

Crotts, A. P. S. and Fang, Y.: 1998, ApJ **502**, 16

Davidson, K.: 1975, ApJ **195**, 285

Donahue, M. and Shull, J. M.: 1991, ApJ **383**, 511

Edgar, R. J. and Chevalier, R. A.: 1986, ApJ **310**, L27

Ellison, S. L., Ibata, R., Pettini, M., Lewis, G. F., Aracil, B., Petitjean, P., and Srianand, R.: 2004, A&A **414**, 79

Ellison, S. L., Songaila, A., Schaye, J., and Pettini, M.: 2000, AJ **120**, 1175

Ferland, G. J.: 1996, *Hazy, A Brief Introduction to Cloudy 90*, University of Kentucky Internal Report

Ferland, G. J.: 2004, *Hazy, A Brief Introduction to Cloudy 96*, University of Kentucky Internal Report

Ferland, G. J.: 2008, *Hazy, A Brief Introduction to Cloudy, Version 08*, University of Kentucky Internal Report

Ferland, G. J., Korista, K. T., Verner, D. A., and Dalgarno, A.: 1997, ApJ **481**, L115+

Ferland, G. J., Korista, K. T., Verner, D. A., Ferguson, J. W., Kingdon, J. B., and Verner, E. M.: 1998, PASP **110**, 761

Fernandez-Soto, A., Barcons, X., Carballo, R., and Webb, J. K.: 1995, MNRAS **277**, 235

Gnat, O. and Sternberg, A.: 2007, ApJS **168**, 213

Gnat, O. and Sternberg, A.: 2009, ApJ **693**, 1514

Gnedin, N. Y. and Abel, T.: 2001, *New Astronomy* **6**, 437

Gonçalves, T. S., Steidel, C. C., and Pettini, M.: 2008, ApJ **676**, 816

Grevesse, N. and Anders, E.: 1989, in C. J. Waddington (ed.), *Cosmic Abundances of Matter*, Vol. 183 of *American Institute of Physics Conference Series*, pp 1–8

Grevesse, N. and Noels, A.: 1993, in N. Prantzos, E. Vangioni-Flam, and M. Casse (eds.), *Origin and Evolution of the Elements*, pp 15–25

Gunn, J. E. and Peterson, B. A.: 1965, ApJ **142**, 1633

Haardt, F. and Madau, P.: 1996, ApJ **461**, 20

Haardt, F. and Madau, P.: 2001, in D. M. Neumann & J. T. V. Tran (ed.), *Clusters of Galaxies and the High Redshift Universe Observed in X-rays*

Heckman, T. M., Norman, C. A., Strickland, D. K., and Sembach, K. R.: 2002, ApJ **577**, 691

Henney, W. J., Arthur, S. J., and García-Díaz, M. T.: 2005, ApJ **627**, 813

Henney, W. J., Williams, R. J. R., Ferland, G. J., Shaw, G., and O'Dell, C. R.: 2007, ApJ **671**, L137

Hindmarsh, A. C. and Serban, R.: 2009, *User Documentation for CVODE v2.6.0*, Technical Report UCRL-SM-208108, Lawrence Livermore National Laboratory

Hockney, R. W. and Eastwood, J. W.: 1988, *Computer Simulation Using Particles*, Taylor & Francis, Inc., Bristol, PA, USA

Iliev, I. T., Mellema, G., Pen, U.-L., Merz, H., Shapiro, P. R., and Alvarez, M. A.: 2006, MNRAS **369**, 1625

Jura, M. and Dalgarno, A.: 1972, ApJ **174**, 365

Kaastra, J. S. and Mewe, R.: 1993, A&AS **97**, 443

Kafatos, M.: 1973, ApJ **182**, 433

Kafatos, M. C. and Tucker, W. H.: 1972, ApJ **175**, 837

Kingdon, J. B. and Ferland, G. J.: 1996, ApJS **106**, 205

Komatsu, E., Dunkley, J., Nolta, M. R., Bennett, C. L., Gold, B., Hinshaw, G., Jarosik, N., Larson, D., Limon, M., Page, L., Spergel, D. N., Halpern, M., Hill, R. S., Kogut, A., Meyer, S. S., Tucker, G. S., Weiland, J. L., Wollack, E., and Wright, E. L.: 2009, ApJS **180**, 330

Kulkarni, V. P., Khare, P., Péroux, C., York, D. G., Lauroesch, J. T., and Meiring, J. D.: 2007, ApJ **661**, 88

Landau, L. D. and Lifshitz, E. M.: 1959, *Fluid mechanics*, Course of theoretical physics, Oxford: Pergamon Press, 1959

Landini, M. and Monsignori Fossi, B. C.: 1990, A&AS **82**, 229

Landini, M. and Monsignori Fossi, B. C.: 1991, A&AS **91**, 183

Lu, L.: 1991, ApJ **379**, 99

Lu, L., Wolfe, A. M., and Turnshek, D. A.: 1991, ApJ **367**, 19

Lynds, R.: 1971, ApJ **164**, L73+

Madau, P.: 1991, ApJ **376**, L33

Meiksin, A., Tittley, E. R., and Brown, C. K.: 2010, MNRAS **401**, 77

Meiksin, A. and White, M.: 2001, MNRAS **324**, 141

Meiksin, A., White, M., and Peacock, J. A.: 1999, MNRAS **304**, 851

Meiksin, A. A.: 2009, *Reviews of Modern Physics* **81**, 1405

Mellema, G., Iliev, I. T., Alvarez, M. A., and Shapiro, P. R.: 2006, *New Astronomy* **11**, 374

Meyer, D. M. and York, D. G.: 1987, ApJ **315**, L5

Murdoch, H. S., Hunstead, R. W., Pettini, M., and Blades, J. C.: 1986, ApJ **309**, 19

Murray, N., Quataert, E., and Thompson, T. A.: 2005, ApJ **618**, 569

Nagamine, K., Cen, R., Hernquist, L., Ostriker, J. P., and Springel, V.: 2005, ApJ **618**, 23

Nagamine, K., Springel, V., and Hernquist, L.: 2004a, MNRAS **348**, 421

Nagamine, K., Springel, V., and Hernquist, L.: 2004b, MNRAS **348**, 435

Nussbaumer, H. and Storey, P. J.: 1983, A&A **126**, 75

Nussbaumer, H. and Storey, P. J.: 1986, A&AS **64**, 545

Nussbaumer, H. and Storey, P. J.: 1987, A&AS **69**, 123

Oppenheimer, B. D. and Davé, R.: 2006, MNRAS **373**, 1265

Oppenheimer, B. D. and Davé, R.: 2008, MNRAS **387**, 577

Osterbrock, D. E.: 1989, *Astrophysics of gaseous nebulae and active galactic nuclei*, University Science Books, Mill Valley, CA

Paschos, P., Norman, M. L., Bordner, J. O., and Harkness, R.: 2007, *ArXiv e-prints, 0711.1904*

Perna, R. and Lazzati, D.: 2002, ApJ **580**, 261

Péroux, C., Dessauges-Zavadsky, M., Kim, T., McMahon, R. G., and D'Odorico, S.: 2002, Ap&SS **281**, 543

Petitjean, P. and Bergeron, J.: 1994, A&A **283**, 759

Pettini, M.: 2004, in C. Esteban, R. García López, A. Herrero, and F. Sánchez (eds.), *Cosmochemistry. The melting pot of the elements*, pp 257–298

Pettini, M.: 2006, *Physical Cosmology*, Undergraduate lecture course notes. `http://www.ast.cam.ac.uk/~pettini/PhysicalCosmology/` Available online June 2006

Pieri, M. M., Schaye, J., and Aguirre, A.: 2006, ApJ **638**, 45

Press, W. H., Teukolsky, S. A., Vetterling, W. T., and Flannery, B. P.: 1992, *Numerical recipes in C. The art of scientific computing*, Cambridge University Press

Rauch, M.: 1998, ARA&A **36**, 267

Rauch, M., Haehnelt, M. G., and Steinmetz, M.: 1997, ApJ **481**, 601

Rauch, M., Sargent, W. L. W., and Barlow, T. A.: 2001, ApJ **554**, 823

Reed, D. S., Bower, R., Frenk, C. S., Gao, L., Jenkins, A., Theuns, T., and White, S. D. M.: 2005, MNRAS **363**, 393

Ryan-Weber, E. V., Pettini, M., and Madau, P.: 2006, MNRAS **371**, L78

Rybicki, G. B. and Lightman, A. P.: 1979, *Radiative processes in astrophysics*, Wiley-Interscience, New York

Sargent, W. L. W., Young, P. J., Boksenberg, A., and Tytler, D.: 1980, ApJS **42**, 41

Savin, D. W.: 2001, in G. Ferland and D. W. Savin (eds.), *Spectroscopic Challenges of Photoionized Plasmas*, Vol. 247 of *Astronomical Society of the Pacific Conference Series*, pp 167–+

Schaye, J., Aguirre, A., Kim, T.-S., Theuns, T., Rauch, M., and Sargent, W. L. W.: 2003, ApJ **596**, 768

Schaye, J., Carswell, R. F., and Kim, T.-S.: 2007, MNRAS **379**, 1169

Schirber, M., Miralda-Escudé, J., and McDonald, P.: 2004, ApJ **610**, 105

Schmutzler, T. and Tscharnuter, W. M.: 1993, A&A **273**, 318

Seager, S.: 2001, in G. Ferland and D. W. Savin (eds.), *Spectroscopic Challenges of Photoionized Plasmas*, Vol. 247 of *Astronomical Society of the Pacific Conference Series*, pp 327–+

Semat, H. and Albright, J. R.: 1973, *Introduction to Atomic and Nuclear Physics*, Chapman and Hall, London, fifth edition

Shapiro, P. R. and Moore, R. T.: 1976, ApJ **207**, 460

Shull, J. M. and van Steenberg, M.: 1982, ApJS **48**, 95

Simcoe, R. A.: 2006, ApJ **653**, 977

Simcoe, R. A., Sargent, W. L. W., and Rauch, M.: 2004, ApJ **606**, 92

Simcoe, R. A., Sargent, W. L. W., Rauch, M., and Becker, G.: 2006, ApJ **637**, 648

Smith, C. J. and Stokes, A. R.: 1972, *The Principles of Atomic and Nuclear Physics*, Edward Arnold, London, first edition

Smith, R. K., Krzewina, L. G., Cox, D. P., Edgar, R. J., and Miller, III, W. W.: 1996, ApJ **473**, 864

Songaila, A.: 1997, ApJ **490**, L1+

Songaila, A.: 2001, ApJ **561**, L153

Songaila, A. and Cowie, L. L.: 1996, AJ **112**, 335

Spergel, D. N., Verde, L., Peiris, H. V., Komatsu, E., Nolta, M. R., Bennett, C. L., Halpern, M., Hinshaw, G., Jarosik, N., Kogut, A., Limon, M., Meyer, S. S., Page, L., Tucker, G. S., Weiland, J. L., Wollack, E., and Wright, E. L.: 2003, ApJS **148**, 175

Spinrad, H., Filippenko, A. V., Yee, H. K., Ellingson, E., Blades, J. C., Bahcall, J. N., Jannuzi, B. T., Bechtold, J., and Dobrzycki, A.: 1993, AJ **106**, 1

Spitzer, L.: 1978, *Physical processes in the interstellar medium*, Wiley-Interscience, New York

Springel, V.: 2005, MNRAS **364**, 1105

Springel, V. and Hernquist, L.: 2003a, MNRAS **339**, 289

Springel, V. and Hernquist, L.: 2003b, MNRAS **339**, 312

Springel, V., White, S. D. M., Jenkins, A., Frenk, C. S., Yoshida, N., Gao, L., Navarro, J., Thacker, R., Croton, D., Helly, J., Peacock, J. A., Cole, S., Thomas, P., Couchman, H., Evrard, A., Colberg, J., and Pearce, F.: 2005, Nature **435**, 629

Stasińska, G.: 1984, A&AS **55**, 15

Steidel, C. C., Shapley, A. E., Pettini, M., Adelberger, K. L., Erb, D. K., Reddy, N. A., and Hunt, M. P.: 2004, ApJ **604**, 534

Stocke, J. T., Shull, J. M., and Penton, S. V.: 2004, *ArXiv e-prints, astro-ph/0407352*

Sutherland, R. S. and Dopita, M. A.: 1993, ApJS **88**, 253

Tescari, E., Viel, M., D'Odorico, V., Cristiani, S., Calura, F., Borgani, S., and Tornatore, L.: 2010, *ArXiv e-prints, 1007.1628*

Theuns, T.: 2005, in P. Williams, C.-G. Shu, and B. Menard (eds.), *IAU Colloq. 199: Probing Galaxies through Quasar Absorption Lines*, pp 185–204

Tittley, E. R. and Meiksin, A.: 2007, MNRAS **380**, 1369

Tytler, D.: 1987, ApJ **321**, 69

Tytler, D., Fan, X.-M., Burles, S., Cottrell, L., Davis, C., Kirkman, D., and Zuo, L.: 1995, in G. Meylan (ed.), *QSO Absorption Lines, Proceedings of the ESO Workshop Held at Garching, Germany, 21 - 24 November 1994, edited by Georges Meylan. Springer-Verlag Berlin Heidelberg New York. Also ESO Astrophysics Symposia, 1995., p.289*, pp 289–+

Verner, D. A.: 2000, *Atomic Data for Astrophysics*, `http://www.pa.uky.edu/~verner/atom.html`, accessed Sept. 2009.

Verner, D. A. and Ferland, G. J.: 1996, ApJS **103**, 467

Verner, D. A., Ferland, G. J., Korista, K. T., and Yakovlev, D. G.: 1996, ApJ **465**, 487

Verner, D. A. and Yakovlev, D. G.: 1990, Ap&SS **165**, 27

Verner, D. A. and Yakovlev, D. G.: 1995, A&AS **109**, 125

Vogel, S. and Reimers, D.: 1995, A&A **294**, 377

Vogt, S. S., Allen, S. L., Bigelow, B. C., Bresee, L., Brown, B., Cantrall, T., Conrad, A., Couture, M., Delaney, C., Epps, H. W., Hilyard, D., Hilyard, D. F., Horn, E., Jern, N., Kanto, D., Keane, M. J., Kibrick, R. I., Lewis, J. W., Osborne, J., Pardeilhan, G. H., Pfister, T., Ricketts, T., Robinson, L. B., Stover, R. J., Tucker, D., Ward, J., and Wei, M. Z.: 1994, in D. L. Crawford and E. R. Craine (eds.), *Proc. SPIE Instrumentation in Astronomy VIII, David L. Crawford; Eric R. Craine; Eds., Volume 2198, p. 362*, pp 362–+

Voronov, G. S.: 1997, *Atomic Data and Nuclear Data Tables* **65**, 1

Wolfe, A. M., Gawiser, E., and Prochaska, J. X.: 2005, ARA&A **43**, 861

Wolfe, A. M., Turnshek, D. A., Smith, H. E., and Cohen, R. D.: 1986, ApJS **61**, 249

York, D. G., Green, R. F., Bechtold, J., and Chaffee, Jr., F. H.: 1984, ApJ **280**, L1

Yoshida, N., Omukai, K., Hernquist, L., and Abel, T.: 2006, ApJ **652**, 6

Yoshikawa, K. and Sasaki, S.: 2006, PASJ **58**, 641